THERMODYNAMIC AND KINETIC EXAMINATIONS OF INORGANIC MATERIALS FORMATION

BY

ZHELONG JIANG

DISSERTATION

Submitted in partial fulfillment of the requirements
for the degree of Doctor of Philosophy in Materials Science and Engineering
in the Graduate College of the
University of Illinois at Urbana-Champaign, 2019

Urbana, Illinois

Doctoral Committee:

Assistant Professor Daniel P. Shoemaker, Chair
Professor Jian-Min Zuo
Professor Shen J. Dillon
Professor Andrew G. Gewirth

ABSTRACT

Inorganic materials formation is the result of a complicated interplay between thermodynamics and kinetics. Improved understanding of such factors can aid the synthesis of target materials and the discovery of new materials. Here, techniques for carrying out time-resolved studies were developed and demonstrated for the investigation of solvothermal and solid state reactions. Detailed kinetic reaction progress maps were constructed, showing quantitative information on the kinetic development of the quantity of each constituent phase during chemical reactions. The approach deployed has little restriction on the reaction conditions, and therefore can be used as a protocol for other kinetic studies of the demonstrated reaction types: solvothermal and solid state. It is shown that detailed and thorough reaction kinetics can be retrieved reliably by combining X-ray diffraction (XRD) with supplementary characterization methods without reliance on synchrotron-based facilities, allowing for high-throughout screening of different reactions. Synchrotron-based *in situ* XRD was also tested and developed, which can provide more insight for those selected systems that require higher-fidelity data collection. In this dissertation, it is shown that valuable mechanistic knowledge on materials syntheses can be learned from such types of thermodynamic and kinetic investigations, which can be effectively employed for the discovery of new material structures.

Comprehensive quantitative information was obtained on phase evolution during the solvothermal synthesis of Cu_4O_3 based on time-resolved *ex situ* investigations. Combined with the observation of phase correlations, it was realized that the transition through $Cu_2(NO_3)(OH)_3$ and a proper redox environment is critical to form Cu_4O_3. With the use of *in situ* energy-dispersive X-ray diffraction carried out at 6-BM-B in Advanced Photon Source, it was verified that all copper oxide forms CuO, Cu_2O, and Cu_4O_3 were made at the solvothermal temperature. It was also shown that at the local scale, no apparent transformation between Cu_4O_3 and CuO / Cu_2O took place, but the transformation between CuO and Cu_2O was evident, supporting the reaction mechanism proposed from the *ex situ* study. Through changes in the solvothermal chemistry, it was shown that direct transformation of $Cu_2(NO_3)(OH)_3$ to Cu_4O_3 could not be achieved with a simple mixture of ethanol and dimethylformamide. Some species generated in the original Cu_4O_3 synthesis scheme are required in order for such transformation to take place, which are yet to be confirmed in identity. After testing with several solvothermal solvents, it was discovered that solvent chemistry has a huge impact on the phase stability of Cu-containing inorganic materials, and four new crystalline phases were suggested based on unmatched diffraction patterns. Among these new structures, one is a coordination compound, which possesses a unique coordination stereochemistry. In this structure, Cu is coordinated to two chelating ethylenediamine ligands and one monodentate ethylenediamine ligand, which is unprecedented.

Solid state synthesis of Fe_2SiS_4 was investigated using *in situ* X-ray diffraction. Important factors that affect Fe_2SiS_4 formation kinetics are identified to be a peritectic transition, intermetallic formation, and particle size reduction. These factors were explored for the discovery of new ternary chalcogenide materials. Realizing the effectiveness of burst formation of superheated liquid on materials formation kinetics, we explored flux-crystallization of Ba–Fe–S materials utilizing BaS_3 as a reactive flux. Both lab and synchrotron *in situ* X-ray diffraction verified that novel crystalline phases formed when the system was in the flux state. Through the analysis of a particular set of synchrotron *in situ* X-ray diffraction patterns, we give suggestions on the diffraction profiles of five new flux-grown Ba–Fe–S phases. Materials discovery was also carried out with solid state synthesis for ternary sulfide and selenides systems with the help of ball milling reagents for kinetic enhancement. Based on the X-ray diffraction results of the products, the existence of three new materials are shown in the ternary systems of Sr–V–S, Sr–Cr–S, and Sr–Ni–S.

ACKNOWLEDGMENTS

First and foremost, I would like to thank my advisor, Daniel Shoemaker. Through talking to him, I have learned a lot about critical thinking in research. When presented with observation, he has often surprised me by coming up with possible explanations that did not occur to me, and these explanations were frequently correct. I have learned to think about problems more thoroughly and not to make hasty decisions based on superficial guesses. He has shown me the importance of making tools from your own designs in problem-solving, which seldom came to me before I joined his group. He has given me guidance on how to proceed when I feel stagnant in the process of my work. He is very fast in responding to emails, reviewing my writings, and reaching out to other personnel, which I have always appreciated. Throughout my graduate study, he has also referred me to activities that benefit my personal development, and I am grateful towards that.

I am greatly thankful to all the undergraduate and Master students who have cooperated with me in my projects: Jai Sharma, Insung Han, Allen Guo, Frank Kelly, and Arun Ramanathan. Without you, this dissertation would not be finished, and your work had contributed to a significant and critical portion to my thesis work. You are all amazing partners, and it was my pleasure to have worked together with you. All the undergraduates I tutored with (Jai Sharma, Allen Guo, and Frank Kelly) were diligent. I never had to worry about the tasks given to you. They were all done in a timely fashion, and sometimes I feel I was able to keep up my own pace of work thanks to you. I would like to especially thank Jai Sharma, who has been in the group the longest. He has come up with plenty of ideas to try in research, and because of it, we have achieved significant progress together. I am also very happy to have guided Arun Ramanathan and Insung Han into working in our group. Even though they had their own projects, their work had shaped my projects in critical fashions. Insung Han is also a close friend. He is one of the most hard-working people I ever know, and thanks to him, I had precious companionship during evening working hours.

I have to thank my groupmates Ankita Bhutani and Rebecca McAuliffe. The three of us joined the Shoemaker group together as the first batch of students. We have built the lab together, studies coursework together, learned research together, maintained the lab together, and discussed life and world together. Our efforts of setting up a research lab from the basics had me develop a comrade-like relationship with you that is very precious. We have had a lot of fun in running the lab, and I will never forget the laughter we shared in the office from the occasional chit-chat times.

I would also like to thank all other members of the research group, Shannon Murray, Manohar Karigerasi, Chengxi Zhao, Meba Gebre, Soumitra Sulekar, Elizabeth Pogue, Jingwen Yu, Shuai Li, and Benjamin Hulbert, *etc.* Working in the same lab required a lot of cooperation and understanding, and I thank you for putting up with the messes that I occasionally created. Thank you all for the help I received from lab works, and also for the knowledge I acquired from interacting with you.

Thanks to all collaborators who have helped in the design and execution of my experiments. I need to thank Shiliang Tian for the help with EPR, Shuqi Lai for the help with NMR, Steven Rogers for the help with micro-Raman, , Danielle Gray and Toby Woods for single crystal XRD and structure solution, Qun Li for ball milling, John Okasinski and Haiyan Chen for EDXRD, and Andrey Yakovenko and Wenqian Xu for synchrotron *in situ* high temperature XRD.

I want to thank all relevant staff members from the University of Illinois who have assisted in the logistics and experiments during my graduate study. Thanks to all the staff members in the Materials Research Laboratory and the Department of Materials Science and Engineering, my graduate study can be carried out smoothly. Thanks to the facilities staffs in

Materials Research Laboratory in training and maintaining the research equipment I used.

I have to thank my family members. I am sorry that I have to stay half a globe away and had so little time to accompany you. But you have given me unconditional mental and financial support on the pursue of my carrier, which I am sincerely grateful at heart. Thank you, mother and father. Having you as parents in the luckiest thing for me and I will always love you.

I thank all the friends of mine. You have made my journey through the graduate study much more enjoyable. Special thanks are given to Shuqi Lai, Cong Xu, Zijian Yang, and Sihan Chen. We have watched great movies, enjoyed palatable meals, and played with exciting games.

Lastly, I would like to thank my witty, charming, and supportive girlfriend, Siyuan Pang. She has brought me joy and cultivated me with positive emotions when I was depressed. Thanks to her, I am able to go through hard days in life with enthusiasm and passion.

TABLE OF CONTENTS

CHAPTER 1

BACKGROUND

1.1 Motivation

Advances in human civilization often parallel, or are based on, significant advances in the ability to obtain and process materials. [1] This is evidenced by our naming of civilization ages. Our prehistoric transition to an agricultural society in the Stone Age benefited from the craftsmanship of natural materials such as stone. Development in the extraction and refining technology allowed scaled access to metals, which paved the establishment of metallurgy and ushered the Bronze and Iron Ages. The remarkable breakthroughs in these times were the synthesis of materials with compositions, phases, and structures not of direct natural origin. The potential to tailor materials properties towards the needs is the basis of modern design and engineering. The Silicon Age is made possible by the establishment of Si crystal growth via the Czochralski process and pushed forward by advances in microfabrication. [2] Evidently, technology leaps stem from progress in the versatility and precision of materials synthesis capabilities, whose advances today demand either innovation in the methodology or gaining fundamental insights on the thermodynamics and kinetics governing reaction outcomes.

The current frontiers of materials research examine materials with functions and syntheses unlike those that have come before. The phenomena of superconductivity [3,4], multiferroics [5,6], photovoltaics [7], just to list a few, all have potential to usher new generations of applied technologies. But just as a good warrior needs a good weapon to fight, a good technology also need the proper materials to perform its core functions. Ultimate performance and utility are bound by material characteristics, which in turn, are based on our accessible materials space. [8, 9] In recent years, there has been an increasing emphasis on moving away from the historical slow and serendipitous trial-and-error methods of discovering and developing materials. [10–15] To accelerate the pace, more systematic and refined practices to understand materials formation chemistry are required. At the heart of the pursuit are these fundamental questions: How to form target materials? What critical factors lead to the formation of these materials? Can new materials be discovered after the realization of these factors?

1.2 Methodology

The following general approach was adopted in my study. Some scientifically or technologically interesting materials were focused upon, and practical methods of synthesizing them were identified. Time-resolved studies were conducted to shed light on the critical factors determining the formation of the target materials using the identified method. The original materials syntheses were later improved by engineering the reactions to avoid unwanted factors and utilize beneficial factors. These critical factors were also applied to other relevant material systems, attempting to discover new materials. The most defining step in the outlined approach is the identification of critical factors.

Thermodynamic principles dictate what products will remain when thermodynamic equilibrium is reached. In a short summary, a transformation of state has a chance to proceed if this transformation lowers the free energy of the system. The dependence of the minimum free energy configuration with respect to composition is often presented in phase diagrams, which are useful guidelines for determining synthesis conditions. Useful online databases for retrieving experimental and theoretical phase diagrams include the ASM Alloy Phase Diagram Database [16], SpringerMaterials [17], Facility for the Analysis of Chemical Thermodynamics [18], *etc.*

Despite the usefulness of these phase diagrams, extra information is often demanded in synthesis. One major problem is that these phase diagrams work best for closed systems with only the components listed, but the presence of any other interfering substances can change the chemical potentials, and therefore change phase stabilities. The absence of a specific phase from the corresponding phase diagram does not rule out the possibility of stabilizing that phase. The phase diagrams also lack kinetic information. It may be unclear whether a specific reaction design can achieve equilibrium in a practical timeframe, or if other non-equilibrium phases within the composition space can actually be made due to the inefficiency of reaching equilibrium. An unconventional kinetic pathway may then reveal hidden jewels of materials structures, but this requires a good examination of important kinetic events during materials formation. [19, 20]

Time-resolved studies are the key steps toward this goal.

A rudimentary way of conducting a time-resolved study is to quench the reaction system in the mid-stage of reaction and examine the systems afterwards. This simple approach has two benefits. First, it enjoys great flexibility in the choice of materials characterization methods, as most tools are developed and optimized for the examination of room temperature samples. Therefore good quality data can usually be obtained. Second, since the sample is not evolving over time, one particular batch of sample can be used for multiple characterizations. Therefore, each quenched sample can receive more comprehensive and accurate examinations. These different pieces of information combine to give a thorough view of the state of the material. However, the *ex situ* quenching approach also suffers two drawbacks. First, each reacted sample has a defined reaction time, so if significant kinetic information covering large time domains is desired, many samples need to be prepared and analyzed, which is inefficient. Second, it is based on the assumption that quenching can effectively freeze the system from its reacting state, which can be a poor assumption. Additionally, in highly sensitive systems with certain sample-to-sample variations that are practically impossible to eliminate, it is hard to decouple the reaction-time effects with sample-to-sample variations.

Due to the above reasons, kinetic data should be obtained using *in situ* techniques where the reaction system is monitored throughout the reaction process. Here I primarily focus on the use of *in situ* X-ray diffraction (XRD) techniques to monitor changes in the crystalline phases. Different *in situ* XRD variations were studied, including lab-source capillary XRD with a built-in tube furnace and other synchrotron-based setups conducted at Advanced Photon Source in Argonne National Laboratory. *In situ* diffraction methods have been developed for about two decades, and they have made great achievements in the instrumentation. However, many *in situ* diffraction studies are concerned with the response of material systems to certain physical stimuli that do not alter the fundamental crystal structures. Examples of these include mechanical testing [21, 22], response to electric field [23], or intercalation [24]. *In situ* diffraction studies of chemical reactions are more complicated due to the time-resolution and reaction containment required. The constant appearing and disappearing of phases often require monitoring a larger range of Q-space. Most *in situ* diffraction studies that concerned with chemical reaction are focused on the temperature of formation of certain materials. [20, 25] But in my work here, the emphasis was placed on the mechanisms governing the reaction and on the discovery of new materials. This required more detailed, systematic examinations of the diffraction patterns throughout the reaction, and more advanced, efficient analyses of diffraction patterns.

In situ diffraction designs are not as mature as the general-purpose characterization tools. Therefore, some work was spent to unravel the practicability and limitations of specific instrumentation with reaction genres. In practice, combinations of *in situ* and *ex situ* quenched approaches were often required to obtain meaningful interpretation for the time-resolved results.

Figure 1.1: Photo showing the autoclave reactor used for carrying out solvothermal syntheses.

1.3 Reaction Types Investigated

My work is concerned mainly with two reaction types. Both types use very generic design with no sophisticated requirement for reactors. Therefore the conclusions reached from the specific studies are expected to be transferable to other materials synthesis schemes of the same reaction types.

The first reaction type is solvothermal chemistry, in which the liquid-state precursor is placed inside a closed reactor that must contain the autogenous pressure from heating. I have conducted solvothermal reactions in two reactor types. The first is the commercially available autoclaves. These autoclaves use Teflon liners to hold the precursors inside steel enclosures (Figure 1.1). Another reactor type uses fresh fused silica glass tubes. The precursors are poured into the fused silica tube pre-sealed with one end, which is later frozen to a solid state by immersing in liquid nitrogen. The quartz tube was then vacuumed and sealed in the middle to create a closed ampoule (Figure 1.2).

Solvothermal synthesis is a versatile and potent method to obtain materials with phase chemistry or microstructure not so readily obtainable by other methods. [26–29] One unique merit of solvothermal chemistry is the ability to induce inorganic crystal formation and transformation at temperatures far below the minimum requirement of similar thermally

Figure 1.2: Photo showing a fused silica tube with solution sealed within for solvothermal reactions.

activated processes. [27] Another strength of solvothermal chemistry concerns the complex interactions within the solution under the high temperature and pressure conditions, which can be easily altered by changing the precursor chemistry and reaction conditions. [30]

The chemical system I tested with this solvothermal approach is Cu_4O_3, which is not a thermodynamically stable form of copper oxide. Inspired by Cu_4O_3 synthesis, the work was extended to test the interaction of copper with other organic substances, with the discovery of various copper-containing materials.

The second reaction type is related to solid state synthesis. This involves working with mixtures of solid-phase chemicals as the starting reagents. The precursor mixtures in this synthesis approach were flame sealed inside fused silica tubes to avoid oxidation, and reacted in box furnaces. Solid state reactions are extremely versatile and potent for the production of multi-element ceramic phases, and easy and cheap to operate. [31–35] Nevertheless, it is a thermally demanding process, and usually requires high temperature, long time, and even multiple cycles to fully achieve equilibrium. This presents a challenge when obtaining material phases whose stability requires low temperature, when kinetics may be too slow.

Traditional studies of solid state synthesis involve examination of the products after cool-

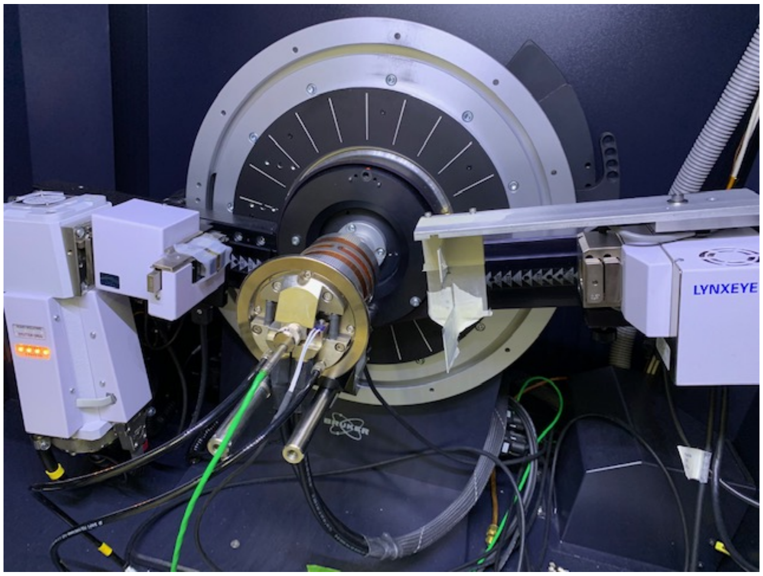

Figure 1.3: Photo showing the instrumentation of the lab *in situ* XRD used. The sample capillary was held within a TC-Transmission furnace with polyimide windows.

ing the samples to room temperature at the end of the reactions. This postmortem approach inevitably overlooks the kinetic events governing the product outcomes. While there were efforts to interrogate solid state reaction *in situ* using synchrotron radiation, the availability of beamline forbids high-throughput exploration of materials space. [36] Here, by using our customized *in situ* XRD setup with a built-in furnace (Fig. 1.3), we demonstrated the capability of our in-house setup to capture key factors regulating inorganic material formation. [37]

My initial focus on solid state reaction was on the formation of the target compound Fe_2SiS_4 with the help of *in situ* XRD. After the identification of peritectic dissociation to be the event leading to Fe_2SiS_4 formation, I devised alternative reaction designs in order to speed up the reaction. Intermetallic sulfidation and particle-size reduction were particularly effective. Inspired by the factors affecting Fe_2SiS_4 formation, I extended these factors to discover new materials in other chalcogenide systems. Evidence of structures that are still unsolved has been obtained from reaction designs that utilize a reactive flux (BaS_3) and ball milling reagents.

1.4 Overview of Chapters

The first half of the dissertation discusses the solvothermal formation of Cu-based inorganic materials. In Chapter 2, the solvothermal formation of an structurally interesting magnetic material Cu_4O_3 is examined using *ex situ* time-resolved study. Reaction mechanisms for the solvothermal reaction are proposed. In Chapter 3, the same reaction is investigated with *in situ* energy-dispersive X-ray diffraction with a synchrotron source, whose results are shown to support the *ex situ* conclusions. In Chapter 4, the effects of different chemistries on the solvothermal stability of Cu-containing inorganic materials are tested. It is shown that the solvothermal stabilities of Cu-containing materials are very dependent on solvent chemistry. Up to four new crystalline phases are discovered. In Chapter 5, the structure of a newly discovered tri-ethylenediamine complex of Cu is solved and discussed in detail.

The second half of the dissertation discusses solid state formation of ternary chalcogenides. In Chapter 6, the kinetics of the formation of Fe_2SiS_4 are investigated primarily with *in situ* X-ray diffraction. The source of the kinetic barrier to Fe_2SiS_4 formation is suggested. Several approaches to overcome or circumvent the barriers are demonstrated. In Chapter 7, inspired by the effect of burst formation of superheated liquid on material formation kinetics, flux-assisted crystallization of new Ba–Fe–S structures is investigated. Five potential new structures are discovered. In Chapter 8, based on the effect of ball-milling to increase reaction kinetics, new materials discovery is attempted in various ternary sulfide and selenide systems. The existence of three new sulfide materials are discovered, which can be accessed by ball-milling reagents but not with only mortar-and-pestle grinding.

CHAPTER 2

EX SITU INVESTIGATION OF SOLVOTHERMAL Cu_4O_3 FORMATION

I chose to investigate the formation of Cu_4O_3 as the starting point of demonstrating the influence of thermodynamics and kinetics on inorganic crystal formation with solvothermal synthesis. Solvothermal reactions bear large degrees of freedom for the control of synthesis conditions. This means that a wide range of chemicals can be chosen to alter the chemical potentials for crystallization, and therefore a wide thermodynamic landscape can be explored. But at the same time, solvothermal chemistry can access above-boiling-point temperature during reaction. This means the reaction system has appreciable kinetics to allow different types of inorganic materials to be crystallized. [38,39] Cu_4O_3 is chosen as the target material, for this compound has interesting physical properties and applications, but is known to be extremely hard to synthesize.

2.1 Introduction

The binary copper oxide family of cuprous oxide Cu_2O, cupric oxide CuO, and paramelaconite Cu_4O_3 has numerous functional applications due to their unique structures and electronic configurations. Cu_2O rectifiers were commonplace before the introduction of Si diodes. [40] Cu_2O is a natural p-type semiconductor, and has been extensively applied in solar cells and optoelectronic devices. [41–46] Recently, attention has turned to excitonic Bose-Einstein condensation [47–49] and spin-phonon interaction [50] in Cu_2O, as well as electron-phonon coupling [51] and spin-phonon interactions [52] in CuO. Both Cu_2O and CuO are also prevalent in catalysis, [53–55] gas sensing, [56] electrochromism, [57] spintronics, [58, 59] and lithium ion battery research. [60–62]

Less is known about paramelaconite Cu_4O_3 due to its scarcity and the complexities of its synthesis. After its discovery in the Copper Queen mine (Bisbee, Arizona, USA), [63] its structure was determined to be tetragonal $I4_1/amd$ (Figure 2.1(A)). [64, 65] It is a mixed-valence compound with equal numbers of two-fold linearly-coordinated Cu^+ and four-fold square-planar Cu^{2+} ions. The spin-active Cu^{2+} sublattice in Cu_4O_3 is an analog of the pyrochlore lattice (Figure 2.1(B)). Oxides of the pyrochlore structure type are a quintessential class of geometrically frustrated magnets. [66] Long-range ordered (*e.g.* $Er_2Ti_2O_7$), [67] spin-glass (*e.g.* $Y_2Mo_2O_7$), [68] spin-ice (*e.g.* $Ho_2Ti_2O_7$) [69] and spin-liquid (*e.g.* $Yb_2Ti_2O_7$) [70] phases have all been observed within the class. Unlike most pyrochlore lattices featuring rare-earths or transition metals with large spins, Cu_4O_3 has $S = 1/2$ magnetic Cu^{2+} ions, and may be expected to exhibit maximized quantum effects. [71] These interactions have most recently been studied in a 2D material, Herbertsmithite $ZnCu_3(OH)_6Cl_3$. [72] Surprising for a frustrated material is the fact that Cu_4O_3 has a relatively high antiferromagnetic Néel temperature $T_N = 42$ K. [71] Whangbo and Koo suggested that low-dimensional magnetism in the square-planar chains may be more dominant than magnetic frustration in Cu_4O_3. [73] However, impurities in the mineral origin Cu_4O_3 sample rendered low quality data that impeded complete resolution of its spin configuration. Moreover, the optical and electronic properties of Cu_4O_3 have remained unexplored to date. [46]

The synthesis of high purity Cu_4O_3 is hampered by its metastability. Hybrid density functional theory calculations and experimental calorimetry have shown that Cu_4O_3 is not a thermodynamically stable phase and decomposes to CuO and Cu_2O when heated to 300–500°C. [74,75] Because of this, early studies of Cu_4O_3 were restricted to mineral samples with limited data quality due to impurities. [71] Previous liquid-phase Cu_4O_3 synthesis attempts include the extraction of mixed oxides from concentrated aqueous ammonia [76] and the sonochemical conversion of copper(II) acetate in aniline. [77] However, these methods suffer from low Cu_4O_3 yield and small crystal size. Alternative Cu_4O_3 synthesis routes are available

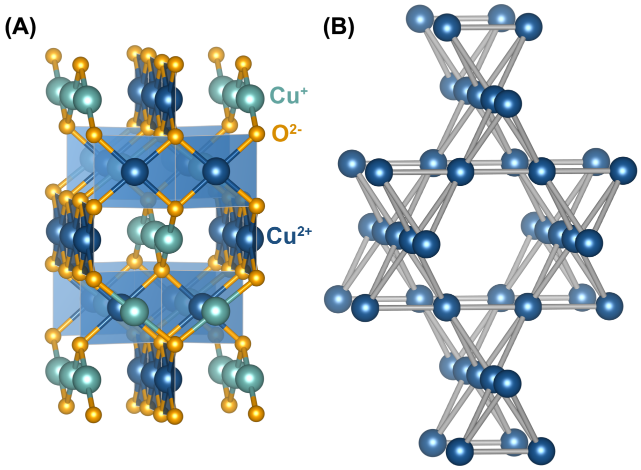

Figure 2.1: (A) Crystal structure of Cu_4O_3. (B) Shown to scale, the spin-1/2 Cu^{2+} sites in Cu_4O_3 form a pyrochlore sublattice.

for thin films, including chemical vapor deposition, [78] Cu_4O_3 reduction in an electron microscope, [79] Cu oxidation in water using laser ablation, [80] and electrochemical cycling of CuO films. [81] However, these methods created only traces of Cu_4O_3. Reactive magnetron sputtering with controlled oxygen flow is currently the most successful Cu_4O_3 film preparation method. [82] Unfortunately, the resulting films are highly textured and contain cracks due to high stress, which limit their applicability for physical properties measurements. The controlled synthesis of Cu_4O_3 crystals with reliable phase purity remains a challenge.

A solvothermal reaction scheme for Cu_4O_3 was recently discovered by Zhao *et al.* [83] Hydrothermal and solvothermal reactions are commonly used to access oxide phases and morphologies that are metastable with respect to solid state conditions. [84–86] In Zhao *et al.*'s scheme, Cu_4O_3 microspheres were produced by reacting a $Cu(NO_3)_2{\cdot}3H_2O$ precursor in a mixed ethanol and dimethylformamide (DMF) solvent. [83] Our attempts to reproduce this reaction were less satisfactory, with only impure Cu_4O_3 forming and a strong preference for nucleation of disparate phases on the rough surfaces of the Teflon autoclave liner.

In this effort, we investigated this reaction scheme in a time-resolved manner by quenching the reaction at various reaction conditions and thoroughly examine the quenched states *ex situ*. This allowed the creation of kinetic reaction maps that provide an overview of phase development. The intrinsic variability of the products was reduced by carrying out reactions in sealed fused silica tubes. Microscopic and spectroscopic observations revealed structural correlations between different crystalline phases. These systematic studies move us closer to an understanding of the reaction mechanisms. We show that the ethanol-induced mineralization of $Cu(NO_3)_2 \cdot 3H_2O$ into $Cu_2(NO_3)(OH)_3$ is followed by DMF-induced reductive conversion of $Cu_2(NO_3)(OH)_3$ into Cu_4O_3.

2.2 Synthesis and Characterization

Ethanol and dimethylformamide (DMF) were mixed in a 2:1 volume ratio to form the reaction solvent. $Cu(NO_3)_2 \cdot 3H_2O$ was dissolved in this solvent to specified concentrations (either 70 or 50 mM) to make precursor solutions. In autoclave attempts, 18 mL of the precursor solution was placed in a 23 mL capacity Teflon-lined autoclave (Parr Instruments). In sealed tube attempts, 15 mL of the precursor solution was poured into a fused silica tube with 16 mm outer diameter (O.D.) and 14 mm inner diameter (I.D.). The end of the tube was submerged into liquid nitrogen to freeze the solution. The tube was then evacuated and sealed. In both autoclave and tube reactions, the precursor solution was placed in an oven pre-heated to 130°C, held for a specific amount of time, then removed from the oven and air-cooled to room temperature. The tubes were tilted about 30° from vertical during reactions. The products were collected and centrifuged to separate the liquid and solid phases. All silica tube reactions presented here were prepared from the same two batches (50 mM and 70 mM) of precursor.

Fourier transform infrared (FTIR) spectra of the liquid samples were collected on a Thermo Nicolet Nexus 670 spectrometer with an attenuated total reflection attachment. ^1H nuclear magnetic resonance (NMR) spectra of the liquid samples were recorded on a Varian U500 (500 MHz) with a mixture of DMF-d_7 and ethanol-d_5 (1:2 v/v) as an external standard and one peak of DMF-d_7 at 2.74 ppm was used for referencing spectra. Inductively coupled plasma–optical emission spectroscopy (ICP-OES) measurements of the liquid samples were performed with a Perkin-Elmer 2000DV spectrometer. The liquid samples were dried in ICP tubes for 2 days at room temperature prior to ICP-OES measurement. X-band electron paramagnetic resonance (EPR) spectra of the liquid samples were collected at 77 K on a Varian-122 spectrometer equipped with an Air Products Helitran cryostat and temperature controller, with a collection frequency of 9.29 GHz, power of 0.2 mW and field modulation of 4.0 G. EPR spectrum was simulated with SIMPOW6. [87] Ultraviolet-visible (UV-Vis) spectroscopy measurements for the liquid samples were performed on a Varian Cary5G spectrometer with transmission attachment, with source and detector changeover both at 600 nm. The undiluted samples were used to record the UV-Vis spectra from 350 to 1000 nm, while samples diluted to 4 vol% with ethanol were used to record the spectra from 290 to 450 nm. All light path lengths were 1 cm in this study.

Powder X-ray diffraction (XRD) patterns of the solid samples were collected on a Bruker D8 ADVANCE diffractometer equipped with a Mo-K_α source and LYNXEYE XE detector in transmission geometry. Rietveld refinements were performed using Bruker TOPAS 4.2 Suite. Scanning electron microscopy (SEM) images of Au/Pd-coated samples were taken with a JEOL JSM-6060LV microscope with 15 kV acceleration voltage. Micro-Raman spectra of the solid samples were acquired on a Jobin Yvon Labram HR800 micro-Raman spectrometer with 532 nm laser excitation (laser spot size $\sim$ 1 µm) with laser intensity around 3 µW/µm^2. The samples were spread over standard glass microscope slides for micro-Raman measurements. Visible light microscopy images associated with the micro-Raman studies were taken with Olympus BX41 microscope. Crystal structures were visualized using VESTA. [88] Magnetization measurements were performed using a Quantum Design MPMS3 operating in DC mode with a sample mass of 12.2 mg in a standard snap-shut powder capsule in a brass trough holder.

2.3 Results and Discussion

2.3.1 Variability of Reactions in Teflon Versus Fused Silica

We initially attempted the synthesis described by Zhao *et al.* [83] and reacted 50 mM and 70 mM $Cu(NO_3)_2 \cdot 3H_2O$ in 2:1 volume ratio ethanol:DMF at 130 °C in Teflon-lined autoclaves. The liquid phase changed color and various amounts of Cu_4O_3, $Cu_2(NO_3)(OH)_3$, Cu_2O and CuO were obtained.

The above reactions in Teflon-lined autoclaves led to inconsistent proportions of crystalline phases. Furthermore, different solid products were found adhering to different surfaces (walls versus bottom) of the liners. The conspicuous difference in roughness of these two surfaces and the difficulty of fully cleaning the liners between reactions precluded a systematic investigation of Cu_4O_3 synthesis using this technique.

To reduce reaction variability we performed syntheses in fused silica tubes as described in Section 2.2. Variations in products were minimized and improved reproducibility was seen over Teflon-contained reactions because a new fused-silica tube was used for every reaction.

2.3.2 State of Solvated Copper Ions: ICP-OES, EPR, and UV-Vis

At various times, we quenched the reaction and separated the liquid from the precipitates. The liquids were interrogated with FTIR and NMR. Within the sensitivity of these two techniques, no new organic species were identified, and the ratio between DMF and ethanol remained unchanged.

Shifts in the NMR spectra imply removal of solvated Cu from the liquid, which we quantified by ICP-OES and EPR. Both ICP-OES and EPR give a linear relationship between intensity and Cu concentration. ICP-OES is not sensitive to copper valence, and gave initial total copper concentrations of 67.5 mM and 49.8 mM for the nominal (unreacted) 70 mM and 50 mM solutions.

In contrast to ICP-OES, EPR probes the $S = 1/2$ Cu^{2+} species only, and is insensitive to diamagnetic Cu^+. The EPR spectra for reacted liquids are shown in Figure 2.2(A,B). The EPR spectra have the same shape with intensity scaling linearly. The EPR g-values are anisotropic and the $g_{\|}$ component has four hyperfine lines due to the hyperfine coupling of the electron spin to the Cu nucleus with $I = 3/2$. This indicates type-II Cu sites, typical of Cu^{2+} complexes in solution with elongated octahedral geometry. [89, 90] Simulations of the EPR spectra give $g_{\|} = 2.38$, $g_{\perp} = 2.07$, and $A_{\|} = 139 \times 10^{-4}$ cm^{-1}. Relative Cu^{2+} concentrations between different reaction times were calculated based on the peak intensities of the EPR signals at magnetic field $H = 3186$ G.

At 0 h reaction time, the concentrations from ICP-OES and EPR correspond to 100% Cu^{2+}. The difference in the ICP-OES and EPR signals is therefore proportional to the diamagnetic Cu^+ ion concentration. The progressions of solvated Cu ions from ICP-OES and EPR are shown in Figure 2.2(C,D) for 70 mM and 50 mM precursor concentrations, respectively. Both Cu^{2+} and total Cu ion concentrations decreased quickly with time, commensurate with precipitation of >95% of the total solvated copper after 5 hours.

ICP-OES and EPR show that Cu^+ did not exist at the start of the reaction, peaked in concentration at 2 hours, then decreased to a small, steady value after 5 hours. Maximum Cu^+ concentrations for both precursor conditions were similar: 12.6% for 70 mM and 12.5% for 50 mM. In the final steady-state (>7 h), the system reached *ca.* 1.0% Cu^+ concentration and <0.4% Cu^{2+} concentration with 70 mM precursor, and *ca.* 1.2% Cu^+ concentration and *ca.* 0.8 Cu^{2+} concentration with 50 mM precursor.

For the 70 mM precursor after 1 h reaction, the relative EPR signal was slightly greater than that of ICP-OES (2.5%), which implies an unphysical negative Cu^+ concentration. It may be caused by inexact dilution, as in the discrepancy between our initial nominal 70 mM solution and the ICP-OES value (67.5 mM). This does not obscure the most important feature: reactions with both precursor concentrations show a clear maximum in Cu^+ concentration around 2 h.

Drastic changes in the liquid color were observed during the reduction of Cu^{2+} to Cu^+ (blue

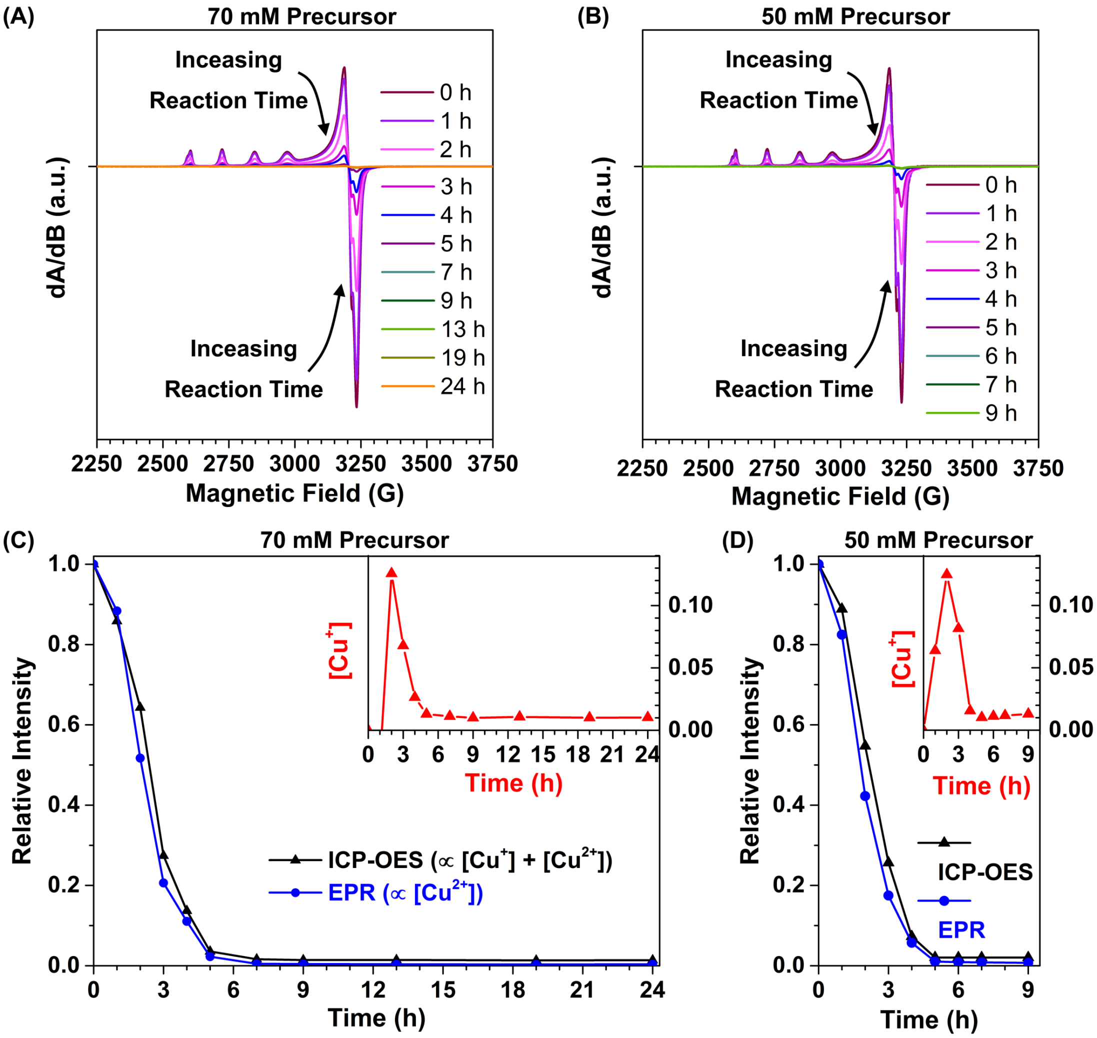

Figure 2.2: EPR spectra for the liquid phase after reactions of (A) 70 mM and (B) 50 mM $Cu(NO_3)_2{\cdot}3H_2O$ in 2:1 v/v ethanol:DMF at 130°C. The insets in (C) and (D) show the variations in Cu^+ concentration, calculated as the difference between total Cu (ICP-OES) and Cu^{2+} (EPR) concentrations. Cu^+ concentrations for both sets of reactions peaked at 2 hours before dropping to a small value after 5 hours.

to green to orange), captured in detail by UV-Vis spectroscopy. The spectra are displayed in Figure 2.3 for reactions starting with 70 mM and 50 mM precursors.

The unreacted '0 h' sample ($Cu(NO_3)_2{\cdot}3H_2O$ dissolved in ethanol/DMF) in Figure 2.3 has two major optical absorption features: strong UV absorbance at wavelengths below 400 nm, and a visible/near-IR peak at 800 nm responsible for the brilliant blue color. These spectra agree well with the Cu^{2+} electronic absorption spectra probed with EXAFS by Inada *et al.*, where they showed the solvation structure of Cu^{2+} is 6-coordinate octahedral in solvents including ethanol, methanol, and dimethyl sulfoxide. [91]

The near-total depletion of Cu^{2+} from solution seen in ICP-OES/EPR is corroborated by the weakening of the 800 nm absorption mode after 5 hours (dashed lines in Figure 2.3(B,D)). The slight blueshift of this peak from 2-3 h is probably due to Cu^{+}, which exhibits maximum absorbance at a smaller wavelength ($\sim$750 nm).

The peak in Cu^{+} intensity seen by ICP-OES/EPR is most likely the cause of the extended UV shoulder that reaches 530 nm after during 2-3 hours of reaction (solid and dashed lines in Figure 2.3(B,D)), then recedes below 400 nm for longer reaction times.

Intriguingly, a sharp new absorption peak appeared at 413 nm. The inset in Figure 2.3(B,D) depicts this new peak and the Cu^{+}-driven broadening of the UV absorption more clearly. The 413 nm peak only increases after long reaction times and we have not been able to assign this peak to any solvated copper species. It may arise from trace amounts of organic species yet to be identified, but no corresponding new contributions were seen in NMR or FTIR.

2.3.3 Progression of Precipitated Phases: XRD

XRD patterns for the *ex situ* quenched samples at various reaction times are shown in Figure 2.4. Four crystalline phases were identified by powder XRD, and are shown in Figure 2.5. Rietveld refinement is necessary to deconvolute the patterns and obtain quantitative phase fractions of $Cu_2(NO_3)(OH)_3$, CuO, Cu_2O, and Cu_4O_3. A representative Rietveld

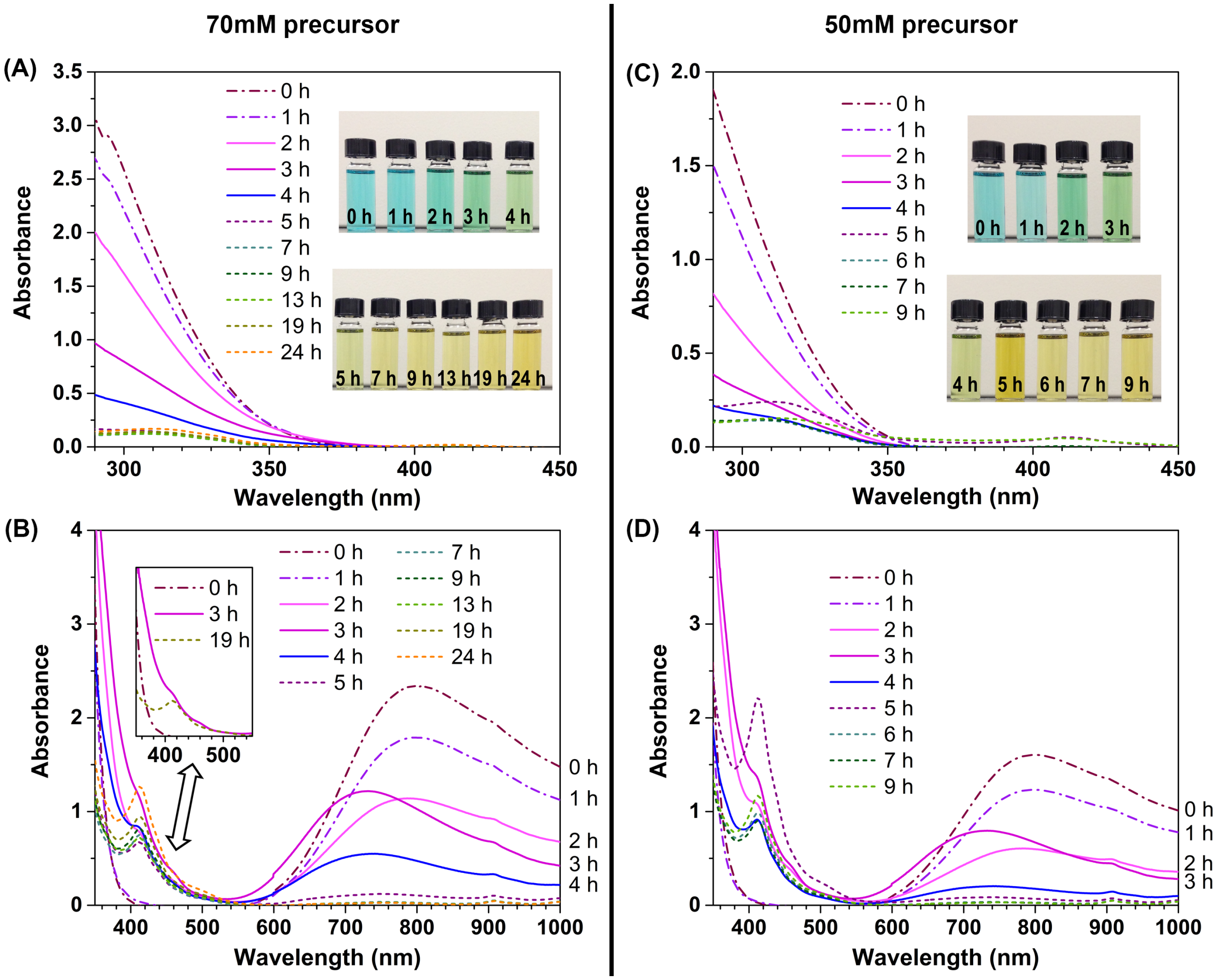

Figure 2.3: UV-Vis spectra for the liquid phase ((A,B) 70 mM and (C,D) 50 mM $Cu(NO_3)_2{\cdot}3H_2O$ in 2:1 v/v ethanol:DMF at 130 °C): (A,C) diluted samples (to 4 vol % with ethanol), (B,D) undiluted samples. The photographs in (A,C) show the change in color. In (B,D), disappearance of the peak around 800 nm (dashed lines) is consistent with depletion of Cu^{2+}. The broad extension in UV-centered absorption from 410 nm (dash-dot) to 530 nm (solid and dashed) suggests Cu^{+} is responsible for this absorption mode in late reaction stages. A sharp peak at 413 nm is also observed to appear after long reaction times (dashed). The inset in (B) displays selected spectra to highlight the 413 nm peak and extension of the UV shoulder.

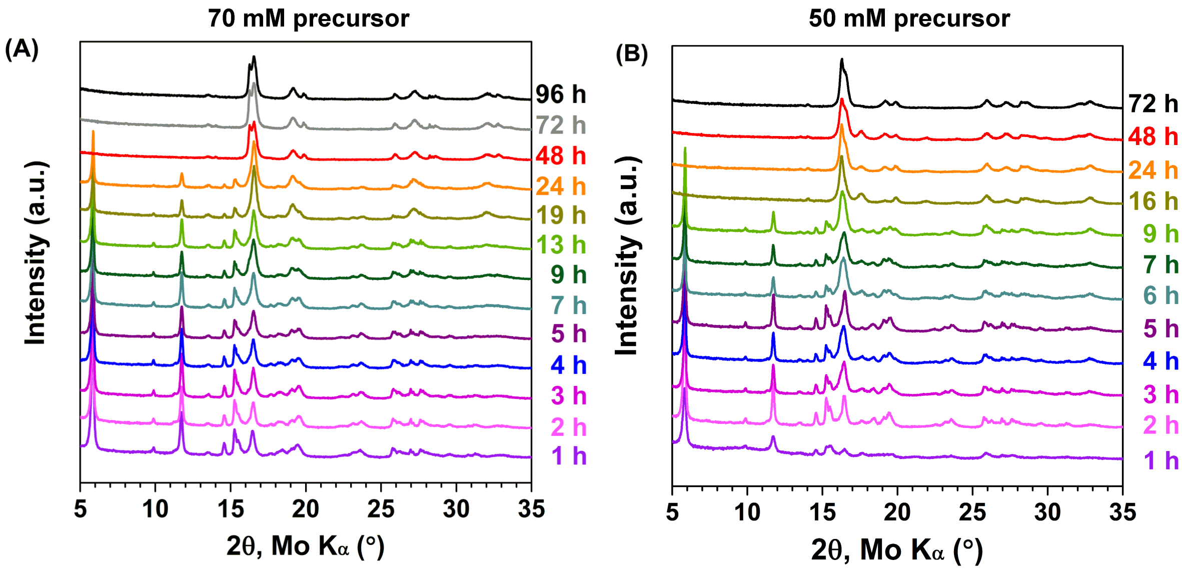

Figure 2.4: XRD patterns for the solid phases after the reaction of $Cu(NO_3)_2{\cdot}3H_2O$ in 2:1 v/v ethanol:DMF at 130 °C with (A) 70 mM precursor and (B) 50 mM precursor concentration.

refinement result is shown in Figure 2.5(A), which depicts the XRD pattern of the 9 hour reaction products from a 70 mM precursor. In this case, Rietveld refinement can separate the contributions from $Cu_2(NO_3)(OH)_3$, Cu_2O, and Cu_4O_3 nicely, even though the peaks partially overlap around 16.5°. At long reaction times (top of Figure 2.4), the two peaks of Cu_2O and Cu_4O_3 are easily resolved.

The quantitative amount of Cu contained in each precipitated crystalline phase as a function of reaction time is shown in Figure 2.5(B,C) for 70 mM and 50 mM precursor reactions, respectively. The total crystalline Cu content at each reaction time is scaled by the amount of Cu lost from the liquid phase since the start of the reaction based on our ICP-OES measurements. We assumed the existence of no amorphous content in this analysis.

In both 70 mM and 50 mM precursor reactions, $Cu_2(NO_3)(OH)_3$ was the first to precipitate and was the dominant solid phase in the early stages, with its maximum amount at 5 h. Eventually, it disappeared in both reaction systems (after 48 h for 70 mM, and 16 hours for 50 mM).

In both sets of reactions, solvated Cu ions declined to a few percents of their initial

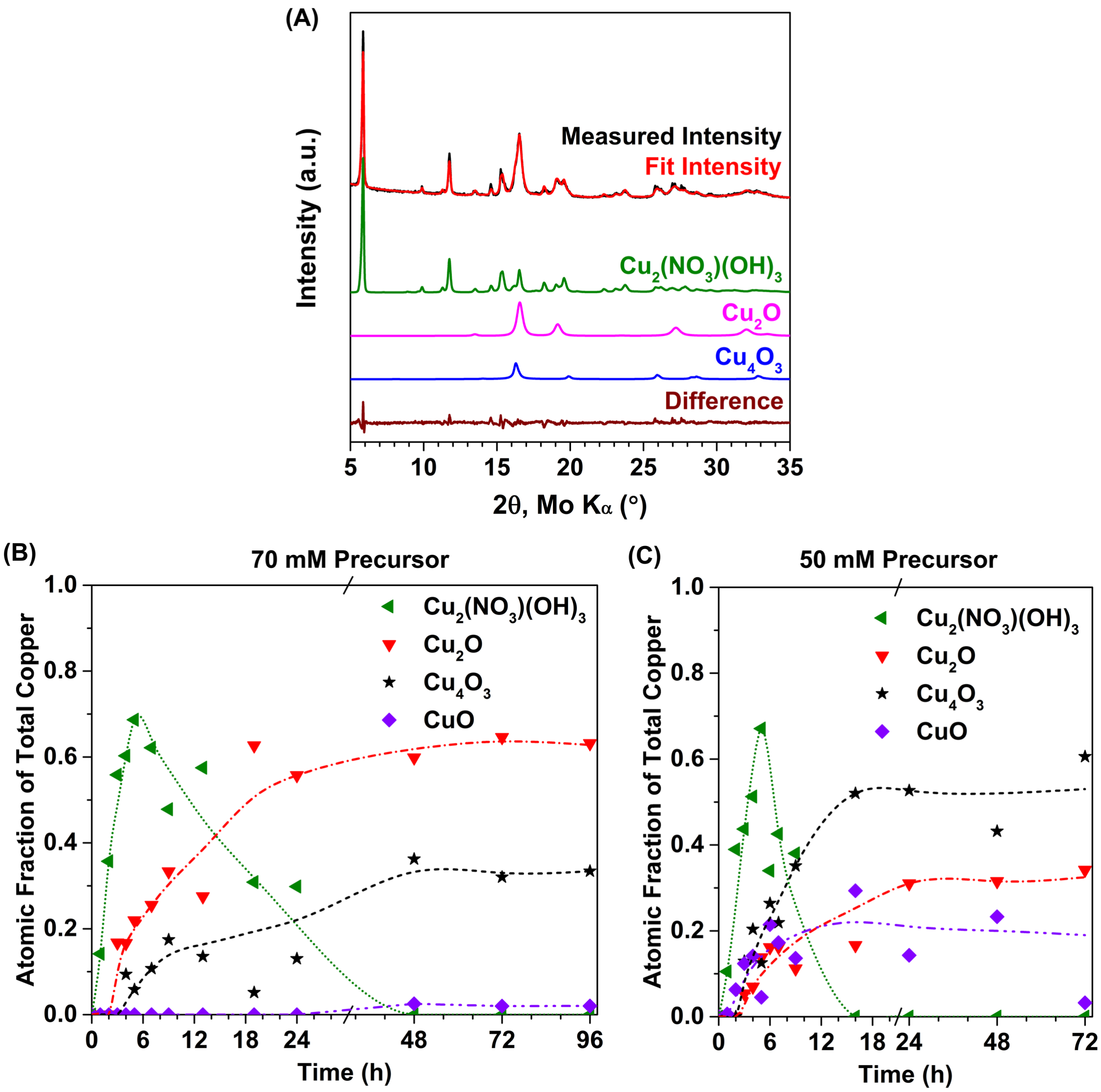

Figure 2.5: (A) Rietveld refinement of the '9 h' XRD pattern in Figure 2.4(A). The evolution of the solid phases with time is shown for (B) 70 mM and (C) 50 mM precursors. Solid phases are normalized to the relative mole amounts of Cu atoms in the phases. The lines in (B) and (C) are visual guides. $Cu_2(NO_3)(OH)_3$ arose as an intermediate product in both cases, but the evolution of binary oxides depended on the precursor concentration. The amount of Cu_4O_3 stabilized once all $Cu_2(NO_3)(OH)_3$ had been consumed for both precursor concentrations.

concentrations after 5 h (Figure 2.2(C,D)), but the amount of binary copper oxides continued to increase after 5 h. Due to the small amount of Cu in solution, the growth of copper oxides must occur by the consumption of $Cu_2(NO_3)(OH)_3$ after 5 h.

In 70 mM precursor reactions, the oxides formed were dominated by Cu_2O and Cu_4O_3, with only a minuscule amount of CuO detected after 48 hours (Figure 2.5(B)). The majority product, Cu_2O, had stabilized in quantity by 19 h. Beyond 19 h, the trends in Figure 2.5(B) imply that Cu_4O_3 continued to form at the expense of $Cu_2(NO_3)(OH)_3$ until 48 h when $Cu_2(NO_3)(OH)_3$ was finally consumed.

When $Cu(NO_3)_2{\cdot}3H_2O$ precursor concentration was 50 mM, CuO appeared during the early stages of the reaction, resulting in a more complex progression of solid phases seen in Figure 2.5(C). All three copper oxides precipitated concurrently. The fraction of Cu_4O_3 was greater than the reactions with 70 mM precursor. Here, as in the 70 mM precursor reactions, the fraction of Cu_4O_3 remained stable after $Cu_2(NO_3)(OH)_3$ was consumed after 16 h.

2.3.4 Kinetic Reaction Maps

Kinetic maps of the solvothermal reaction were constructed by combining our findings from ICP-OES, EPR, and XRD, and are shown in Figure 2.6(A,B) for 70 mM and 50 mM precursor concentrations respectively. In Figure 2.6, the vertical span of each color block represents the quantity (total incorporated Cu ions) of the corresponding copper-containing species as a function of reaction time. The traces of the blue and orange points in Figure 2.6 mirror the signal intensities of ICP-OES and EPR in Figure 2.2(C,D), giving concentrations of total solvated Cu ions and solvated Cu^{2+} (blue region), with the difference thus being the solvated Cu^{+} (orange region). The remaining regions correspond to the solid phase fractions from quantitative Rietveld refinements to the XRD patterns (Figure 2.5(B,C)).

The kinetic maps provide a concise summary of how copper ions are distributed throughout these reactions. By comparing Figure 2.6(A) and Figure 2.6(B), it is clear that changing the $Cu(NO_3)_2{\cdot}3H_2O$ precursor concentration from 70 mM to 50 mM increases the

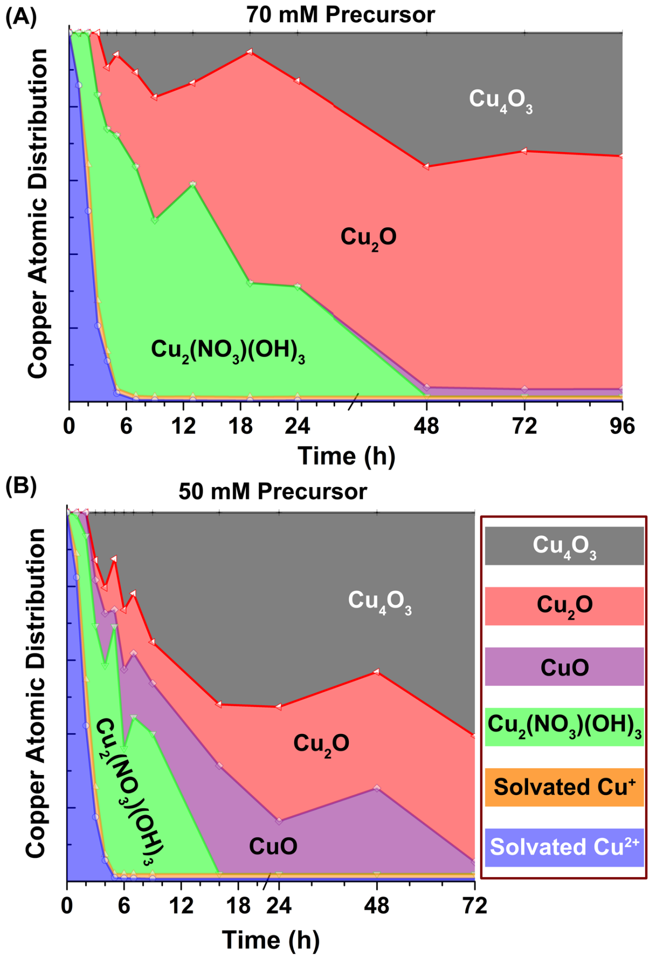

Figure 2.6: Kinetic evolution of each copper-containing species (both in liquid and solid) when reacting $Cu(NO_3)_2{\cdot}3H_2O$ in 2:1 v/v ethanol:DMF at 130 °C with (A) 70 mM and (B) 50 mM $Cu(NO_3)_2{\cdot}3H_2O$ precursor. This is a concise depiction of the impact of precursor concentration on $Cu_2(NO_3)(OH)_3$ consumption rate, oxide phase formation, and the yield of Cu_4O_3.

$Cu_2(NO_3)(OH)_3$ consumption rate and increases the yield of Cu_4O_3, despite the increased stability of CuO. It can also be verified from Figure 2.6 that the quantity of Cu_4O_3 stabilizes once all $Cu_2(NO_3)(OH)_3$ has been consumed.

2.3.5 Microstructure Evolution: SEM and Micro-Raman Spectroscopy

Since the long-term goal of growth of at least micron-sized pure Cu_4O_3 crystals is yet to be realized, the structural evolution of the competing phases in this reaction needs to be understood. The first precipitation product, $Cu_2(NO_3)(OH)_3$, was easily isolated as the lone solid product in short reactions and was identified by SEM as clusters of flat plates, seen by us (Figure 2.7(A)) and others. [83] The remaining oxide phases were impossible to differentiate via SEM, even with the aid of energy dispersive X-ray spectroscopy. We turned to the complementary techniques of visible light microscopy (VLM; $Cu_2(NO_3)(OH)_3$ and Cu_2O have distinctive emerald and red colors, respectively) and micro-Raman spectroscopy with a $\sim$1 µm spot size for unambiguous phase identification of small particles.

SEM micrographs of 70 mM reaction products reveal the nucleation of spherical particles on the surface of $Cu_2(NO_3)(OH)_3$ plates in Figure 2.7(B-F). At 3 or 4 hours of reaction (Figure 2.7(B,C)), spherical particles appeared on the surfaces of these large plate aggregates. Figure 2.7(C) shows that some of the spheres were partially embedded within the $Cu_2(NO_3)(OH)_3$ aggregates. This was most apparent for spheres with relatively large sizes ($\sim$4 µm). This motif of spherical particles on large $Cu_2(NO_3)(OH)_3$ plates remained the main feature until 24 h. As the amount of $Cu_2(NO_3)(OH)_3$ plates diminished, the spherical particles grew in size and abundance (Figure 2.7(E)). The size distribution of spheres seemed roughly bimodal, with the largest spheres growing to be around 10 µm. The surfaces of some spheres became corrugated (Figure 2.7(F)) after multiple days of reaction.

Separate nucleation events produced self-assembled thin films composed of spherical particles after 7 h (Figure 2.7(D)). The solvothermal reactions were carried out with the silica tube slanted, making the lower tube surface concave up and the upper tube surface concave

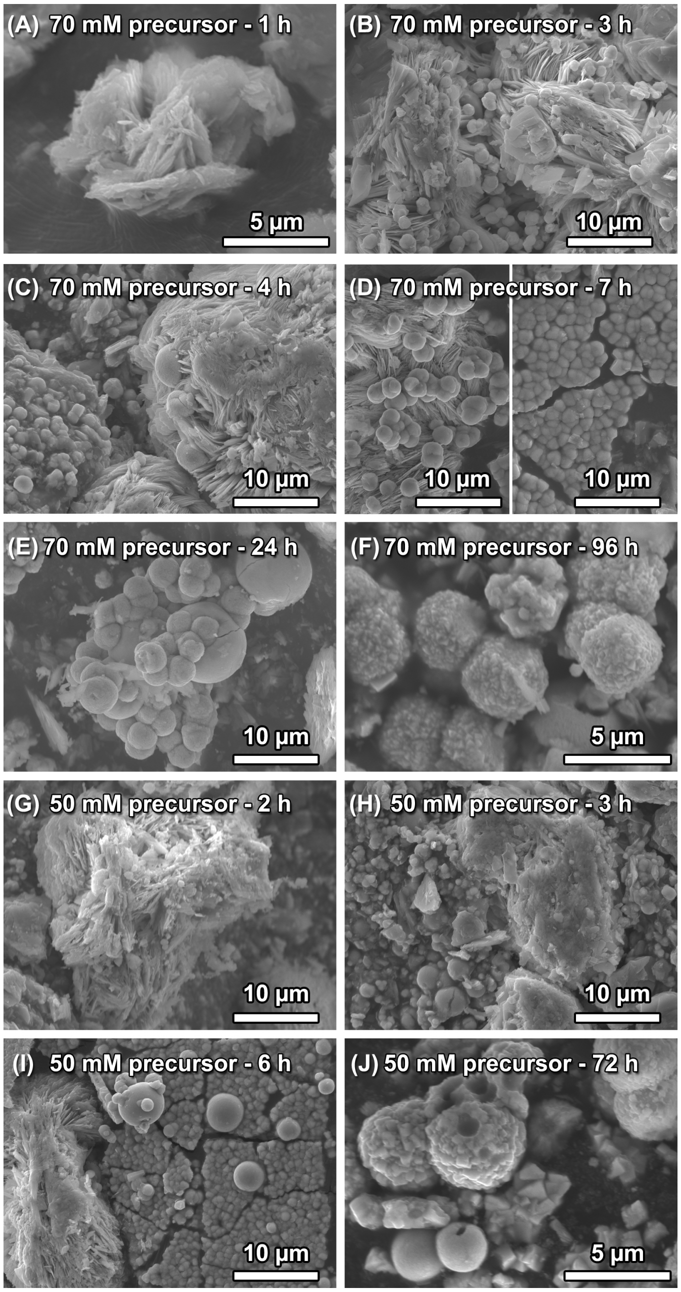

Figure 2.7: SEM images of 70 mM precursor samples reacted for (A) 1 h, (B) 3 h, (C) 4 h, (D) 7 h, (E) 24 h, and (F) 96 h. SEM images of 50 mM precursor samples reacted for (G) 2 h, (H) 3 h, (I) 6 h, and (J) 72 h. The plate-like structures are $Cu_2(NO_3)(OH)_3$. Spherical particles (binary copper oxides) were found to nucleate on the surface of these $Cu_2(NO_3)(OH)_3$ plates at the beginning of the reaction. For reaction times > 24 h, spherical particles varied in size, coarsening, and location.

down. The self-assembled thin films were exclusively seen on the concave down side of the silica wall, opposite to the concave up silica wall where the plates and other spheres were found. These films persisted after long reaction times (not explicitly shown in Figure 2.7 beyond 7 h).

The 50 mM precursor series, despite having different phase composition, experienced similar morphology development as seen in SEM. $Cu_2(NO_3)(OH)_3$ plate aggregates appeared first, followed by spheres attached to the $Cu_2(NO_3)(OH)_3$ surface (Figure 2.7(G,H)). Self-assembled films of spheres also appeared (Figure 2.7(I)), and after the full consumption of $Cu_2(NO_3)(OH)_3$, some spheres' surfaces became corrugated (Figure 2.7(J)).

Micro-Raman spectroscopy permits phase assignment of individual particles in these samples because the Raman peaks for the 4 solid phases are well-separated. The four Raman spectra in Figure 2.8(A-D) are selected single-phase micro-Raman scans from this study: Figure 2.8(A) from 70 mM precursor - 1 h, Figure 2.8(B,C) from 70 mM precursor - 9 h, and Figure 2.8(D) from 50 mM precursor - 2 h. Even though our micro-Raman spectra were collected from micron-sized single particles, the results are consistent with Debbichi *et al.*'s report. [92] Micro-Raman spectroscopy also verified that the particle color viewed by VLM can provide phase information (Figure 2.9(A,B)): emerald blocks are $Cu_2(NO_3)(OH)_3$, red particles are Cu_2O, and shiny black spheres are either Cu_4O_3 or Cu_2O.

Micro-Raman spectroscopy confirmed the nucleation of Cu_2O spheres on $Cu_2(NO_3)(OH)_3$ plates as early as 3 h in a 70 mM precursor reaction (Figure 2.8(E)). As in SEM, spherical particles (*ca.* 1 μm) adhering to large aggregated plates were seen in VLM. Micro-Raman spectra showed that the emerald body is indeed $Cu_2(NO_3)(OH)_3$, and when the laser probe is focused around the red spheres, the 219 cm^{-1} peak (unique to Cu_2O) appeared (Figure 2.8(E)-right). Such phase identification is consistent with our XRD analysis (Figure 2.5(B)).

The spheres attached to $Cu_2(NO_3)(OH)_3$ plates were identified as a mixture of Cu_2O and Cu_4O_3 when the reaction was extended to 4 h (with 70 mM precursor) (Figure 2.8(F)). VLM observations showed that the spheres at this stage had two colors: red and black (Figure

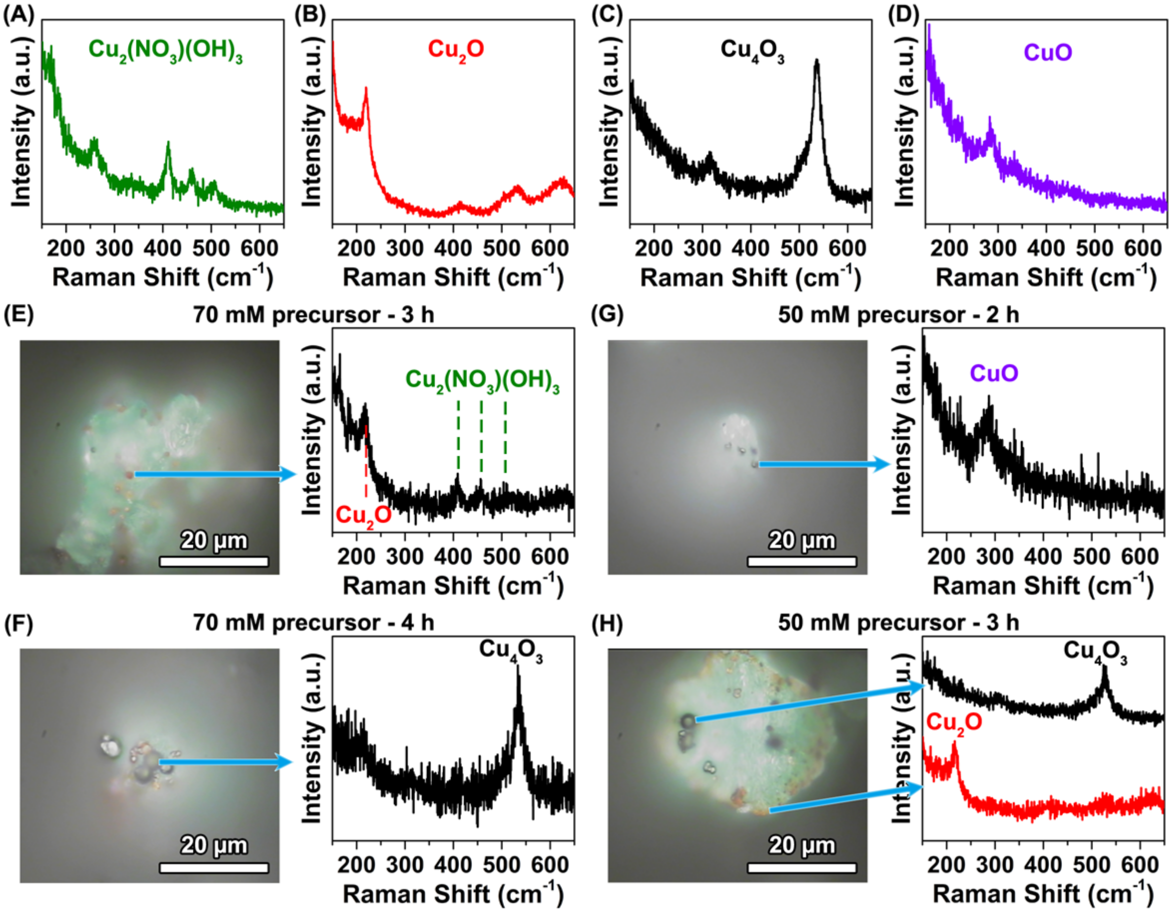

Figure 2.8: Micro-Raman spectra of (A) $Cu_2(NO_3)(OH)_3$, (B) Cu_2O, (C)Cu_4O_3, and (D) CuO. Visible light microscopy images and the corresponding micro-Raman spectra of (E) 70 mM precursor - 3 h, (F) 70 mM precursor - 4 h, (G) 50 mM precursor - 2 h, and (H) 50 mM precursor - 3 h samples. Micro-Raman analysis shows that particles of all three binary copper oxides can be found on $Cu_2(NO_3)(OH)_3$ plates, and that Cu_4O_3 spheres tend to be larger than Cu_2O or CuO.

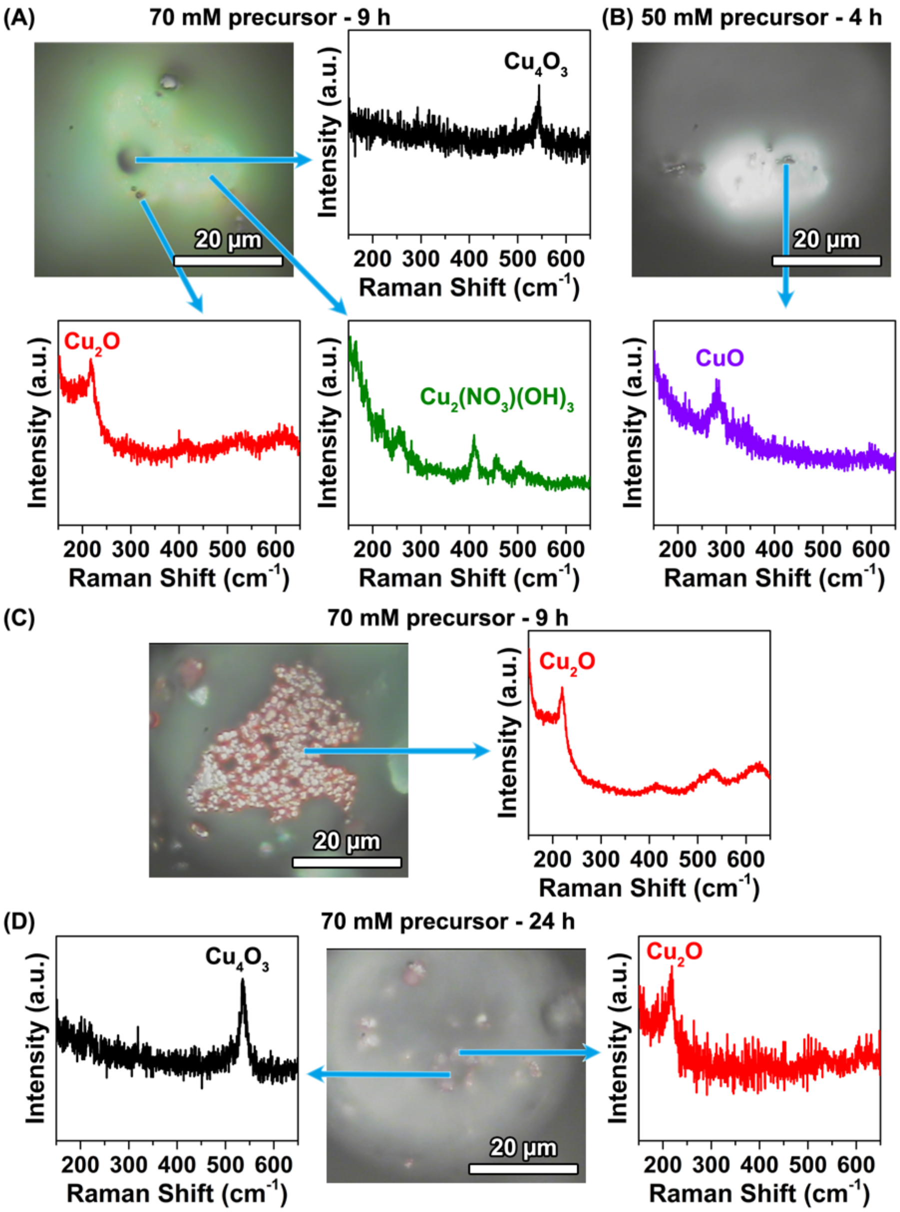

Figure 2.9: Visible light microscopy images and the corresponding micro-Raman spectra of (A) 70 mM precursor - 9 h, and (B) 50 mM precursor - 4 h samples. They demonstrate that $Cu_2(NO_3)(OH)_3$ appeared emerald, Cu_2O red, Cu_4O_3 and CuO black in visible light microscopy images. Visible light microscopy images and the corresponding micro-Raman spectra of (C) the self-assembled film seen in 70 mM precursor - 9 h sample, and (D) the spheres with corrugated surface seen in 70 mM precursor - 24 h sample. This confirms that the self-assembled films were Cu_2O and that the corrugated spheres were composed of Cu_4O_3 core and Cu_2O shell.

2.8(F)-left). As in Figure 2.8(E), the red spheres were confirmed to be Cu_2O. Micro-Raman spectra of the black spheres revealed Cu_4O_3 (Figure 2.8(F)-right). The phenomenon of black Cu_4O_3 spheres being much larger than red Cu_2O spheres in Figure 2.8(F) is universal across our samples.

Before the full consumption of $Cu_2(NO_3)(OH)_3$, the microstructure of Cu_2O and Cu_4O_3 attached to $Cu_2(NO_3)(OH)_3$ plates did not change much as the 70 mM precursor reactions progressed. Over time, $Cu_2(NO_3)(OH)_3$ plates shrunk and the oxide spheres grew larger. Cu_4O_3 spheres remained larger in size than Cu_2O. The self-assembled films composed of spheres (seen after 7 h reaction) were red in VLM and were found to be Cu_2O from micro-Raman spectroscopy (Figure 2.9(C)). After the depletion of $Cu_2(NO_3)(OH)_3$, days of reaction resulted in the surfaces of Cu_4O_3 spheres being covered by a layer of Cu_2O (Figure 2.9(D)), giving rise to their corrugated appearance seen by SEM (Figure 2.7(F)).

Reactions with 50 mM precursor displayed similar morphology development, but with all three binary copper oxides (Cu_4O_3, CuO, and Cu_2O) attaching to the $Cu_2(NO_3)(OH)_3$ surface (Figure 2.8(G,H)). At 2 h reaction time, black spherical particles were spotted on the emerald $Cu_2(NO_3)(OH)_3$ plate aggregates (Figure 2.8(G)-left). Their micro-Raman spectrum showed CuO (Figure 2.8(G)-right). At 3 h of reaction, the spheres attached to the surface were either black or red. Micro-Raman spectra showed that the black spheres are CuO and Cu_4O_3. The Raman spectrum of one Cu_4O_3 sphere is displayed in Figure 2.8(H)-right. The red spheres were identified to be universally Cu_2O (Figure 2.8(H)-right). By using micro-Raman spectroscopy to distinguish CuO and Cu_4O_3, we found that CuO and Cu_2O had comparable sphere sizes, while Cu_4O_3 spheres were mostly larger in diameter. Further reactions of 50 mM precursor series showed similar events as in the 70 mM case: formation of a self-assembled CuO film and the corrugation of Cu_4O_3 spheres by Cu_2O coverage.

The ability of all three binary copper oxides to nucleate on $Cu_2(NO_3)(OH)_3$ plate surfaces by adjusting reaction conditions is proven by our micro-Raman analysis. It was also observed that the size of Cu_4O_3 spheres was significantly larger than those of Cu_2O and CuO.

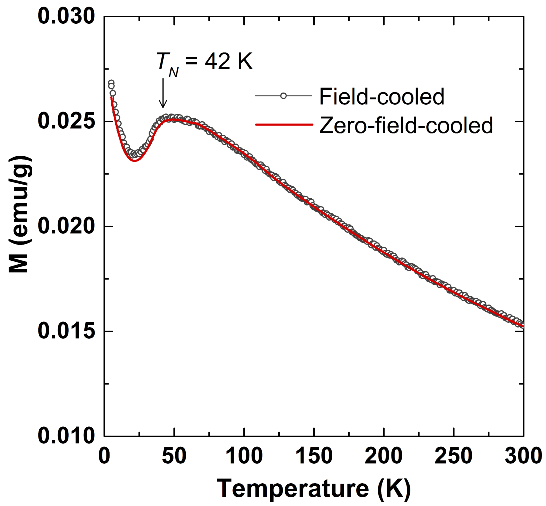

Figure 2.10: Magnetic susceptibility of Cu_4O_3 and diamagnetic Cu_2O obtained from a reaction with 70 mM precursor concentration and 48 h reaction time. Measured in field $H = 10^4$ Oe. The arrow corresponds to the reported Néel temperature $T_N = 42$ K reported for natural crystals, which coincides with our observed antiferromagnetic ordering for Cu_4O_3.

2.3.6 Antiferromagnetic Signature of Cu_4O_3

Controlled synthesis of bulk Cu_4O_3 is a mandatory goal before the magnetic properties of this system can be studied. We present the first verification that bulk synthetic paramelaconite displays the same Néel temperature as natural crystals, despite the limitation to micron-sized agglomerates currently imposed by the solvothermal synthesis route. Figure 2.10 shows the magnetic susceptibility of a sample generated from a 70 mM $Cu(NO_3)_2{\cdot}3H_2O$ precursor solution reacted for 48 h, which consists of Cu_4O_3 and diamagnetic Cu_2O. The drop in susceptibility at 42 K agrees with the value reported for natural crystals. [71] We expect this transition to sharpen as crystallinity and yield improve.

2.3.7 Progression of Cu Valence

Tracking the total copper valence in these reactions provides insight on how the reaction can be further optimized. We have seen that $Cu(NO_3)_2{\cdot}3H_2O$, when dissolved in ethanol alone, precipitates as $Cu_2(NO_3)(OH)_3$ at elevated temperatures (equation 2.1). The copper nitrate precursor concentration had little impact on this behavior (50 or 70 mM).

$$8\,Cu(NO_3)_2 \cdot 3\,H_2O \longrightarrow 4Cu_2(NO_3)(OH)_3 + 12\,NO_2(g) + 3\,O_2(g) + 18\,H_2O \tag{2.1}$$

Including DMF in the solvent has two effects. First, it encourages precipitation of dissolved copper ions into binary copper oxides. Second, the presence of DMF leads to reduction of Cu^{2+}. Chang *et al.* demonstrated the first effect by showing that reaction with DMF can convert $Cu(NO_3)_2 \cdot 3H_2O$ directly into CuO, without the involvement of $Cu_2(NO_3)(OH)_3$. [93]. The second effect is most apparent from our results. With the inclusion of 33 vol% DMF in the solvent, Cu^+ became the dominant ion after 5 h (Figure 2.2(C,D)) and Cu^+-containing Cu_4O_3 and Cu_2O formed (Figure 2.5(B,C)). Therefore, a reducing agent must be present in the solution. This can either be DMF itself, or a chemical species generated by the reaction of DMF and ethanol.

Chang *et al.* proposed that the hydration of DMF at similar reaction temperatures produced dimethylamine and formic acid (equation 2.2). [93] Dimethylamine was proposed to be responsible for precipitating solvated Cu^{2+} as CuO (equation 2.3), whereas formic acid is credited to be the reducing agent (equation 2.4). [83, 93, 94] Within the sensitivity limit our NMR and FTIR, we were unable to detect the presence of any liquid species other than the starting solvent in this study. Use of gas chromatography mass spectroscopy for the detection of trace chemicals generated in these reactions are to be discussed in Chapter 4, which implies that the reaction is more complicated than that shown in equation 2.2. Nevertheless, the importance of DMF in binary oxide formation and Cu valence reduction in this system is apparent.

$$HCON(CH_3)_2 + H_2O \longrightarrow HCOOH + NH(CH_3)_2 \tag{2.2}$$

$$Cu^{2+} + H_2O + 2\,NH(CH_3)_2 \longrightarrow CuO(s) + 2\,NH_2(CH_3)_2{}^+ \tag{2.3}$$

$$2\,Cu^{2+} + HCOOH \longrightarrow 2\,Cu^+ + CO_2(g) + 2\,H^+ \tag{2.4}$$

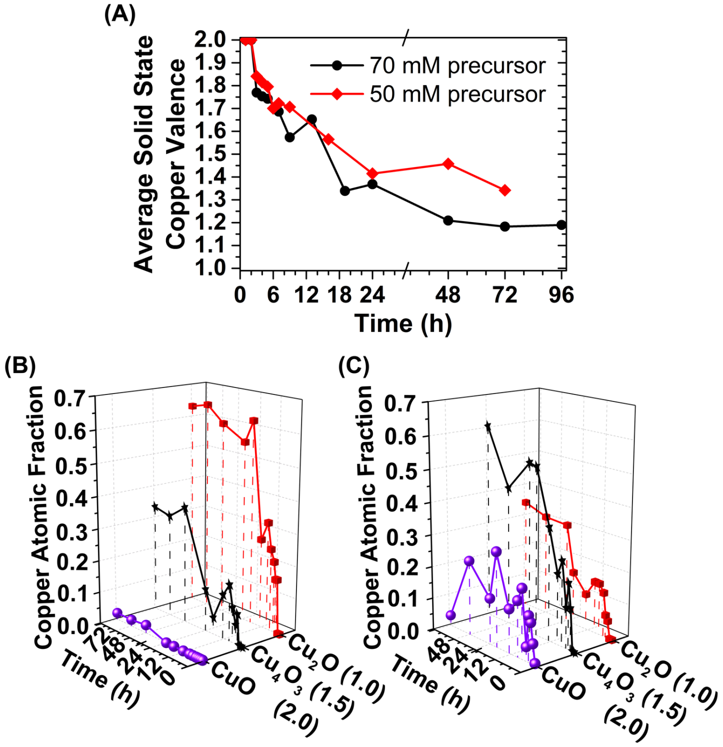

Figure 2.11: Panel (A) shows the change in overall Cu valence in the solid precipitates with time for 70 mM and 50 mM precursor reactions. The distribution of copper atoms between phases with average valence of 1 (Cu_2O), 1.5 (Cu_4O_3) and 2 (CuO) are shown for (B) 70 mM and (C) 50 mM precursor conditions. The overall Cu valence in the solid decreases even after the liquid has stabilized. The 50 mM reactions generated products with a more symmetrical distribution of Cu about Cu_4O_3.

If the reducing power of the system determines the final balance of copper oxides, then Cu_4O_3 would require an intermediate power between that of CuO and Cu_2O. The average Cu valance in all four solid phases during reactions are displayed in Figure 2.11(A). It is evident the that copper valence was continuously reduced with reaction time. The reducing agents in solution must remain active for at least 24 h. Figure 2.11(A) also demonstrates that the reducing power was weaker with 50 mM $Cu(NO_3)_2{\cdot}3H_2O$ precursor than with 70 mM. Further decrease of the $Cu(NO_3)_2{\cdot}3H_2O$ precursor concentration to 30 mM resulted in inefficient reducing power, creating a larger amount of CuO.

Although the difference in average Cu valence may seem small in Figure 2.11(A), the effect is magnified in the distribution of oxide phases (Figure 2.11(B,C)). For 50 mM precursor reactions, the oxide Cu valence is centered around 1.5+, which seems ideal given our target of Cu_4O_3, but the distribution is wide, limiting the purity of Cu_4O_3.

2.3.8 Proposed Reaction Mechanism

Based on our extensive characterization and earlier published studies of related systems, we propose a reaction scheme leading to the production of various copper-containing crystalline phases in Figure 2.12.

Ethanol-triggered and DMF-triggered precipitation pathways compete in the initial reaction steps. Previous studies, as well as ours, have confirmed the transformation of $Cu(NO_3)_2{\cdot}3H_2O$ to $Cu_2(NO_3)(OH)_3$ in ethanol alone, [83] and have shown that DMF alone will convert $Cu(NO_3)_2{\cdot}3H_2O$ to CuO and Cu_2O spheres. [93, 94] In our solvent with 67 vol% ethanol and 33 vol% DMF, both pathways took place simultaneously (Figure 2.12(A)): the precipitation of solvated Cu ions gave $Cu_2(NO_3)(OH)_3$, CuO, or Cu_2O.

$Cu_2(NO_3)(OH)_3$ clearly enables binary oxide growth by serving as a secondary copper source (Figure 2.12(B)). This was most apparent after the depletion of solvated Cu ions in the solution. As shown in Figure 2.2(C,D), few solvated copper ions persist in the solution after 5 h. However, the growth of binary oxides continues after 5 h (Figure 2.5(B,C)). This has to be compensated for by consuming $Cu_2(NO_3)(OH)_3$, the only phase decreasing in quantity at this stage. The conversion of $Cu_2(NO_3)(OH)_3$ into binary oxides is due to the instability of $Cu_2(NO_3)(OH)_3$ in DMF/ethanol, with final oxides dependent on the system reduction potential. Higher reducing power from our 70 mM precursor resulted in only Cu_2O alongside Cu_4O_3. Milder reduction power from our 50 mM precursor led to co-existence of CuO, Cu_2O, and Cu_4O_3.

The question is whether the three binary oxides formed from $Cu_2(NO_3)(OH)_3$ arise from dissolution-precipitation or on-site transformation. It has been shown that $Cu_2(NO_3)(OH)_3$ is not required for CuO and Cu_2O formation with 100% DMF solvent. [93] During the period when $Cu_2(NO_3)(OH)_3$ was the source for further Cu_2O growth, we noticed the formation

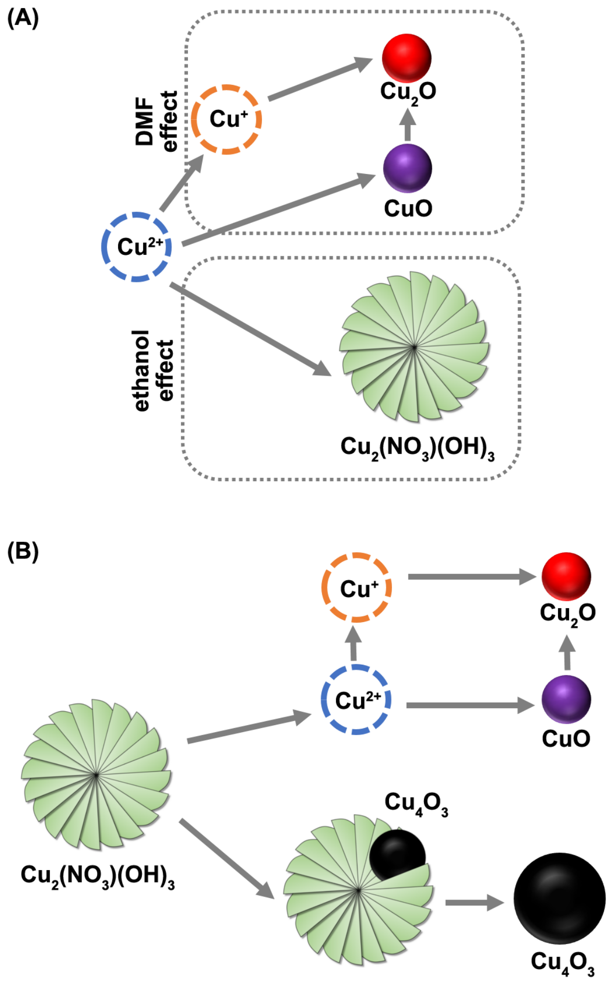

Figure 2.12: Schematic illustration of the proposed reaction mechanism. In (A), solvated copper nitrate precipitates as $Cu_2(NO_3)(OH)_3$ in ethanol, or CuO and Cu_2O in DMF. In (B), $Cu_2(NO_3)(OH)_3$ ca be converted to CuO and Cu_2O via dissolution-reprecipitation, or transformed into Cu_4O_3 via on-site reduction. The requirements for Cu_4O_3 crystal growth include ethanol-triggered formation of $Cu_2(NO_3)(OH)_3$ and its subsequent reduction. Cu_4O_3 yield is reduced by the presence of these competing dissolution reactions.

of self-assembled Cu_2O films far away from the $Cu_2(NO_3)(OH)_3$ plates after 7 h (Figure 2.7(D)). This physical separation implies that crystallization of CuO and Cu_2O can occur via precipitation of solvated copper ions, either initially dissolved (Figure 2.12(A)), or from the re-dissolution of $Cu_2(NO_3)(OH)_3$ (Figure 2.12(B)).

Cu_4O_3, on the other hand, likely formed by on-site reductive transformation of $Cu_2(NO_3)(OH)_3$ plates (Figure 2.12(B)). We observed large Cu_4O_3 spheres embedded in $Cu_2(NO_3)(OH)_3$ plates (Figure 2.7(C)), while the small Cu_2O and CuO spheres appeared only resting on top of the $Cu_2(NO_3)(OH)_3$ plates. There have been no reports of Cu_4O_3 synthesis in a DMF-only solvent. A possible explanation for the formation of embedded Cu_4O_3 spheres is that, without re-dissolution, conversion of $Cu_2(NO_3)(OH)_3$ into Cu_4O_3 was more favorable than into CuO or Cu_2O. This implies that $Cu_2(NO_3)(OH)_3$ is a necessary predecessor for Cu_4O_3 formation in our reaction system. This is further supported by the observation that the amount of Cu_4O_3 and $Cu_2(NO_3)(OH)_3$ stabilized at the same time.

Based on our proposed reaction scheme, three factors are critical for the growth of Cu_4O_3 crystals: the precipitation of $Cu_2(NO_3)(OH)_3$ from copper nitrate in the presence of ethanol, the on-site reductive transformation from $Cu_2(NO_3)(OH)_3$ to Cu_4O_3 triggered by DMF, and a suitable reduction potential in the reaction environment. Competing processes include the direct oxide formation from solvated Cu ions, and the re-dissolution of $Cu_2(NO_3)(OH)_3$. It would be desirable to suppress these competitive oxide formation pathways to improve Cu_4O_3 yield. With continued exploration of the reactions mechanisms described here, this solvothermal system has the potential for high-purity Cu_4O_3 production.

2.4 Conclusions

In this study, we conducted a time-resolved study on the solvothermal formation of the inorganic crystal Cu_4O_3 utilizing a reaction medium composed of ethanol and DMF. It was established that performing the reaction in fused silica tubes were better for this *ex situ* kinetic study. This reaction design allowed better reproducibility of reaction. It allowed easier quick examination on the state of the system. It is also more efficient in quenching so that the result is more trustworthy. The quenched samples were subjected to extensive characterization in order to understand the reaction mechanism of Cu_4O_3 formation from a $Cu(NO_3)_2{\cdot}3H_2O$. Combining quantitative diffraction data with microscopic phase identification, the progression of the reactions was examined in detail. Copper oxide formation resulted from the mineralization effects of both ethanol and DMF. We found that CuO and Cu_2O precipitated from dissolved copper ions, while Cu_4O_3 was likely formed by on-site transformation of the $Cu_2(NO_3)(OH)_3$ predecessor. Key elements of stabilizing metastable Cu_4O_3 crystals were identified to be the generation of $Cu_2(NO_3)(OH)_3$ and a suitable reduction potential for transformation into Cu_4O_3. This work separated this one-pot solvothermal synthesis into two synchronized and synergistic steps, underlying how important thermodynamic and kinetic information concerning inorganic materials formation can be retrieved through detailed time-resolved *ex situ* studies.

CHAPTER 3

IN SITU EDXRD INVESTIGATION OF SOLVOTHERMAL Cu_4O_3 FORMATION

3.1 Introduction

Despite the success of unraveling part of the mystery of how Cu_4O_3 formed in Chapter 2, *ex situ* examination still has its drawbacks.

One problem with the *ex situ* investigation is related to the variability (and hence low reproducibility) of this solvothermal reaction. Therefore, although kinetic maps have been constructed, the accuracy is still questionable. The zig-zag pattern seen in Figure 2.6 is mainly attributed to sample-to-sample variations. Such a pattern should not exist in real *in situ* kinetic data. One unsettled question in Chapter 2 is related to the solvothermal stability of the three copper oxides Cu_2O, CuO, and Cu_4O_3. While it seems that the amount of these phases did not change drastically, it is still possible that the phases were still slowly evolving with time. The sensitivity of *ex situ* kinetics did not determine whether Cu_4O_3 is thermodynamically stabilized or kinetically stabilized in this solvothermal synthesis. The SEM image in Figure 2.7 cannot fully settle this debate. While the Cu_4O_3 surface was seen becoming rugged and covered with Cu_2O, both scenarios are possible. The Cu_2O covering the Cu_4O_3 surface could be formed due to Cu_4O_3 transforming into more stable phases, or through preferential coagulation of the Cu_2O spheres formed elsewhere. It will be helpful to identify the truly stable phase(s) in this reaction scheme if a deeper understanding of this particular system is desired.

Another concern on the *ex situ* data is how accurately the quenched samples represent the real system during reaction. There is no guarantee that the crystalline phases and molecular species did not suffer identity changes after quenching. This can be serious for the liquid sample, as small organic molecules are known to be very temperature sensitive. However, our major focus here was on the crystalline solid phases, whose impacts were more consequential. Through XRD of the *ex situ* sample, the presence of all three copper oxides Cu_2O, CuO, and Cu_4O_3 are shown. But there is a possibility that a particular phase formed during cooling and is not actually present during reaction. It is important to supplement with *in situ* data to increase the reliability of the kinetic map and reaction mechanism deduced from *ex situ* studies.

In situ diffraction studies of solvothermal reactions have been a challenging task. Although successful demonstrations of *in situ* hydrothermal / solvothermal XRD do exist, the designs were limited to specific types of reactions. Because of this, we have attempted to devise our own designs, including lab-source *in situ* solvothermal diffraction, and *in situ* neutron diffraction at POWGEN, where we had evaluated hypotheses about how to make *in situ* solvothermal investigations work. The most successful demonstration is with the use of energy-dispersive X-ray diffraction (EDXRD) performed at 6-BM-B at Advanced Photon Source (APS) in Argonne National Laboratory (ANL).

EDXRD is a variation of the conventional XRD technique. In conventional XRD, monochromatic X-rays are incident on the sample and the variation of the X-ray intensity with scattering angle is recorded. In EDXRD, a polychromatic beam of X-rays (which is possible with synchrotron source) is incident on the sample, the scattered X-ray intensities are analyzed with respect to the X-ray energy (and therefore wavelength) while keeping a fixed scattering angle. High synchrotron X-ray energy and intensity permit high beam penetration, making it more suitable for the study of solvothermal reactions which are in enclosed systems. *In situ* EDXRD has been performed in the past to study the solvothermal reaction systems. [95–97] Most of these previous *in situ* EDXRD studies relied on beam penetration through a thick autoclave (high noise), specialized furnaces, or chemically simple, single-step reactions. In our work, we contained our reagents in fused silica ampoules without steel autoclaves, which improves the signal-to-noise ratio. A full-size oven, instead of a specialty mini-oven, was used in this study so that we can fully mimic the reaction conditions verified in the lab at the beamline, eliminating unnecessary variable changes. Our oven is customized with two X-ray ports on the two lateral side. The ports are plugged with rubber stopper during lab-reactions, but can be replaced with metal foil windows for *in situ* EDXRD. These factors therefore allowed us to examine this complex and sensitive Cu_4O_3 formation chemistry.

3.2 Instrumentation and Characterization

The preparation of precursor solutions enclosed in fused silica tubes was similar to that described in Section 2.2. A 15 mL mixture of $Cu(NO_3)_2{\cdot}3H_2O$, ethanol, and DMF was made and sealed inside a 15 mm O.D. fused silica tubes. If without any specific mention, the precursor composition was composed of 50 mM $Cu(NO_3)_2{\cdot}3H_2O$, 20 vol% DMF, with balancing 80 vol% ethanol.

In situ energy-dispersive X-ray diffraction (EDXRD) was performed at beamline 6-BM-B in APS, ANL. The reaction was conducted with a Despatch LFC Class A bench-top oven (LFC 1-38). The oven has two circular port openings on the lateral sides of the furnace. The port openings are 2 inches in diameter, with their centers 10 inches above the oven base. The port holes were covered with aluminum foils both on the inside and outside of the oven for EDXRD measurement. The EDXRD setup has a preset detector position, which fixes the scattering angle at 6.50° and determines the location of the sample in focus. The oven had to be positioned very close to the detector because of this (Figure 3.1(A)). However, even with this arrangement, one lateral metal liner plate within the oven had to be taken off to get the sample in focus. The sample was held in place by a holder that approximately fix the sample location within the oven. With this holder, the sample tube was held almost vertical with an inclination angle of $\sim 10°$. A steel plate was placed in front of the sample to attenuate low energy X-ray intensity. This decreased localized heating due to absorption of the incident X-rays. Figure 3.1(B) shows photos of the sample placement.

The oven was programmed to heat the sample from room temperature to 130°C in 11 min. It was then held at 130°C for 11 h. In the end, it was programmed to cool to room temperature in 2 h.

For this EDXRD setup, the incident X-ray was slit down to a beam size of 100µm × 100µm during diffraction. Two perpendicular slits controlled the irradiation area. During imaging, the slits were kept fully open, which gave an irradiation area more than 100 times larger than that in diffraction. Canberra germanium solid state detector was used to detect the scattered X-ray with a front conical opening of 50 µm and a back conical opening of 70 µm. This detector has 10 strips within. The strips are aligned along a circle, with 9 strips (#1 - #9) equally spaced along a semicircle running from the uppermost to the lowermost positions. Strip #10 is at the middle of the other semicircle, opposite Strip #5. Right after the start of oven heating, the sample position was rastered in all three Cartesian directions to find space with good diffraction signals of precipitates. The physical positions where crystalline precipitates gather needed to be determined in this way. This had to be done because imaging contrast was too low to find where precipitates were most abundant. After spotting where precipitates gathered, the sample position was fixed except in the vertical direction. In general practice, a series of diffraction patterns were taken with gauge volume moving from the bottom to the top, after which an image was captured with the gauge volume brought back to the bottom. The series was repeated (with some manual adjustments on the range of movement) until the end of the reaction.

The software PLOT85 (written by Kenneth Baldwin) [98] was used to convert the energy-dispersive diffraction data into *d*-spacing intensity data. Each individual diffraction was converted to 10 files, each for 1 detector strip. A self-developed Matlab script was used to sum these ten files into a single one, and transform *d*-spacings into the corresponding 2θ values expected from a monochromatic diffractometer with Mo $K_{\alpha 1}$ radiation (λ=0.7093Å)

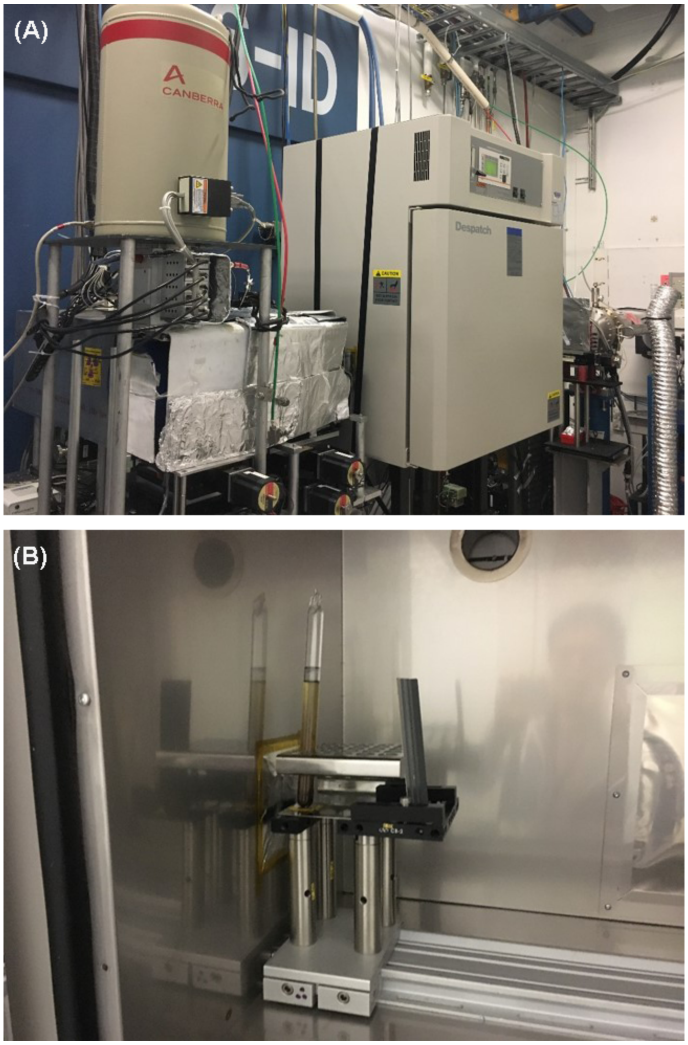

Figure 3.1: Photos showing the instrumentation used in the *in situ* EDXRD measurement. (A) A full-sized reaction oven with X-ray ports were positioned very close to the energy-dispersive X-ray detector. (B) The solvothermal sample tube was placed close the oven wall, with a steel plate to attenuate the intensity of incident low-energy X-rays. The fused silica sample tube shown had a diameter of 15 mm.

(which is the X-ray wavelength of our D8 lab diffractometer). The transformed data were further analyzed by GSAS-II and Topas 5, whose details will be discussed later.

The reaction tubes after *in situ* EDXRD measurement were later opened and analyzed *ex situ*. Laboratory powder XRD was performed on the dried precipitates using Bruker D8 ADVANCE diffractometer equipped with a Mo-K_α source and LYNXEYE XE detector in transmission geometry. Rietveld refinements of the lab-XRD data were performed using Bruker TOPAS 5.

3.3 Data Analysis and Results

Lab XRD of the final crystalline phases after *in situ* EDXRD reaction at 6-BM-B at APS is shown in Figure 3.2. Phase matching revealed that all three copper oxides Cu_2O, CuO, and Cu_4O_3 were present after reaction, which is to be expected based on *ex situ* studies discussed in Chapter 2. Rietveld refinement was used to quantify the mass fractions of the phases (Figure 3.2), which were used as standard values for semi-quantitative EDXRD calibration to be discussed later. The refinement indicated that Cu_4O_3 was the primary crystalline phase, followed by Cu_2O, with CuO present but very scarce. There were no unexpected phases, and the result is comparable to that obtained from a normal solvothermal reaction with this condition. These imply that subjecting the system to continuous high energy polychromatic X-ray irradiation during solvothermal reaction did not cause changes to reaction chemistries that drastically affected crystallization outcomes.

The EDXRD instrumentation at 6-BM-B was designed with very small gauge volume. Gauge volume is the size of the material interrogated by diffraction, and is determined by the slit opening size and scattering angle. This setup at 6-BM-B is mainly used for measuring strain distribution of geological samples under stress, so the gauge volume was chosen to optimize intensity with resolution. If we used too large a gauge volume, the noise would be very high. This small gauge volume caused trouble in our *in situ* EDXRD measure-

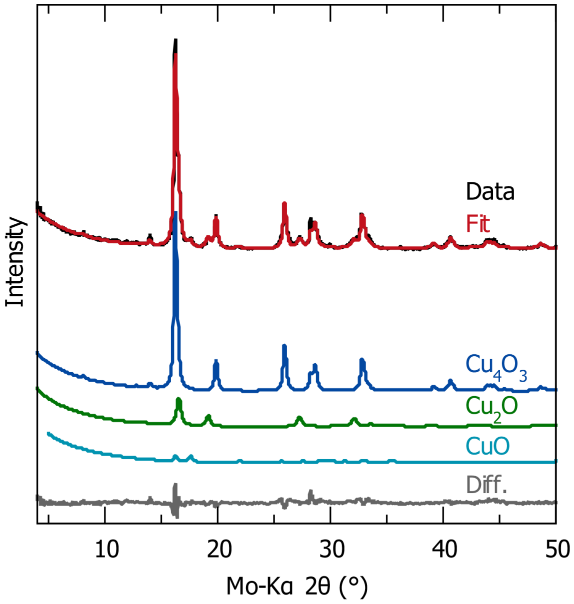

Figure 3.2: *Ex situ* lab XRD pattern of the sample after the end *in situ* EDXRD reaction and its Rietveld refinement result.

ment. The first problem is that this volume was very small compared to the sample volume. Since we could not pre-locate where the crystallites would gather, we had to raster sample position during reaction to find the optimum spot of measurement. This was found to be extremely difficult at the start of the reaction when precipitates were scarce. Typically, we were unable to record useful Bragg signals until after 1 h into the reaction. The second problem is that small gauge volumes can suffer from strong texture effects from large crystals. Good powder diffraction requires sufficient randomly-oriented crystallites within the gauge volume for statistically significant peak intensity. When there are only few highly textured crystallites, they may produce a few extremely high intensity peaks. I suspect this was the case for $Cu_2(NO_3)(OH)_3$ in our reaction. $Cu_2(NO_3)(OH)_3$ is an intermediate phase existed only in the early stage, which was already hard to capture due to the first problem discussed. Moreover, it was expected to have a large crystal size (up to 10 μm in the long direction) with a plate morphology. Therefore, $Cu_2(NO_3)(OH)_3$ in the gauge volume might create a few abnormal peaks, which was indeed what we saw at the early stage ($\sim$1h). The monoclinic crystal structure and large lattice parameters of $Cu_2(NO_3)(OH)_3$

imply that diffraction-allowed *d*-spacings are virtually any value. Because of this, the presence of $Cu_2(NO_3)(OH)_3$ cannot be assured from the observation of a few abnormal peaks. These peaks could not be differentiated with transient noise spikes which were found to be common for this experiment. Taking these problems into consideration, the first two hours of reaction where $Cu_2(NO_3)(OH)_3$ might exist were not refined.

Despite these problems, some concerns about the *ex situ* caveats were addressed with *in situ* EDXRD study. The peaks seen in the EDXRD patterns (>2h) can be compared with the *d*-spacings of the copper oxide phases. For the majority of them, it is certain that all three forms of copper oxides Cu_2O, CuO, and Cu_4O_3 co-existed at the reaction temperature. We also did not observe drastic changes in the *in situ* EDXRD diffraction patterns during cooling. It is thus confirmed that quenching has no drastic effect on the crystalline phases. This gives creditability to the *ex situ* kinetic maps (Figure 2.6).

The question concerning solvothermal stabilities of the three copper oxide phases required kinetic analysis with quantitative refinement. Quantitative analysis of EDXRD patterns is not as straightforward as for conventional XRD. One drawback of EDXRD is related to the polychromatic nature of the incident X-ray. In conventional XRD, wavelength (λ) is fixed and the scattered X-ray intensities with scattering angle (2θ) are recorded. Since a monochromatic X-ray is used, there is no change in source intensity and scattered intensity differences are entirely diffraction-related. In EDXRD, the polychromatic incident X-ray does not have constant intensity with respect to wavelength. The X-ray intensity peaks around the energy corresponding to $\sim$2.5 Å *d*-spacing. The intensity falls as the X-ray deviates from this energy. Because of the variation of X-ray intensity with energy, the detected X-ray intensity differences are a combined effect of diffraction and the incident X-ray profile. Therefore, direct quantitative Rietveld refinement of the EDXRD data is not possible. Energy-dependent absorbance of the X-rays by objects in the beam-path also makes the X-ray intensity profile instrumentation-dependent. We did not achieve a reliable deduction for such profile. Therefore, the EDXRD data is best treated for qualitative analysis based on peak position matching instead of quantitative phase analysis.

Nevertheless, I have formulated a method to process the *in situ* EDXRD data in a semi-quantitative manner. This method gives an estimate for the mass fraction of the constituent phases in the EDXRD pattern without correcting variations in incident beam intensity, but the results are not as trustworthy as a direct quantitative Rietveld analysis. In this approach, the EDXRD pattern of the sample at the end of the reaction was compared with that of the conventional lab XRD data taken *ex situ* (Figure 3.2). It was assumed that the sample homogeneity was good enough to equate the two. The EDXRD pattern was first fit to the phase mixture of Cu_2O, CuO, and Cu_4O_3. However, no detailed crystal structures for the phases were specified except for the space group and lattice parameters (determined by *ex situ* XRD). Intensities of the three phases with space group-allowed peaks were freely refined to give the best match to the EDXRD pattern. It thus constrained peak positions but gave full freedom on peak intensity. This fitting scheme is termed "hkl fit" in Topas implementation and has two algorithms called "Pawley method" and "Le Bail method". The Pawley method was used in this example. In a normal quantitative Rietveld refinement, three factors determine the relative phase amount: scale factor, cell mass, and cell volume. For this Pawley fitting, the cell volume was fixed by the *ex situ* determined lattice parameters. Both scale factor and peak intensity parameters control the integrated intensity of calculated peaks. The peak intensity parameters took the role of structure factors in Rietveld refinement, and after an initial satisfied fitting they were all fixed. However, since these peak intensity parameters were not related to crystal structures and thus can be arbitrarily scaled, the scale factors in these cases affected the appearance of calculated curves, but did not have an absolute scale. The cell masses, on the other hand, had no effect of the appearance of the calculated curve, but were involved in phase fraction calculation. Therefore, the concept of virtual cell mass was introduced. These virtual cell masses for different phases set the scales for scale factors (and had no relation to real cell mass) so that calculation of phase fraction using the original formula could still work. In practice,

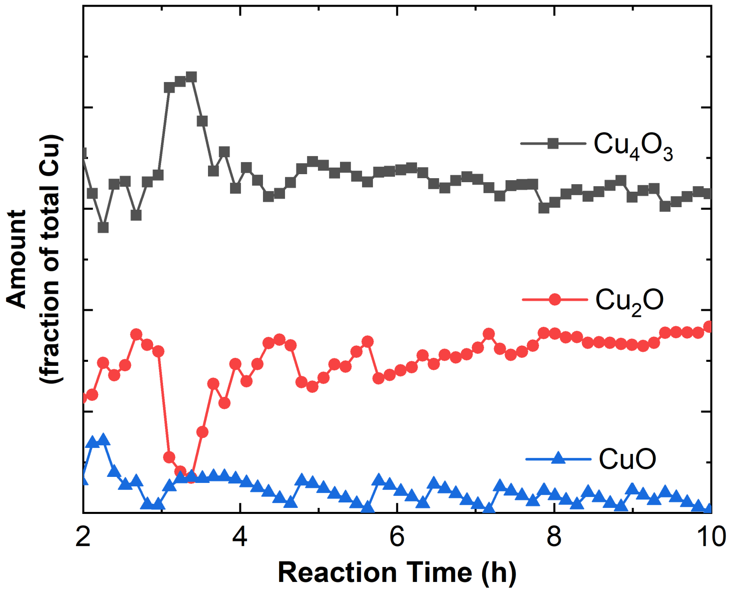

Figure 3.3: Evolution of the amount of Cu_4O_3, Cu_2O, and CuO determined by semi-quantitative analysis of the *in situ* EDXRD patterns.

the cell mass for one phase was fixed, while the cell masses for the other two phases were adjusted until they resulted in the same phase fractions as for the *ex situ* result. Afterwards, the cell masses were all fixed, and these phase states were saved as bases for future Pawley refinement of other EDXRD patterns where only scale factors were refined. This procedure is a modification of the PONKCS (Partial Or No Known Crystal Structures) method of refinement. The scale factors thus derived provided semi-quantitative phase fractions for *in situ* EDXRD data.

This semi-quantitative Pawley fit was performed for all *in situ* EDXRD patterns. The results were converted to normalized amounts of each phase, quantified by the amount of Cu element in one phase relative to the total amount of Cu in all copper oxide phases. Figure 3.3 shows the time evolution kinetics for Cu_2O, CuO, and Cu_4O_3 within the gauge volume at one particular position close to the bottom of the tube.

One intriguing observation is that there were sudden jumps in the amount of all phases that occurred at irregular time intervals. One probable postulation is related to the disturbance from absorbing polychromatic X-ray beams. When a sample tube with crystalline powder within was placed in the beam with slits fully open, we have observed the formation of gas bubbles from the imaging camera. These bubbles disturbed the powder settled at the bottom of the tube and redistributed it in space. This happened even when the oven is at room temperature, so it was not an intrinsic phenomenon of the solvothermal process. It was likely related to the absorption of low energy X-rays by the liquid phase that created localized heating or side-reactions. During *in situ* EDXRD measurement, the slits were fully opened during imaging. It is possible that occasionally during imaging, absorption of polychromatic synchrotron caused gas bubble formation that disturbed the powder. Since the gauge volume was very small, local statistics seen were changed, resulting in the jumps. The jump frequency was much lower than the imaging frequency though, meaning not all imaging actions caused bubbling. Because of these powder redistribution events, local phase kinetics seen in Figure 3.3 were separated into segments, and it became trivial to compare between different segments.

Even only within the single segments, it is still interesting to look at the phase kinetics. Figure 3.3 showed some small changes to the phase within each segment, but since such change is small and Figure 3.3 was constructed based on semi-quantitative whole pattern fitting, it makes more sense to only look at single peaks within each segment. Figure 3.4 shows the change of the characteristic peaks for Cu_2O, CuO, and Cu_4O_3 within a single segment. These are selected peaks of the corresponding phases that do not overlap. Therefore their heights are direct indications on the amount the phases. From Figure 3.4, it looks like the amount of CuO was continuously decreasing, the amount of Cu_2O was continuously increasing, while the amount of Cu_4O_3 remained relatively unchanged. Therefore it can be expected that CuO was transforming into Cu_2O under this solvothermal condition. Cu_4O_3 crystallites, on the other hand, did not fade away once formed, nor did it receive any addition from transformations of CuO and Cu_2O crystals. Partial conversion of Cu_2O back to CuO is suggested during the bubbling event by Figure 3.3. These bubbling events were the result of absorbing polychromatic synchrotron radiation, and are not expected in normal

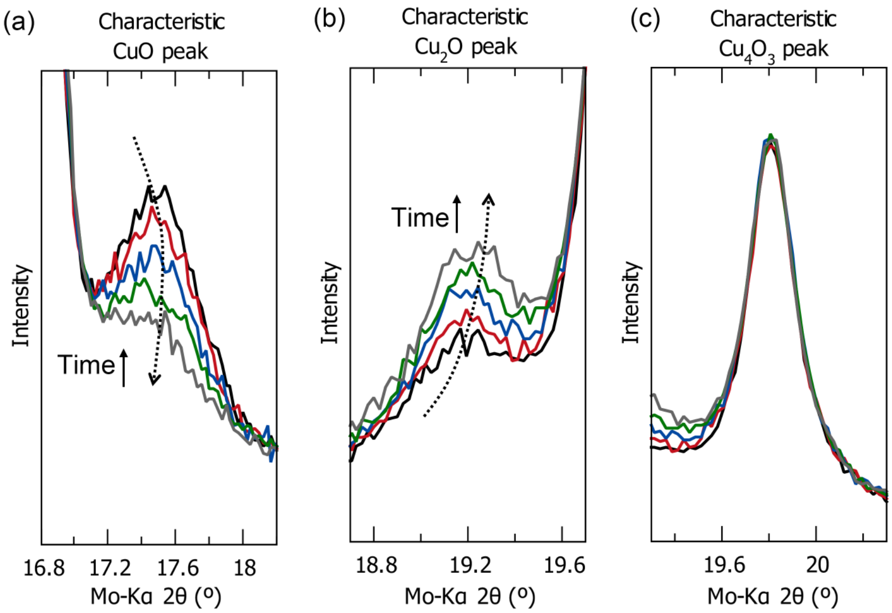

Figure 3.4: Evolution of the intensity of peaks for (a) the characteristic CuO peak at 17.4°, (b) the characteristic Cu_2O peak at 19.2°, and (C) the characteristic Cu_4O_3 peak at 19.8°. The peaks shown are within a single segment without the occurrence of jumps initiated by gas bubbles.

solvothermal reactions. These results suggest that transformations between CuO and Cu_2O is possible. Their balances depend on the specific chemical potentials determined by the reaction condition. Cu_4O_3, on the other hand, does not have significant phase change once formed, and can be regarded as a “stable phase”. Its resistance to change implies that in this specific solvothermal environment, it is either thermodynamically stable but kinetically hard to access from the states of CuO or Cu_2O, or extremely stabilized by kinetic reasons. This *in situ* EDXRD study shows that there are significant kinetic barriers for Cu_4O_3 to transform to Cu_2O or CuO, but a low transformation barrier between CuO and Cu_2O. This finding is consistent and support the postulated reaction mechanism (Figure 2.12) from *ex situ* study.

3.4 Conclusions

Using synchrotron-based EDXRD, *in situ* kinetics on the solvothermal formation of Cu_4O_3 in the environment of DMF and ethanol were tested. Although we did not obtain strictly continuous quantitative phase information on the solvothermal products without unwanted interruption, this study did answer some questions concerning the credibility of *ex situ* results performed on quenched samples. All three forms of copper oxides Cu_2O, CuO, and Cu_4O_3 were seen at the solvothermal temperature from *in situ* EDXRD measurement. The kinetic stabilities of the three phases Cu_2O, CuO, and Cu_4O_3 can be inferred from examining their EDXRD signal changes within a single segment uninterrupted by gas-bubbles. The *in situ* results show that Cu_4O_3 was kinetically more stable, while transformations between CuO and Cu_2O took place. Such behaviors were expected if Cu_4O_3 was formed through a different mechanism than CuO and Cu_2O, which is the main feature of the reaction mechanism (Figure 2.12) proposed.

This was the first attempt in our research group to conduct *in situ* EDXRD, and our first successful *in situ* XRD study on solvothermal reactions. Therefore, there were several shortcomings in the design that can be improved upon in the future. Some major problems are shown below. The first problem is the small gauge volume. While this gave us a good spatial resolution, such pros did not justify the accompanying cons. The small gauge volume made it very hard to locate the physical space for monitoring the reaction *in situ*. Thus, the most valuable kinetic information in the early reaction stage was lost. The small gauge volume also caused signals contributed from large $Cu_2(NO_3)(OH)_3$ plates to be uninterpretable. In the future, it would be preferable to look for EDXRD stages that allow for a large gauge volume. This would require the use of an energy-dispersive X-ray detector with a large conical opening. The second problem concerns the polychromatic nature of the incident X-ray. This caused difficulty in quantitative phase refinement and disturbed the original solvothermal reaction. The semi-quantitative method I implemented using Pawley method is not as accurate as the quantitative Rietveld method. In the future, it would be desirable to first spend enough effort to log the dependence of X-ray intensity on X-ray energy in a condition that mimics our *in situ* solvothermal reaction setup. The low energy portion of the polychromatic X-ray also induced X-ray absorption by the liquid within the solvothermal system. Luckily no significant changes to the overall solvothermal chemistry were observed. But it resulted in bubble formation that caused discontinuities in our *in situ* kinetic data. To minimize X-ray absorption, this would require the selection of a beamline whose bending magnet provides higher energy white beam, or the use of filters to selectively remove the low energy X-rays. Higher X-ray energy will cause a smaller scattering angle, so it will also demand a different detector location to be implemented. The third problem is that the sample was located too close to the edge of the oven in order to have the sample in focus. The oven is not designed to have sample at such location and therefore heating efficiency and uniformity is not guaranteed. This will be solved if the detector is positioned at a smaller scattering angle. The fourth problem is that the sample holder was not very well designed. In the future, we can design and build a dedicated sample holder that fixes the sample tightly so that good sampling volume can be defined before reaction.

CHAPTER 4

RELATIONS BETWEEN SOLVENT CHEMISTRY AND SOLVOTHERMAL FORMATION OF COPPER COMPOUNDS

4.1 Introduction

Although we have successfully made Cu_4O_3 using the solvothermal approach that used $Cu(NO_3)_2{\cdot}3H_2O$, ethanol, and DMF, as discussed Chapters 2 and 3, these Cu_4O_3 particles still come with impurities in the form of Cu_2O and CuO. We have yet to refine the process so that phase-pure Cu_4O_3 can be consistently synthesized. As an effort to improve the formulation of this solvothermal synthesis scheme, we made modifications to the solvothermal chemistry.

The work on testing the solvothermal chemistry was investigated in two sets of reactions. In the first set, we devised alternative reaction schemes based on the mechanism (Figure 2.12) proposed in Chapter 2. There, it was postulated that CuO and Cu_2O mainly came from homogeneous precipitation in solution, whereas Cu_4O_3 formation was a result of on-site reduction on $Cu_2(NO_3)(OH)_3$. Since $Cu_2(NO_3)(OH)_3$ was postulated as the direct predecessor to Cu_4O_3, it is imperative to ask whether it is possible to synthesize Cu_4O_3 directly using $Cu_2(NO_3)(OH)_3$ as the precursor instead of $Cu(NO_3)_2$. Following this philosophy, we reacted $Cu_2(NO_3)(OH)_3$ solvothermally in different liquid mediums based on DMF and ethanol, and looked for diffraction evidence of the formation of Cu_4O_3.

In the second set, we tried to change the liquid chemistry completely by substituting DMF with other chemicals. In this approach, we explored vastly different regions of chemical potential landscape and saw evidence of the existence of different forms of copper-containing inorganic materials. It shows that Cu_4O_3 is indeed a very sensitive material whose stability is only possible in a very specific solvothermal environment.

4.2 Synthesis and Characterization

$Cu_2(NO_3)(OH)_3$ precursor was synthesized with two methods. The first method involved reacting 100 mM $Cu(NO_3)_2{\cdot}3H_2O$ in 33 vol% DMF and 67 vol% ethanol at 130°C for 2h using the autoclave reactor. The second method mixed 150 mM $Cu(NO_3)_2{\cdot}3H_2O$ aqueous solution with an equal volume amount of 100 mM NaOH aqueous solution at room temperature, followed by magnetic stirring for a few minutes. The precipitates were separated by centrifuge and dried. Both methods produced phase-pure $Cu_2(NO_3)(OH)_3$ as verified by XRD.

A special solution called “solvothermal remnant liquid” was specially prepared. This was done through the reaction of 50 mM $Cu(NO_3)_2{\cdot}3H_2O$ in 33 vol% DMF and 67 vol% ethanol at 130°C for 24h using the fused silica reactor. The product after this reaction was centrifuged to isolate the liquid phase, which was this “solvothermal remnant liquid”.

Solvothermal reactions in sealed fused silica tubes were used for the first set of reactions. In this approach, 8.5 mL liquid solution or dispersion was prepared and poured into a fused silica tube with 12 mm O.D. and 10 mm I.D. The end of the tube was submerged into liquid nitrogen to freeze the solution. The tube was then evacuated and sealed. Solvothermal reactions were conducted by placing the sealed tube vertically inside a Quincy Lab QL-40 oven pre-heated to the desired temperature for a specific duration. A thermocouple was used to monitor and control the temperature within the oven. After reaction, the tubes were taken out of the oven and air-cooled. After cooling to room temperature, the fused silica tube was opened and the products were collected and centrifuged to separate the liquid and solid phases.

For the first set of reactions, $Cu_2(NO_3)(OH)_3$ precursor was added to 8.5 mL of the prepared liquid to make a dispersion. The amount of $Cu_2(NO_3)(OH)_3$ was chosen so that the total Cu element in the dispersion was the same as a 50 mM $Cu(NO_3)_2$ solution. The liquid medium used include (i) pure DMF, (ii) 40 vol% DMF and 60 vol% ethanol, (iii) 40 vol% DMF, 60 vol% ethanol, and 23 µL H_2O, (iv), 25 mM CuCl in 40 vol% DMF, 60 vol% ethanol, (v) 75 mM $Na(NO_3)$ in 40 vol% DMF, 60 vol% ethanol, and (vi) the "solvothermal remnant liquid". The solvothermal reaction condition was at 130°C for 24 h unless otherwise specified.

Solvothermal reactions in autoclaves were used for the second set of reactions. $Cu(NO_3)_2 \cdot 3H_2O$ was dissolved in a liquid mixture of ethanol and another solvent to make 50 mM solution. The solvents tested include acetonitrile, ascorbic acid, citric acid, oxalic acid, dimethylacetamide, 2-pyrrolidone, and ethylenediamine. The volume percent of the chemical was typically 33 vol%, but other amounts were also used and specified in the relevant context. For those chemicals which are solid at room temperature, their mass was measured and converted to the corresponding volumes using density values. In this approach, 15 mL of the precursor solution was placed in a 23 mL capacity Teflon-lined autoclave (Parr Instruments). The oven usage and product handling is the same as the fused silica tube approach. Typical solvothermal reactions were conducted at 130 °C for 24 h unless otherwise specified.

Powder X-ray diffraction (XRD) patterns of the solid samples were collected on a Bruker D8 ADVANCE diffractometer equipped with a Mo-K_α source and LYNXEYE XE detector in transmission geometry. Rietveld refinements were performed using Bruker TOPAS 5. Scanning electron microscopy (SEM) images the samples were taken with a JEOL JSM-6060LV microscope with 15 kV acceleration voltage. Thermogravimetic analysis (TGA) of the solid sample was conducted on TA Instruments Q50 with nitrogen flow over the sample. The heating rate was 10 °C/min. Gas chromatography mass spectroscopy (GC-MS) was acquired using a GC-MS system (Agilent Inc) consisting of an Agilent 6890 gas chromatograph, an Agilent 5973 MSD and a HP 7683B autosampler. Gas chromatography was performed on a ZB-1MS (30m × 0.32 mm I.D. and 0.25 µm film thickness) capillary column (Phenomenex). The inlet temperature was 280 °C, the MS interface temperature was 25 0°C, and the ion source temperature was adjusted to 230 °C. An aliquot of 1 µL was injected in split mode (15:1). The helium carrier gas was kept at a constant flow rate of 1.6 mL/min. The temperature program as 2 min at 50 °C, followed by a temperature ramp of 10 °C/min to 200 °C for 2 min. The mass spectrometer was operated in positive electron impact mode at 69.9 eV ionization energy at m/z 33-300 scan range. The threshold was 100. The instrument variability was within the standard acceptance limit (5%). The spectra of all chromatogram peaks were evaluated using the AMDIS v2.71 software (NIST) and NIST Mass Spectral Database (NIST08) (John Wiley & Sons, Inc.).

4.3 Results and Discussion

4.3.1 Solvothermal Conversion of $Cu_2(NO_3)(OH)_3$

Since $Cu_2(NO_3)(OH)_3$ was the direct predecessor to Cu_4O_3, we tried to solvothermally react $Cu_2(NO_3)(OH)_3$ dispersed in a liquid medium. We first tried pure DMF and a mixture of ethanol and DMF (33 vol%) as the liquid medium as ethanol–DMF is the solvent system used in Chapter 2 and DMF was thought to be the agent responsible for the reduction of $Cu_2(NO_3)(OH)_3$. However, only Cu_2O and CuO could be found, as evident in the XRD plot showing the product using DMF and ethanol as a liquid medium (Figure 4.1). This shows that the liquid medium was not exactly the same as that for the synthesis used in Chapter 2, although both have ethanol and DMF as the dominant components with the same ratio. In the original synthesis, $Cu(NO_3)_2{\cdot}3H_2O$ was used as the copper precursor. Thus, changing the precursor from $Cu(NO_3)_2{\cdot}3H_2O$ to $Cu_2(NO_3)(OH)_3$ actually modified the reaction chemistry. Some critical ingredients must have been missing.

We tried to figure out those missing ingredients by adding extra chemicals into the liquid medium of 33 vol% DMF and 67 vol% ethanol. In the original synthesis, $Cu(NO_3)_2{\cdot}3H_2O$ was dissolved, but we could not simply add $Cu(NO_3)_2{\cdot}3H_2O$ because this would cause the same solvothermal reaction to happen that formed Cu_2O and CuO alongside Cu_4O_3 from the liquid itself. Therefore we tried to replace $Cu(NO_3)_2{\cdot}3H_2O$ with other reagents. We tried to

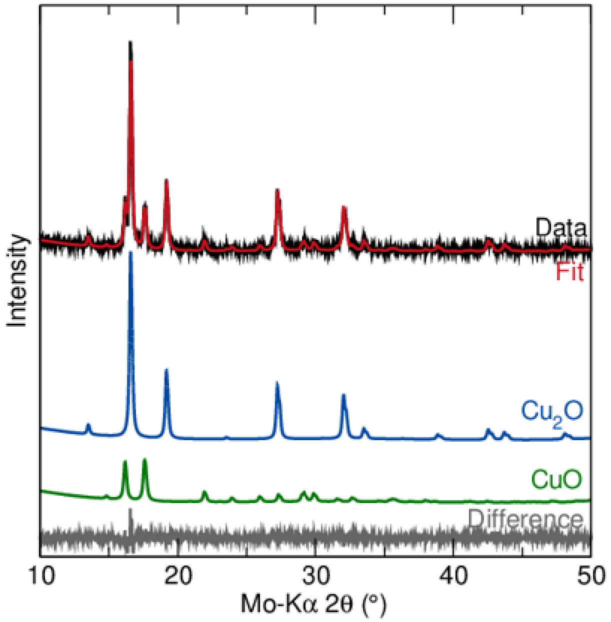

Figure 4.1: Rietveld refinement result on the solvothermal conversion product of $Cu_2(NO_3)(OH)_3$ in a liquid medium of DMF (33 vol%) and ethanol. No Cu_4O_3 was produced with this reaction.

deliberately add water to account for hydration in $Cu(NO_3)_2{\cdot}3H_2O$. We tried to add nitrate anions in the form of $NaNO_3$. We also tried to add in Cu(I) ions in the solution with the addition of CuCl, as the kinetic map shows that there were decent Cu(I) ions in the solution with the original synthesis scheme. Unfortunately, none of these additions helped to form Cu_4O_3.

Demonstrations that $Cu_2(NO_3)(OH)_3$ can indeed be solvothermally transformed to Cu_4O_3 was shown with the use of "solvothermal remnant liquid" as the liquid medium. This "remnant liquid" is the supernatant liquid generated from the previous Cu_4O_3 synthesis reaction with the original scheme using $Cu(NO_3)_2{\cdot}3H_2O$, DMF, and ethanol. After 24 hours of reaction, the supernatant liquid was separated from the solid precipitates using centrifugation. Solvothermal reaction of $Cu_2(NO_3)(OH)_3$ dispersed in this "remnant liquid" successfully created samples whose XRD pattern showed the characteristic peak of Cu_4O_3 (Figure 4.2). Since such "remnant liquid" was shown to be no longer able to precipitate on its own based on the previous kinetic study, the Cu_4O_3 formed here is considered to be the result of the

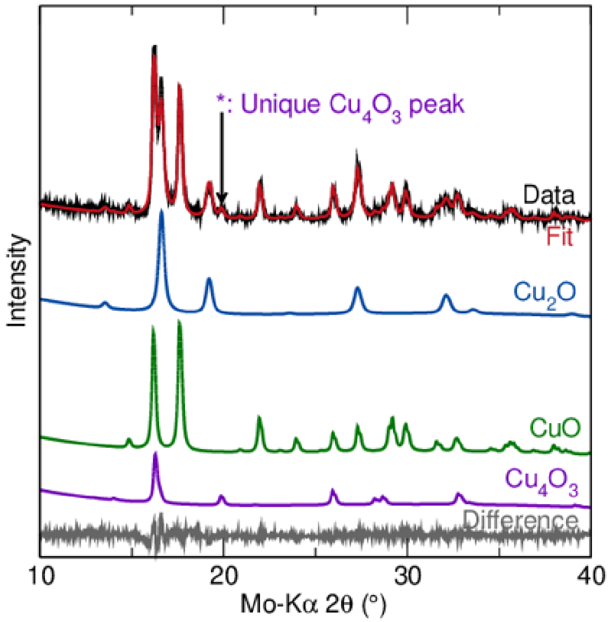

Figure 4.2: Rietveld refinement result on the solvothermal conversion product of $Cu_2(NO_3)(OH)_3$ using "solvothermal remnant liquid". Some Cu_4O_3 was produced with this reaction.

Table 4.1: The success of forming Cu_4O_3 by solvothermally reacting $Cu_2(NO_3)(OH)_3$ in various liquid medium

Precursor	**Liquid Medium**	**Cu_4O_3 in product?**
$Cu_2(NO_3)(OH)_3$	DMF	No
	ethanol + DMF	No
	ethanol + DMF + H_2O	No
	ethanol + DMF + Cu^+Cl^-	No
	ethanol + DMF + $Na^+(NO_3)^-$	No
	"solvothermal remnant liquid"	Yes

transformation of $Cu_2(NO_3)(OH)_3$.

The result of the success on forming Cu_4O_3 by solvothermally transforming $Cu_2(NO_3)(OH)_3$ is shown in Table 4.1. The fact that Cu_4O_3 could only be synthesized with the use of "remnant liquid" but not with any other chemical mixtures indicate that there were specific chemicals in the "remnant liquid" responsible for the effect. These chemicals were the result of complex chemical reactions between $Cu(NO_3)_2{\cdot}3H_2O$, DMF, and ethanol in the solvothermal condition. Although they were in trace amount hard to be detected, their presence drastically altered the thermodynamics / kinetics of Cu_4O_3 formation.

Gas chromatography mass spectroscopy (GC-MS) was used on the “solvothermal remnant liquid” to get a clue on the possible chemical identities of these trace chemicals. Some trace chemicals suggested in the results are N-nitrosodimethylamine, 1,1-diethoxy-ethane, 1,1-dimethyl-2-oxohydrazine, 1,1,3-triethoxy-propane, ethyl N,N-dimethyloxamate, ethyl ester 4-pyridinecarboxylic acid, methyl salicylate, 1,3-dimethyl-2,4,5-imidazolidinetrione, benzoic acid, 1,3-bis(1,1-dimethylethyl)-benzene. The chromatography profile for the unreacted solvent (ethanol + DMF) was much cleaner, so these are likely the result of solvothermal reactions. However, at this trace level, the confidence levels on assigning the correct chemical compounds by selecting retention peaks and matching MS data are low. We did not carry out quantitative analysis, but if these trace chemicals existed, they were probably on the ppm level of concentrations. Although these GC-MS suggestions are not to be fully trusted, they do show that the solvothermal chemistry between $Cu(NO_3)_2{\cdot}3H_2O$, DMF, and ethanol is extremely complicated in terms of organic chemistry. It is surprising that the presence of chemicals in such trace amount could have such a huge impact on the formation and stability of Cu_4O_3. Through literature review, it is found that all demonstrations of wet chemical Cu_4O_3 syntheses used some kinds of nitrogen-containing chemicals. [76, 77, 99] Therefore I postulate that some specific kind of Cu–N interaction is related to the stability of Cu_4O_3 prior to its formation. This interaction is likely to be weak, which could be a form of dynamic coordination bond within the liquid phase.

4.3.2 Solvothermal Conversion of $Cu(NO_3)_2$ in Various Solvents and the Discovery of New Copper Compounds

We substituted DMF in the original Cu_4O_3 synthesis scheme with another solvent, with the hope of finding another liquid environment capable of producing Cu_4O_3. The chemicals testing include two groups: C-H-O based organic acid, and N-containing small molecules. The list of chemicals tested are summarized in Figure 4.3. We did not succeed in producing Cu_4O_3 in this endeavor, but created several samples whose diffraction patterns cannot be

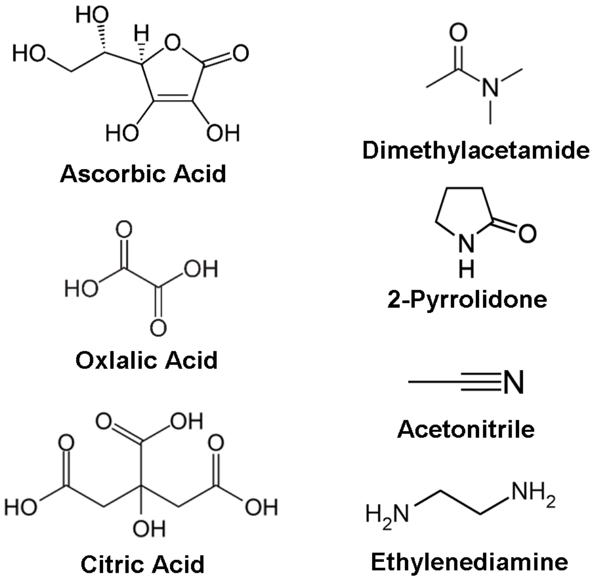

Figure 4.3: Chemicals tested in the solvothermal synthesis of Cu-containing inorganic materials with ethanol and $Cu(NO_3)_2{\cdot}3H_2O$.

matched with anything using the automated matching from Jade software (based on JCPDS database) and therefore are likely new types of Cu-containing inorganic materials.

Ascorbic acid was shown to be a very strong reducing agent, but at low concentrations, an unidentified phase is shown (Figure 4.4). When 33 vol% and 10 vol% ascorbic acid was used in the solvent, only metallic Cu was shown to be present after solvothermal reaction. The amount of ascorbic acid had to be reduced to decrease reduction power. With 1 vol% ascorbic acid, Cu was seen to dominate (Figure 4.4(a)), but there were some other low-intensity diffraction peaks. These peaks were more obvious at an even lower ascorbic acid concentration (0.1 vol%). Cu_2O, instead of Cu, was present at this stage. The difference curve after the removal of Cu_2O signals shows strong Bragg peaks (Figure 4.4(b)), which is similar to the peaks seen in Figure 4.4(a). The origin of these peaks is unknown and could be due to a new form of copper compound.

With the use of 33 vol% oxalic acid, we got a sample whose diffraction pattern is shown in Figure 4.5. This pattern is similar to that of the copper(II) oxalate recently discovered by Christensen *et al.*, with a chemical formula CuC_2O_4. [100] Using the suggested crystal

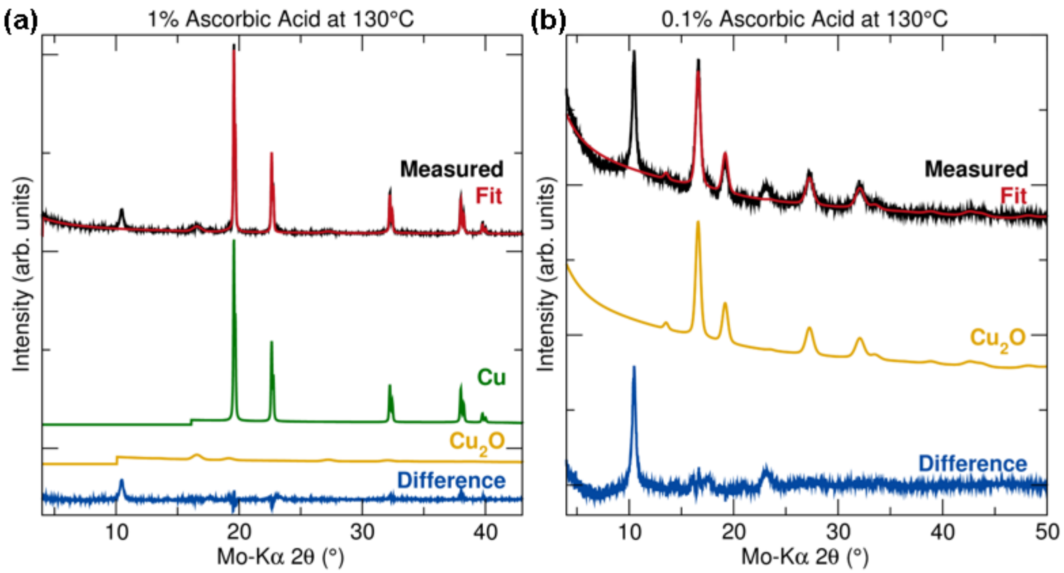

Figure 4.4: XRD patterns for the solvothermal products with the use of different concentrations of ascorbic acid. The unmatched peaks show the potential of having a new Cu-containing inorganic material.

structure from Christensen *et al.*, we were able to perform a Rietveld refinement for this phase (Figure 4.5) and confirmed what we got is indeed phase pure Cu(II) oxalate.

With the use of 33 vol% citric acid, we got a sample whose diffraction pattern are not that of any other copper oxides (Figure 4.6(a)). We did not find a match for it with published crystal structures and this is likely a new material. TGA analysis showed that it lost almost half of its mass easily at low temperatures ($\leq$ 237 °C) and has two turning points at 237 °C and 313 °C (Figure 4.6(b)). The loss of mass at low temperatures, together with large *d*-spacings (evidenced by the low angles of diffraction peaks) suggest this is a large unit cell structure containing some weak bonds, similar to $Cu_2(NO_3)(OH)_3$. SEM analysis showed that it had plate-like morphology similar to $Cu_2(NO_3)(OH)_3$ as well (Figure 4.6(c)). The exact crystal structure and chemical composition of it still needs to be determined.

When DMF was substituted with dimethylacetamide (DMA), Cu_4O_3 could no longer be produced. With the use of 33 vol% DMA, the solvothermal product consisted of CuO, Cu_2O, and Cu (Figure 4.7(a)). When DMA concentration was reduced (for example 25 vol%), $Cu_2(NO_3)(OH)_3$ started to dominate (Figure 4.7(b)). DMA is very similar in the molec-

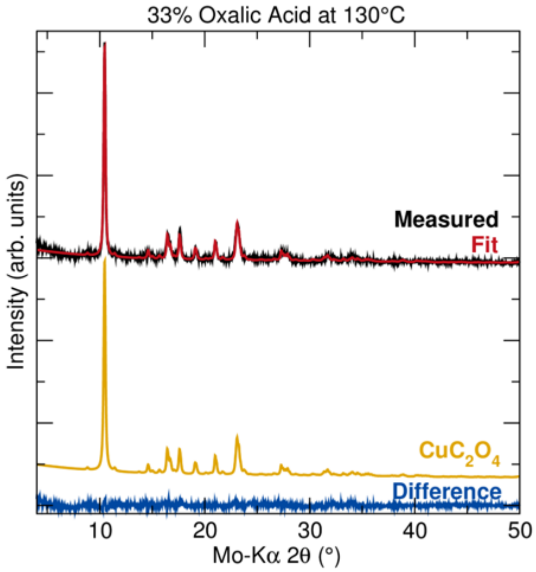

Figure 4.5: XRD patterns for the solvothermal products with the use of oxalic acid. Rietveld refinement shows that the product is copper(II) oxalate.

ular structure to DMF. Both are N,N-dimethylamide. DMA is only one methylene group (CH_2) group extra compared to DMF, but this extra methylene means that DMA does not contain the aldehyde functional group that DMF has. Apparently, this methylene group difference caused significant changes in chemistry. Both DMF and DMA caused solvothermal precipitation of $Cu_2(NO_3)(OH)_3$, CuO, and their reduction, but only with DMF could $Cu_2(NO_3)(OH)_3$ be converted to Cu_4O_3. Therefore the chemical substances responsible for Cu_4O_3 stability must have their origins with the aldehyde group in DMF.

With the use of 33 vol% 2-pyrrolidone, we recovered solid-phase precipitates but XRD showed that this solid was almost amorphous (Figure 4.8(a)). SEM showed that the precipitates were very fine in size (Figure 4.8(b)). This showed that when subjecting to such solvothermal reactions, the bonding arrangement between Cu ions and the adjacent molecular units can be very dynamic that even in the solid state well-defined structural periodicity did not form.

With the use of 33 vol% acetonitrile, the products produced XRD patterns that we could not match to any structures known (Figure 4.9(a)). The same structure was produced with three different solvothermal temperatures (110, 120, and 130°C). This new material

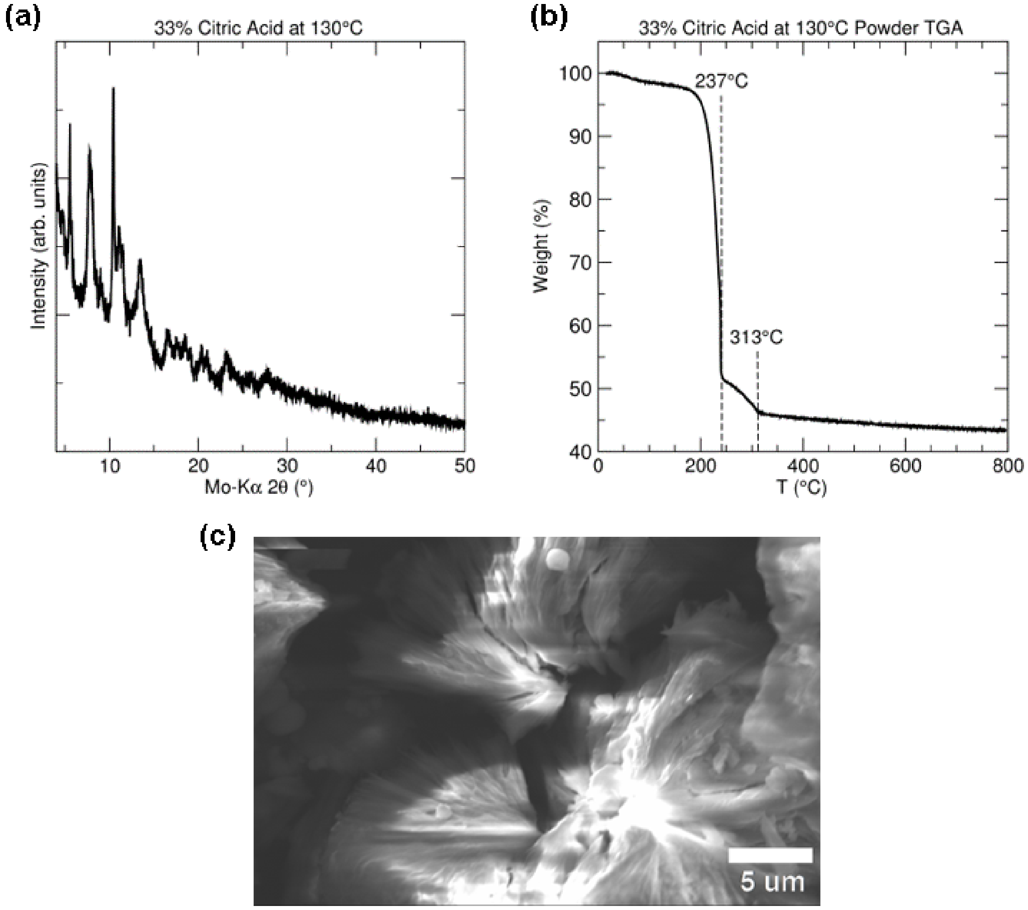

Figure 4.6: (a) XRD pattern, (b) TGA analysis, and (c) SEM image for the solvothermal products with the use of citric acid. The unmatched diffraction peaks show the potential of having a new Cu-containing inorganic material.

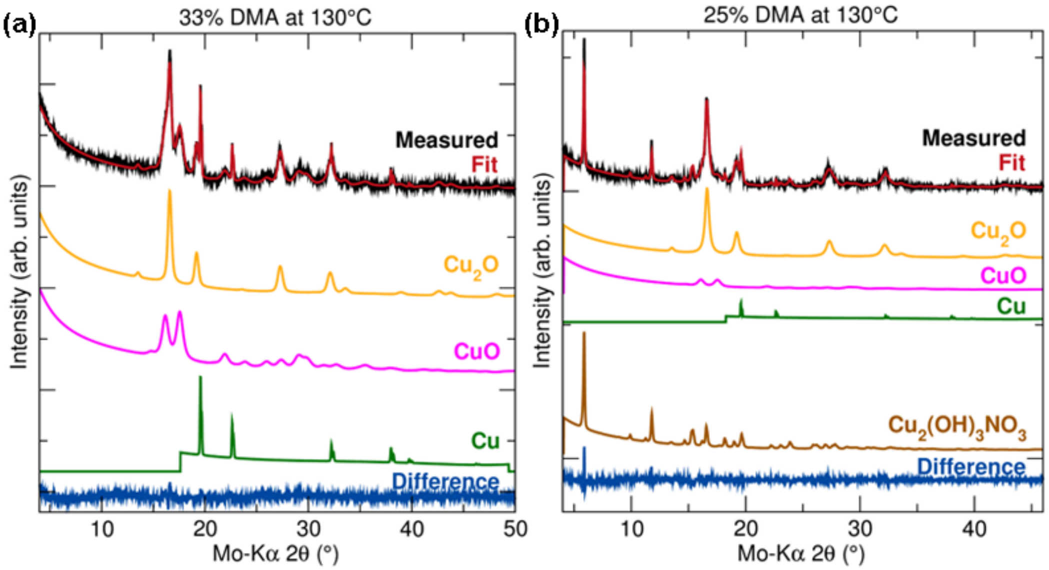

Figure 4.7: XRD patterns for the solvothermal products with the use of DMA with (a) 33 vol% and (b) 20 vol% concentrations. No unusual phases were seen.

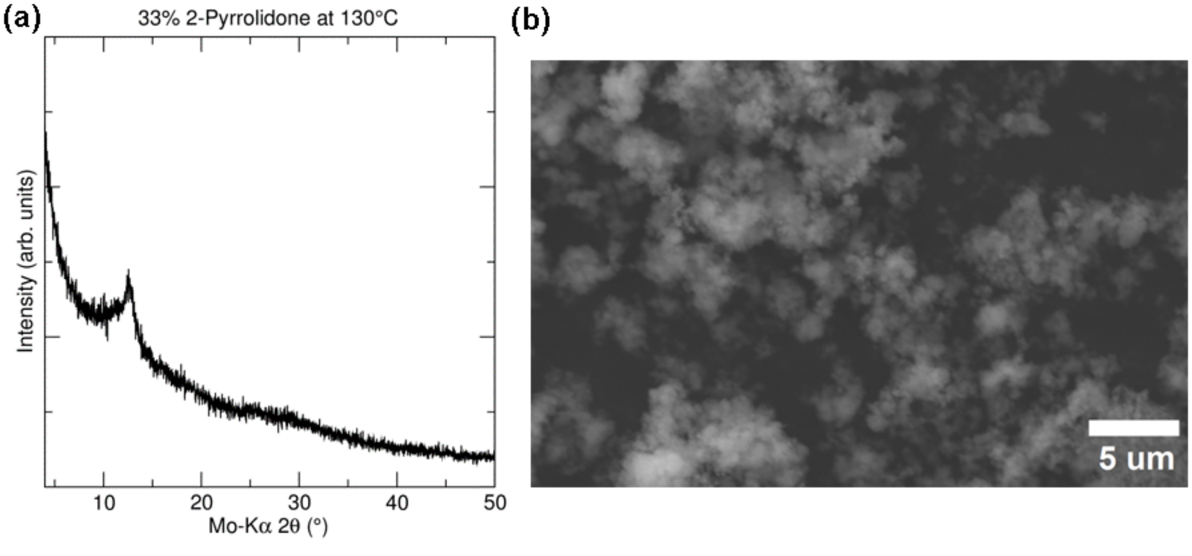

Figure 4.8: (a) XRD pattern and (b) SEM image for the solvothermal products with the use of 2-pyrrolidone. The product is a Cu-containing amorphous phase.

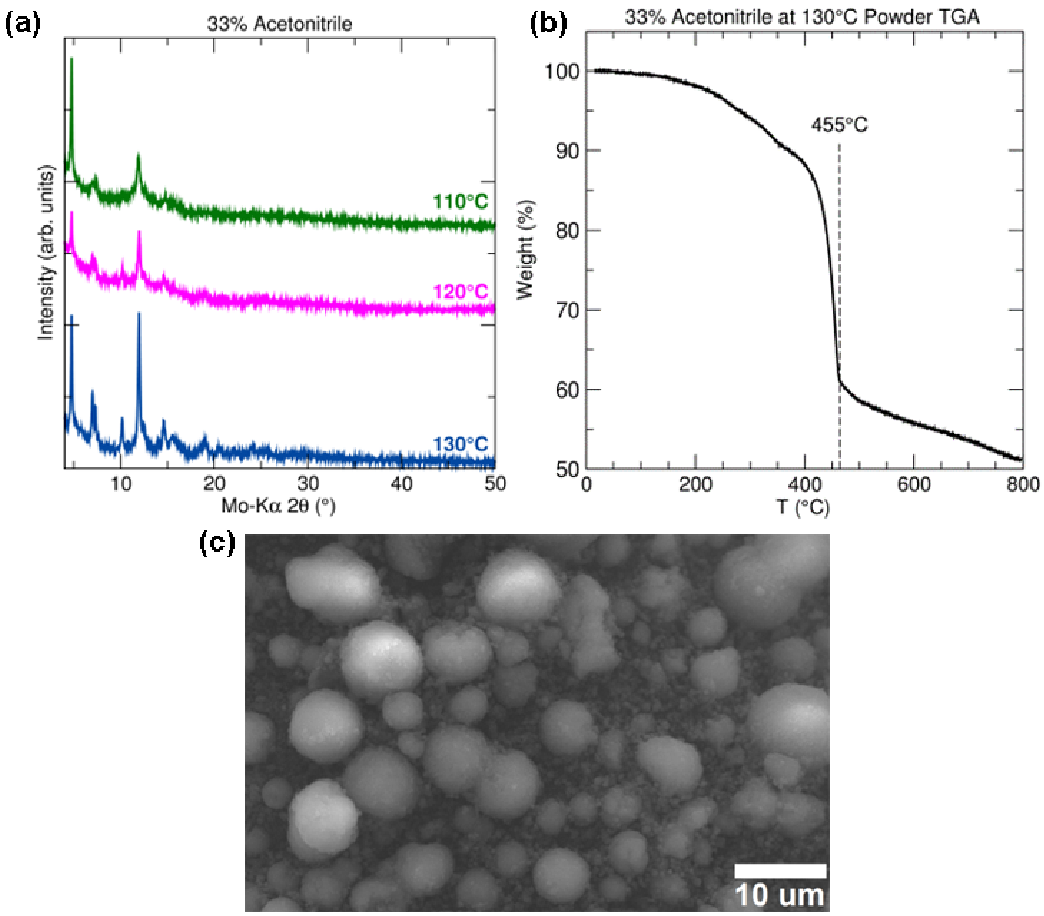

Figure 4.9: (a) XRD pattern, (b) TGA analysis, and (c) SEM image for the solvothermal products with the use of acetonitrile. The unmatched diffraction peaks show the potential of having a new Cu-containing inorganic material.

is brown in color is shown from SEM image to aggregate into micron-sized spheres (Figure 4.9(c)). TGA analysis showed that it was thermally stable up to 400°C, until it underwent a transformation at around 455 °C (Figure 4.9(b)). This good thermo-stability is in sharp contrast to the new structure derived from citric acid (Figure 4.6(b)). We have not yet solved the exact crystal structure and chemical composition of it, which warrants further investigation.

With the use of 33 vol% ethylenediamine, we were able to grow large needle-shaped crystals mm-long in length. With the use of single crystal XRD, we were able to solve its crystal structure. It was found to be a new structure type and have a unique coordination stereochemistry. Details about this compound is presented in the next chapter.

In this part of the work, we were able to solvothermally produce 6 other Cu-containing phases that are neither binary copper oxide nor metallic Cu. Among these, 4 are newly discovered crystalline sample (with the use of ascorbic acid, citric acid, acetonitrile, and ethylenediamine) and 1 is amorphous (with the use of 2-pyrrolidone). These results verify that in these solvothermal environments, Cu is very sensitive to local complexation chemistry, which can significantly influence the thermodynamic and kinetic stabilities of the various Cu-containing inorganic materials. Therefore, finding the right chemical environment to stabilize a particular form of Cu-structure can be a tricky task that requires very detailed understanding of local bonding chemistry in the liquid.

4.4 Conclusions

The effects of precursor chemistry on the solvothermal formation of Cu-containing inorganic materials were tested. It was shown that slight changes in precursor chemistry could have drastic effects on the relative thermodynamic and kinetic stabilities of the competing phases during solvothermal reactions. Although we were unable to identify an exact condition that can be employed to consistently produce phase-pure Cu_4O_3, the search for Cu_4O_3 had let us discover many new Cu-containing inorganic materials.

Although $Cu_2(NO_3)(OH)_3$ is a direct predecessor to Cu_4O_3, its direct solvothermal conversion to Cu_4O_3 was proven difficult. A simple solution mixture of DMF and ethanol did not make an adequate medium to produce Cu_4O_3. The "solvothermal remnant liquid" was found to have this potential. The active ingredients within should come from the complex chemistry between $Cu(NO_3)_2{\cdot}3H_2O$, DMF and ethanol under solvothermal condition. GC-MS gave some suggestions about these ingredients.

When DMF was switched to another compound, it was shown that the solvothermal chemistries were changed dramatically. Other forms of copper-containing inorganic materials were produced. We have found up to 4 new Cu-containing crystalline substances here. They were made by substituting DMF with citric acid, acetonitrile, ascorbic acid, and ethylenediamine respectively. Except for the ethylenediamine case, the crystal structures of these new materials are yet to be solved. Revisions of the synthesis scheme to produce more suitable samples for structure solution is required. The results indicate that changes in the solvothermal chemical environment have a huge impact on the stability of the various Cu-containing phases. A thorough understanding of the dynamic complexation of Cu-ions with other molecules is needed for this task, which is challenging at the moment.

CHAPTER 5

A NEW INORGANIC Cu-STRUCTURE WITH UNIQUE COORDINATION STEREOCHEMISTRY

5.1 Introduction

The investigation on the change of solvent environment on Cu_4O_3 formation led us to realize the importance of local coordination chemistry on the formation of Cu_4O_3. As an effort of testing $Cu(NO_3)_2$ interaction with various N-containing chemicals, we stumbled upon a new crystal structure that grew to long single-crystal needles when working with ethylenediamine.

Ethylenediamine (en) is one of the most prevalent ligands in coordination chemistry and was once termed “God’s gift to coordination chemist”. [101] It is the most widely studied bidentate amine and readily forms highly stable five-membered metallocyclic rings when chelating a metal ion. Coordination compounds with en ligands and its derivatives are also used in the pharmaceutical [102–104], agricultural [105], polymer [106], bleaching [107] and industrial sectors [108]. The propensity of en to coordinate with metals also makes it a versatile reagent for the synthesis of inorganic materials through dissolution of metal salts or oxides, which can be engineered to precipitate in other crystalline forms. [29, 109, 110]

Ethylenediamine is prevailingly found to be bidentate. Monodentate or bridging forms of en are extremely rare. [111, 112] However, many kinetic intermediate species in a variety of important chemical processes have been proposed to contain complexes containing monodentate and bridging en with *trans* conformations. For instance, the ligand displacement reaction of a hexadentate cobalt(III) complex from $EDTA^{4-}$ and $PDTA^{4-}$ by en was rate-determined by the monodentate NH_2 coordination of the first en group. [113] The isomerisation of the hydroxoammine complexes of cobalt(III) was found to involve unimolecular dissociation on one end of an en chelating ring. [114] A monodentate en complex was detected from the aquation of [*trans*-Cr(en)$_2$F$_2$]$^+$, a low-lying σ-antibonding compound with important electron-transfer and photochemical characteristics. [115] During the en-based solvothermal synthesis of magnetic chalcogenides $KFeS_2$ and KFe_2S_3, formation of Fe_2S_3 sheets connected by bridging en was suggested as the first reaction intermediate. [29] However, these prior studies on monodentate en describe possible transient reaction intermediates, and the existence of monodentate en is only speculated upon based on spectroscopic evidence of solution-phase species. Only a few solid state compounds containing monodentate en have been crystallographically confirmed recently. [116–119] But in these examples, protonated enH is the actual monodentate ligand, and multiple ligands are involved in the metal coordination, so the steric and electronic effects are not entirely comparable to the case where en ligands are free to bond and dissociate.

Here, we recorded the crystallization and structure solution of (ethylenediamine-N)-bis(ethylenediamine-N,N')-copper(II) bis(nitrate) for the first time (Fig. 5.1). It is a penta-coordinated complex with two chelating and one monodentate en ligands with severely trigonally distorted square pyramidal stereochemistry. To the best of our knowledge, it is the first crystallographic confirmation for the existence of monodentate en when no other chemical species are introduced as mixed ligands. Such penta-coordination chemistry with en ligands has never been observed with any metal centers. The non-coordinating amine of this en is not protonated, and the N atom participates in hydrogen bonding to the amine H of a chelating en in the adjacent complex. It is also the first crystallographically characterized Cu ion coordinated to monodentate en. This unique coordination chemistry might originate from the penta-ammine effect. However, the penta-ammine effect is usually realized with five NH_3 ligands, or at least one mono-amine ligand is employed. [120] Here, it is demonstrated that even with only the short bi-amine complex en, penta-amine coordination is still possible. Spectroscopic characterization of this compound supports the crystallographic assignment of square-pyramidal-based Cu(II)-tris(en) complex with penta-coordination. The insights from

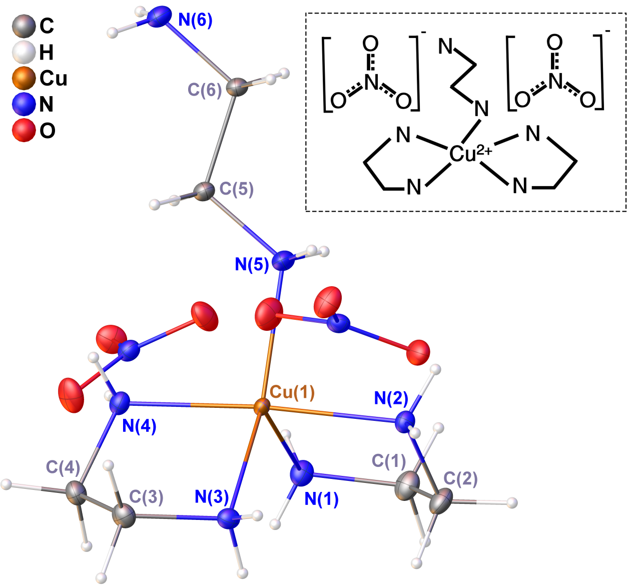

Figure 5.1: Asymmetric unit of [Cu(en-N)(en-N,N')$_2$](NO$_3$)$_2$. Anisotropic displacement ellipsoids (except H) are drawn at the 50 % level. The inset shows its chemical diagram. Cu(II) is coordinated to two bidentate en and one monodentate en in this structure.

the stereochemistry of this complex are valuable to the analysis of reaction mechanisms and kinetics involving en ligands for coordination chemistry.

5.2 Synthesis and Characterization

A solution of 50 mM $Cu(NO_3)_2 \cdot 3H_2O$ with 33.3 vol% ethylenediamine was prepared by dissolving 0.1812 g of $Cu(NO_3)_2 \cdot 3H_2O$ in a mixture of 10 mL ethanol and 5 mL ethylenediamine. The resulting solution (15 mL) was placed in a 23 mL capacity teflon-lined autoclave (Parr Instruments). The system was transferred into a preheated oven at 130 °C for 24 h. A homogeneous blue liquid was obtained after air-cooling the autoclave to room temperature, which was then transferred into a closed polypropylene centrifuge tube. Needle-shaped single crystals millimeters long in length formed from the liquid over a resting period of 24–72 h (Fig. 5.2).

Crystals of the same structure can be prepared without the solvothermal heating step. However, significantly increased single crystal precipitation rate and larger needles were

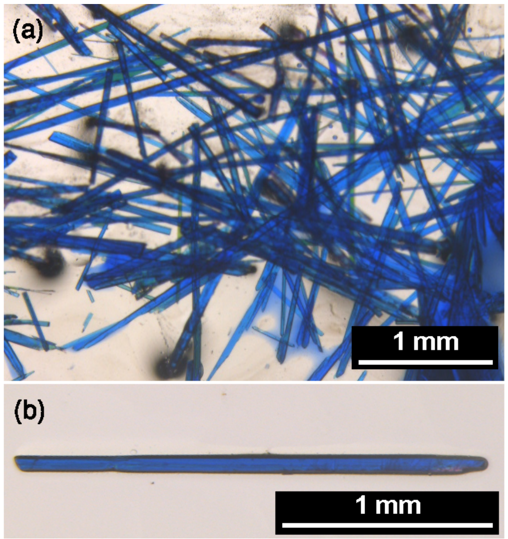

Figure 5.2: Optical microscopy images of the blue needle-shaped $[Cu(en\text{-}N)(en\text{-}N,N')_2](NO_3)_2$ crystals.

observed with the solvothermal treatment.

A suitable crystal was selected, chopped to proper length, and mounted on a Bruker D8 Venture diffractometer equipped with a Photon 100 detector using multilayer optics to monochromatize Mo Kα radiation for single crystal diffraction. The crystal was kept at 100 K during data collection. Using Olex2 [121], the structure was solved with the ShelXT [122] using intrinsic phasing and refined with the ShelXL [123] refinement package using least squares minimisation.

After precipitation of the crystals, inductively coupled plasma optical emission spectroscopy (ICP-OES) was performed on the supernatant liquid using the PerkinElmer Optima 8300 to determine the Cu elemental concentration.

Heating or vacuum treatment will lead to structural changes of the crystals. Therefore, the powder samples used in the following characterizations were isolated from the liquid, dried at room temperature for solvent evaporation (sometimes with nitrogen gas flow) before performing the measurement. However, we expect some solvent molecules remaining adsorbed onto the crystals with such drying process (based on the mismatch of Cu ICP result of supernatant liquid and mass result of the dried precipitates). Powder X-ray diffraction (XRD) patterns were recorded on a Bruker D8 ADVANCE diffractometer equipped with Mo K_α source and LYNXEYE XE detector. Each sample was compacted inside a glass capillary and the diffraction was recorded in transmission configuration. Magnetic susceptibilities were recorded on a Quantum Design MPMS3 in the temperature range of 5–300 K under a magnetic field of 1000 Oe. The crystals were compacted into a cylindrical disc before magnetic measurement. Raman spectra were recorded using a Nanophoton Raman 11 confocal microscope with 532 nm laser excitation. Diffuse reflectance ultraviolet-visible-near-infrared (UV-Vis-NIR) spectroscopy measurements were performed on a Varian Cary5G spectrometer. The sample crystals were placed on top of a $BaSO_4$ powder bed, with pure $BaSO_4$ powder used as reflection standard. The measured diffuse reflectance was converted to absorbance using the Kubelka-Munk transform.

5.3 Results and Discussion

5.3.1 Crystallography

Blue needle-shaped single crystals precipitated from 50 mM $Cu(NO_3)_2$ ethanolic solution with 33.3 vol% ethylenediamine (en) days after solvothermal treatment (Fig. 5.2). The supernatant liquid after the precipitation of crystals was examined by ICP-OES to determine the Cu concentration. Based on the ICP-OES and density measurement results, it was calculated that at most 26% of the initial Cu elements were retained in the liquid. Therefore, the precipitation yield was at least 74% for this synthesis process in terms of Cu element.

Single crystal X-ray crystallography established monoclinic space group $P2_1/c$ with lattice parameters a = 12.8262(5)Å, b = 9.7712(4)Å, c = 11.9065(5)Å, and β = 94.8220(10)° at 100 K for the precipitated needles. The asymmetric unit consists of one mononuclear Cu(II) ion coordinated by three en ligands and two symmetrically inequivalent noncoordinating nitrate counter anions (Fig. 5.1). This renders its chemical formula of $[Cu(en)_3](NO_3)_2$. Detailed atomic coordinates and the anisotropic displacement parameters of the [Cu(en-

Table 5.1: Fractional atomic coordinates and equivalent isotropic displacement parameters ($Å^2$) for $[Cu(en\text{-}N)(en\text{-}N,N')_2](NO_3)_2$. The crystal has space group $P2_1/c$, with a = 12.8262(5) Å, b = 9.7712(4) Å, c = 11.9065(5) Å, and β = 94.8220(10) °. The data was collected at 99.96 K. Hydrogen atom coordinates are provided in Table 5.2.

Atom	*x*	*y*	*z*	**U(eq)**
Cu(1)	0.77022(2)	0.07870(2)	0.25688(2)	0.00713(6)
N(1)	0.73723(9)	-0.01800(12)	0.08986(9)	0.0122(2)
N(2)	0.92029(8)	0.03499(11)	0.22635(9)	0.0093(2)
N(3)	0.76670(9)	-0.07708(11)	0.37197(9)	0.0101(2)
N(4)	0.61950(8)	0.10589(11)	0.28731(9)	0.0105(2)
N(5)	0.80017(9)	0.28290(11)	0.22735(11)	0.0146(2)
N(6)	0.70314(9)	0.64783(11)	0.26478(10)	0.0134(2)
C(1)	0.83916(10)	-0.05158(14)	0.04763(11)	0.0146(2)
C(2)	0.91836(10)	-0.08133(13)	0.14685(11)	0.0139(2)
C(3)	0.67263(10)	-0.05732(13)	0.43371(10)	0.0122(2)
C(4)	0.58395(10)	-0.01559(13)	0.34804(11)	0.0122(2)
C(5)	0.72527(9)	0.39334(12)	0.24597(10)	0.0105(2)
C(6)	0.77382(9)	0.53596(12)	0.24033(10)	0.0101(2)
O(1)	1.03807(7)	0.12595(9)	0.44802(8)	0.01368(18)
O(2)	1.00958(7)	0.20804(10)	0.61215(7)	0.01544(19)
O(3)	0.88349(7)	0.20377(10)	0.47803(8)	0.0186(2)
N(7)	0.97700(8)	0.17867(10)	0.51220(9)	0.0102(2)
O(4)	0.60586(7)	0.22205(10)	-0.00091(8)	0.0172(2)
O(5)	0.47413(7)	0.12980(11)	0.07470(8)	0.0178(2)
O(6)	0.45479(7)	0.20662(10)	-0.09722(8)	0.01535(19)
N(8)	0.51145(8)	0.18576(10)	-0.00768(9)	0.0104(2)

$N)(en\text{-}N,N')_2](NO_3)_2$ crystal are provided in Tables 5.1 and 5.2.

Powder XRD patterns for the precipitated crystals are provided in Fig. 5.3. As discussed in the caption of Fig. 5.3, the pristine crystals showed very good agreement with the calculated powder XRD pattern based on its single crystal structure solution, but with the presence of preferred orientation, which was to be expected due to their needle shapes. Therefore, we conclude that our precipitates have good single-phase purity.

The coordination geometry of our crystal, however, is different from all copper tris(en) complex crystals known to date. Previously reported crystals containing $[Cu(en)_3]^{2+}$ complexes are ubiquitously 6-coordinated with three chelating en ligands. For our crystal, the three en ligands coordinate differently: two en ligands are bidentate (chelating) as commonly

Table 5.2: Hydrogen atom coordinates and equivalent isotropic displacement parameters (Å^2) for $[Cu(en\text{-}N)(en\text{-}N,N')_2](NO_3)_2$ with space group $P2_1/c$, a = 12.8262(5) Å, b = 9.7712(4) Å, c = 11.9065(5) Å, and β = 94.8220(10) °. CH_2 hydrogens were constrained while NH_2 hydrogens were freely refined.

Atom	*x*	*y*	*z*	**U(eq)**
H(1A)	0.7041(15)	0.0400(20)	0.0455(16)	0.027(5)
H(1B)	0.7011(15)	-0.0860(20)	0.0923(16)	0.026(5)
H(2A)	0.9493(14)	0.1051(19)	0.1968(15)	0.023(5)
H(2B)	0.9565(13)	0.0160(17)	0.2877(15)	0.016(4)
H(3A)	0.7611(13)	-0.1558(18)	0.3366(14)	0.017(4)
H(3B)	0.8189(15)	-0.0784(17)	0.4158(15)	0.019(4)
H(4A)	0.5821(14)	0.1197(19)	0.2243(16)	0.025(5)
H(4B)	0.6119(13)	0.1741(18)	0.3276(15)	0.020(4)
H(5A)	0.8201(15)	0.2910(20)	0.1613(17)	0.031(5)
H(5B)	0.8536(17)	0.2920(20)	0.2729(18)	0.035(5)
H(6A)	0.6575(15)	0.6594(19)	0.2078(16)	0.026(5)
H(6B)	0.6708(14)	0.6311(18)	0.3207(16)	0.020(4)
H(1C)	0.863583	0.026226	0.003481	0.018
H(1D)	0.831715	-0.132555	-0.002372	0.018
H(2C)	0.898778	-0.166268	0.185232	0.017
H(2D)	0.988626	-0.094449	0.119925	0.017
H(3C)	0.68532	0.014896	0.491569	0.015
H(3D)	0.654808	-0.143296	0.471702	0.015
H(4C)	0.566752	-0.091363	0.294463	0.015
H(4D)	0.520658	0.006929	0.386528	0.015
H(5C)	0.698334	0.380821	0.320808	0.013
H(5D)	0.665201	0.386599	0.188319	0.013
H(6C)	0.836501	0.540213	0.294738	0.012
H(6D)	0.797217	0.549815	0.164008	0.012

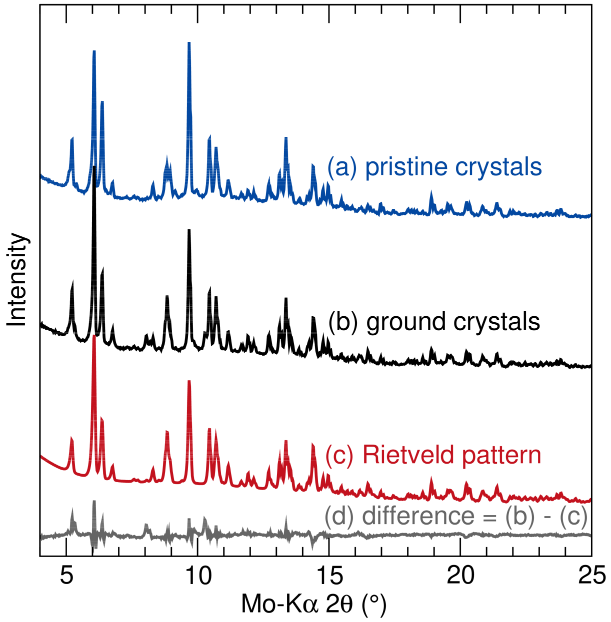

Figure 5.3: (a) Powder XRD pattern taken by compressing the dried precipitate crystals directly into a glass capillary. (b) Powder XRD pattern taken by first grinding the dried precipitates before packing into the capillary. (c) Theoretical powder XRD pattern of $[Cu(en\text{-}N)(en\text{-}N,N')_2](NO_3)_2$ from Rietveld refinement on pattern (b). (d) The difference curve between (b) and (c). The ground sample (b) has no texture as compared to the needle-shaped crystals (a), which is preferred for Rietveld analysis (c). The major misfit peaks seen in (d) are not present in (a), so these misfit peaks are likely a consequence of grinding. Therefore, the pristine crystals are expected to be almost pure $[Cu(en\text{-}N)(en\text{-}N,N')_2](NO_3)_2$.

found, but the third en ligand is monodentate, making this copper tris(en) complex 5-coordinated. Therefore, the proper name for this compound should be (ethylenediamine-N)-bis(ethylenediamine-N,N')-copper(II) bis(nitrate), with chemical formula of $[Cu(en\text{-}N)(en\text{-}N,N')_2](NO_3)_2$ to precisely reflect the uniqueness of this coordination structure.

This $[Cu(en\text{-}N)(en\text{-}N,N')_2]^{2+}$ is penta-coordinated with distorted square pyramidal coordination geometry, with the chelating en donors at the four in-plane sites and the monodentate en donor at the apical site. Bonds between Cu(II) and the N donors in the two chelating en have an average distance of 2.04 Å. Chelating en can bond to central metal ions to form a five-membered puckered ring, with two possible enantiomeric conformations: λ and δ. [101] Our $[Cu(en\text{-}N)(en\text{-}N,N')_2](NO_3)_2$ is a racemate compound, with an equal mixture of $\lambda\lambda$ and $\delta\delta$ stereochemical forms.

The apical Cu(II)–N bond to the monodentate en has a longer bond distance of 2.21 Å. This disparity in bond distances is largely a consequence of the structural distortion originating from the $3d^9$ electronic configuration of Cu(II) (commonly present in penta-coordinated Cu complexes). This has similar underlying principle as the Jahn-Teller distortion in octahedrally coordinated structures with axial elongation. [124] This complex, therefore, is more accurately depicted as having "4+1" coordination, with a tetragonality T^5 of 0.923. [101,125]

The square pyramidal geometry of $[Cu(en\text{-}N)(en\text{-}N,N')_2]^{2+}$ is significantly trigonally distorted. The geometry index τ_5 can be used to describe such in-plane angular distortion. [126] The τ_5 value for $[Cu(en\text{-}N)(en\text{-}N,N')_2]^{2+}$ is calculated to be 0.464, almost at the midpoint between perfect square pyramid (τ_5=0) and trigonal bipyramid (τ_5=1).

The hydrogen bonding scheme in this crystal structure is visualized in Fig. 5.4 for a single asymmetric unit. Most of the hydrogen bonding interactions are between hydrogens in $[Cu(en\text{-}N)(en\text{-}N,N')_2]^{2+}$ and oxygens in $(NO_3)^-$. The only exception is the dotted green lines in Fig. 5.4 that connects adjacent $[Cu(en\text{-}N)(en\text{-}N,N')_2]^{2+}$ complexes along the b-axis and involves the non-coordinating N(6) as the acceptor. This hydrogen bond is relatively short and straight. Its H-A distance is 2.204 Å, one of the shortest H-bonds in this structure,

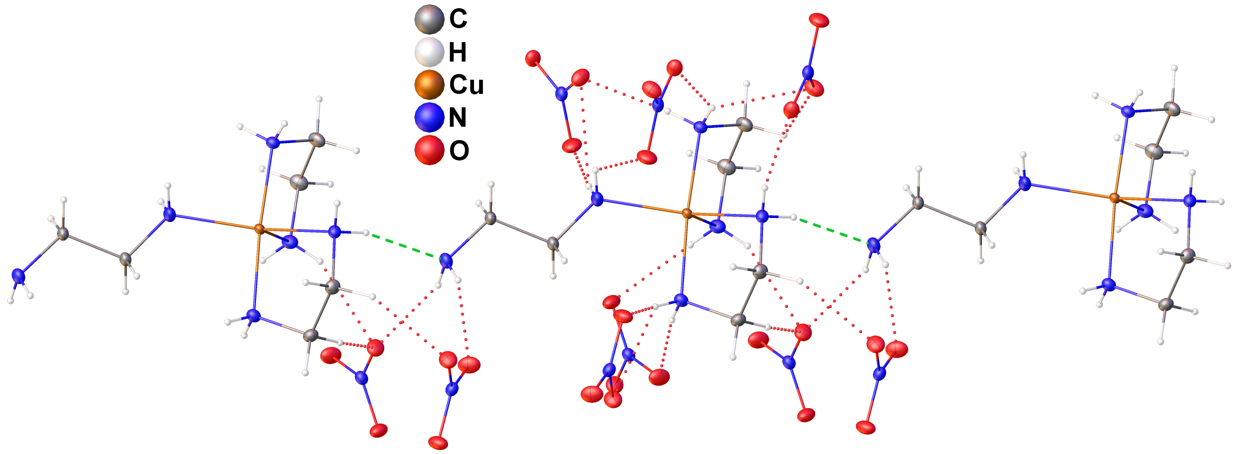

Figure 5.4: Hydrogen bonding in [Cu(en-N)(en-N,N')$_2$](NO$_3$)$_2$ crystal. Hydrogen bonds between [Cu(en-N)(en-N,N')$_2$]$^{2+}$ and nitrate are shown with dotted red lines. The hydrogen bonds between N(6) (*i.e.* the non-coordinating en N) and H(3A) in adjacent [Cu(en-N)(en-N,N')$_2$]$^{2+}$ complexes along b-axis are highlighted as thickened green dotted lines.

and its D-H-A angle is 164.0°. In fact, for the monodentate en, the coordination bond length (N donor to Cu: 2.21 Å) is almost the same as the hydrogen bond length (N acceptor to H: 2.20 Å). Therefore, this hydrogen bonding with N(6) is expected to have decent strength, which could weaken the Lewis basicity of N(6) and stabilize the monodentate en ligand.

5.3.2 Structural Comparison with Other Complexes

A penta-coordinated tris(ethylenediamine) complex as seen in our [Cu(en-N)(en-N,N')$_2$](NO$_3$)$_2$ has never been crystallographically confirmed before. In the absence of an overriding factor, a complex containing chelating five-membered metallocyclic rings is expected when en or N,N-substituted en derivatives are employed as ligands. [127] Bridging and monodentate forms of en are extremely rare. The early postulations of their existence mainly came from spectroscopic inference on liquid solutions of complexes, and are thus less reliable. [111, 112, 128, 129] Only very recently have a handful of monodentate and bridging en compounds been confirmed crystallographically. [116–118]

[Cu(en-N)(en-N,N')$_2$](NO$_3$)$_2$ differs from the other monodentate-en ligand compounds in three key aspects. First, no ligands other than en are present, whereas mixed-ligands donors are introduced in other examples to compete for chelating en ring formation through steric and electronic effects. Second, our $[Cu(en\text{-}N)(en\text{-}N,N')_2]^{2+}$ has a coordination number of 5, whereas all other examples have coordination number 6. Third, the monodentate en ligand in $[Cu(en\text{-}N)(en\text{-}N,N')_2](NO_3)_2$ is neutral, whereas in other structures mono-protonation occurs on the non-coordinating N of the monodentate en ligand.

Crystals with Cu(II) centers have never been reported with monodentate en, although an abundance of crystals containing Cu(II)-bis(en) and Cu(II)-tris(en) have been studied. [130–137] Our compound differs from the other 5-coordinated $[Cu(en)_2X]^{2+}$ complexes in two key aspects. First, the basal plane in our $[Cu(en\text{-}N)(en\text{-}N,N')_2]^{2+}$ has severe trigonal distortion whereas the others are fairly flat. Second, the apical coordination bond in $[Cu(en\text{-}N)(en\text{-}N,N')_2]^{2+}$ is not semi-coordinating as in the others with $\geq$2.5Å bond lengths. [138]

Perhaps the nearest comparable stereochemistry to $[Cu(en\text{-}N)(en\text{-}N,N')_2]^{2+}$ is the penta-ammine-Cu(II) complex as found in $K[Cu(NH_3)_5](PF_6)_3$. [120] In general, five-coordination of Cu(II) is hard to realize without mixed-ligands or π-bonding donors so as to introduce the possibility of bond-length and bond-angle distortion. However, NH_3 are known to exhibit a strong tendency to form CuN_5 chromophores with only σ-bonding, a phenomenon termed the penta-ammine effect. However, these penta-amine complexes typically uses ammine ligands, sometimes in combination with tetradentate / bidentate amine (such as $[Cu(tren)(NH_3)](ClO_4)_2$ and $[Cu(en)_2(NH_3)](BF_4)_2$. [120] The use of ammine has been required to form the fifth coordination site on top of the characteristic 4 coordination of Cu(II). [139] It is unprecedented to achieve the penta-ammine effect with only one type of ligand that is fundamentally bidentate as is the case in our $[Cu(en\text{-}N)(en\text{-}N,N')_2]^{2+}$.

The formation of this unique $[Cu(en\text{-}N)(en\text{-}N,N')_2](NO_3)_2$ can be examined as an intermediate between known complexes. The previously known Cu(II)-en complex with nitrate counterions is $[Cu(en\text{-}N,N')_2](NO_3)_2$. [130] We synthesized this compound pure when $\leq$ 10 vol% en is employed. Our structure is a tris(en) complex, and with certain counter-anions (*e.g.* acetate, oxalate, chloride, sulfate), crystalline $[\mathrm{Cu(en\text{-}N,N')_3}]^{2+}$ forms when the en to Cu(II) ratio is in excess of 3:1 in an aqueous environment. [134, 135, 140] However, no $[\mathrm{Cu(en\text{-}N,N')_3}]^{2+}$ has been reported in the solid state with nitrate. Our preliminary tests show that excess en prohibits crystallization. No crystalline precipitation will occur if en is $\geq$ 75 vol%. In this state, Cu(II) ions are expected to be present in the solution phase as $[\mathrm{Cu(en\text{-}N,N')_3}]^{2+}$, but crystallization of their solid state equivalence with nitrate anions is forbidden for some reasons unclear.

The ideal en concentration for crystalline $[\mathrm{Cu(en\text{-}N)(en\text{-}N,N')_2}](\mathrm{NO_3})_2$ formation should be larger than required for $[\mathrm{Cu(en\text{-}N,N')_2}](\mathrm{NO_3})_2$, but not in excess to fully stabilize solution $[\mathrm{Cu(en\text{-}N,N')_3}]^{2+}$. Within this range, the Cu-complexes in solution are speculated to be square-planar $[\mathrm{Cu(en\text{-}N,N')_2}]^{2+}$, with some en ligands in solution available to contribute to further coordination. [141] The existence of a stable 5-coordinated Cu complex with tris(en) ligands in solution, as is found in our solid state example, is highly unlikely due to the incompatibility of fast exchange dynamics in the liquid phase with the extreme structural distortion caused by such stereochemistry. We postulate that Cu(II) was initially present in the solution as $[\mathrm{Cu(en\text{-}N,N')_2}]^{2+}$, and during its condensation into solid state phase, the additional free en ligands participated in coordination by forming a fifth monodentate bond, achieving the penta-amine analog. The non-coordinating N in the monodentate en is partially stabilized through H-bonding, as demonstrated in Fig. 5.4. In the end, an equilibrium between $[\mathrm{Cu(en\text{-}N,N')_2}]^{2+}$ in solution and $[\mathrm{Cu(en\text{-}N)(en\text{-}N,N')_2}]^{2+}$ in solid state is achieved. This is in agreement of our observation that the liquid phase after precipitation remained blue, and the existence of a significant amount of Cu in liquid from ICP-OES. A schematic for this proposed formation of $[\mathrm{Cu(en\text{-}N)(en\text{-}N,N')_2}](\mathrm{NO_3})_2$ is shown in Fig. 5.5.

5.3.3 Spectroscopy and Magnetism

Raman spectra of $[\mathrm{Cu(en\text{-}N)(en\text{-}N,N')_2}](\mathrm{NO_3})_2$ crystal and pure liquid en are shown in Fig. 5.6. Modes of en have been assigned by Krishnan and Plane based on their study

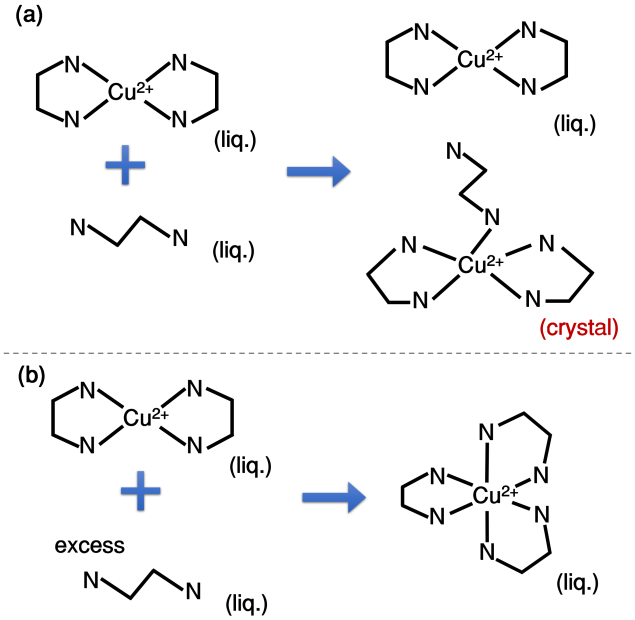

Figure 5.5: Proposed formation scheme of [Cu(en-N)(en-N,N')$_2$](NO$_3$)$_2$ crystals. With insufficient en ($\leq$ 10 vol% en), only [Cu(en)$_2$](NO$_3$)$_2$ precipitates. (a) In the ideal condition of 33 vol% en and 67 vol% ethanol, Cu(II) ions are first coordinated with two chelating en ligands, with some free en ligands in the solution. Over time, the fifth coordination bond forms between some [Cu(en)$_2$]$^{2+}$ and the free en, resulting in the precipitation of [Cu(en-N)(en-N,N')$_2$](NO$_3$)$_2$ crystals. (b) When there is excess en in the liquid ($\geq$ 75 vol% en), stable octahedral [Cu(en)$_3$]$^{2+}$ will form in solution, preventing the crystallization of [Cu(en-N)(en-N,N')$_2$](NO$_3$)$_2$. Cu(NO$_3$)$_2$ concentration is fixed at 50 mM pertaining to the above discussion.

of en in water and heavy water. [141] Compared with their results, peaks in our en Raman spectrum are slightly shifted, probably due to the exclusion of water, but the overall pattern is consistent. The Raman spectrum of the $[Cu(en\text{-}N)(en\text{-}N,N')_2](NO_3)_2$ complex seen in Fig. 5.6(a) has the modes originating from en shifted, which is to be expected due to en coordinating to metal ions. [141] As indicated in Fig. 5.6, the extent of peak shifts, however, are different depending on the vibrating atoms. Modes of CH_2 (twisting at 1317 cm^{-1}, bending at 1480 cm^{-1}) and NH_2 (wagging at 1396 cm^{-1}, bending at 1614 cm^{-1}) are observed with minimal shifts, whereas those corresponding to the en skeleton (bending at 541 cm^{-1}, stretching at 903 cm^{-1}, C–N stretching at 1132 cm^{-1}) have appreciable positive shifts. This can be appreciated considering that liquid en can freely transform between its trans and gauche(A,B) conformations [142], but once within the solid state complex, this freedom disappears and the molecule is markedly stiffer. The freedom of CH_2 and NH_2 vibrations, on the other hand, is not severely restricted by complex formation. Castro and Jagodzinski isolated three fundamental Raman peaks of ${NO_3}^-$ with cation-insensitive positions. [143] All these three nitrate Raman modes are present in $[Cu(en\text{-}N)(en\text{-}N,N')_2](NO_3)_2$, with very narrow peaks at 726, 1059, and 1346 cm^{-1}.

Low energy vibrations (less than 500 cm^{-1}) are generally associated with metal-donor coordinations. Five such strong Raman peaks can be easily identified for $[Cu(en\text{-}N)(en\text{-}N,N')_2](NO_3)_2$ in Fig. 5.6(a) at 245, 271, 339, 456, and 479 cm^{-1}. Generally, lower wavenumber modes are assigned to metal-nitrogen bending and higher wavenumber modes to metal-nitrogen stretching. [141] Critically, M–N stretching at *ca.* 420 cm^{-1} has been consistently observed in the tris(en) complexes of different metal ions, which is not the case for $[Cu(en\text{-}N)(en\text{-}N,N')_2](NO_3)_2$. This agrees with our crystallographic analysis that our tris(en) complex is 5-coordinated rather than the usual octahedral geometry for other compounds. The M–N stretching mode for known bis(en) complexes with two chelating rings appear at 450 cm^{-1}, which is close to the ones in $[Cu(en\text{-}N)(en\text{-}N,N')_2](NO_3)_2$, consistent with this structure also having two chelating rings. Usually, only two major Raman peaks can be located within

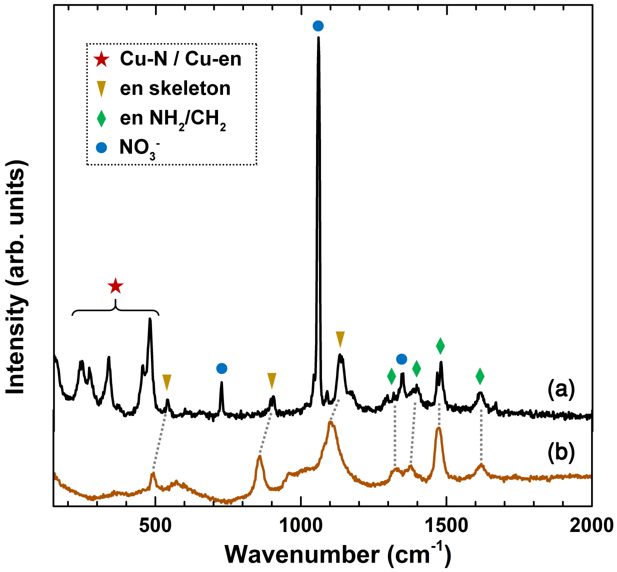

Figure 5.6: Raman spectra of (a) [Cu(en-N)(en-N,N')$_2$](NO_3)$_2$ crystal and (b) liquid en. The Raman spectrum of [Cu(en-N)(en-N,N')$_2$](NO_3)$_2$ contain peaks corresponding to NO_3^-, en (wavenumber shifted compared to liquid en), and the Cu-tris(en) penta-coordination.

this wavenumber region for metal-en coordination, but five are identified here. This may be attributed to unique 5-coordination, making the Cu(II) center lack point symmetry. Although more precise assignment of the Raman modes for [Cu(en-N)(en-N,N')$_2$](NO_3)$_2$ was not made, Fig. 5.6 foretells which Raman spectral features can be expected from species having similar stereochemistry.

The UV-Vis-NIR spectrum of [Cu(en-N)(en-N,N')$_2$](NO_3)$_2$ is presented in Fig. 5.7. It has a broad visible light absorption peaked at *ca.* 555 nm and extends to the NIR region. The absorption maximum correlates with the first coordination sphere in the complex. [144] The 555 nm absorption maximum for our 5-coordinated [Cu(en-N)(en-N,N')$_2$](NO_3)$_2$ is in between the 514 nm seen in [Cu(en)$_2$]$^{2+}$ and 609 nm in [Cu(en)$_3$]$^{2+}$. [144,145] A second smaller peak maximum in the NIR at 914 nm can be identified for [Cu(en-N)(en-N,N')$_2$](NO_3)$_2$ as well. This Vis-NIR spectrum agrees with the one observed in the square-pyramidal penta-ammine compound K[Cu(NH_3)$_5$][PF_6]$_3$, which has a primary peak maximum at 654 nm and a secondary one at 909 nm. [120] Based on molecular-orbital analysis using extended-Hückel

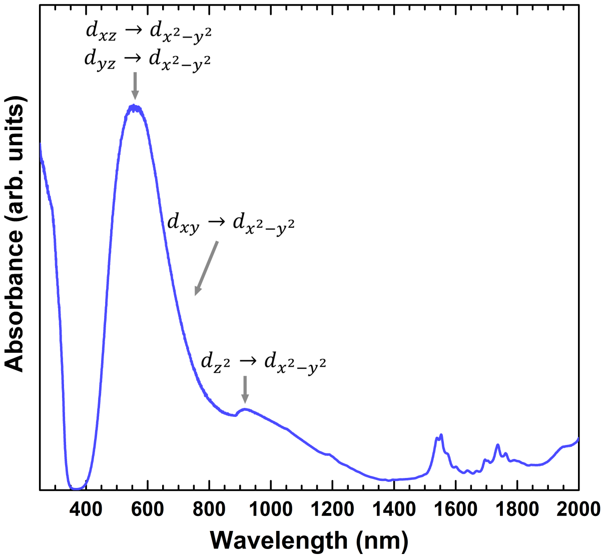

Figure 5.7: UV-Vis-NIR spectrum of [Cu(en-N)(en-N,N')$_2$](NO$_3$)$_2$ crystals. The strong visible absorption peak at 555 nm with the NIR shoulder at 914 nm is consistent with square-pyramidal-based Cu-amine coordination.

calculations, Duggan *et al.* showed that for square-pyramidal [Cu(NH$_3$)$_5$]$^{2+}$, the primary visible absorption was due to $d_{xz}, d_{yz} \to d_{x^2-y^2}$ transitions, the secondary NIR absorption was due to $d_{z^2} \to d_{x^2-y^2}$ transitions, and there was a weak band due to $d_{xy} \to d_{x^2-y^2}$ at 714 nm which could be resolved from the primary peak with Gaussian analysis. [120, 146] The same electronic transition assignment can be adopted for [Cu(en-N)(en-N,N')$_2$](NO$_3$)$_2$ (Fig. 5.7) due to the close resemblance in Vis-NIR spectra and stereochemistry. However, Cu(II) in [Cu(NH$_3$)$_5$]$^{2+}$ exhibits C_{2v} symmetry, whereas the Cu in [Cu(en-N)(en-N,N')$_2$]$^{2+}$ is at a general C_1 position. Therefore the degeneracy between d_{xz} and d_{yz} is expected to be lifted for our complex. Nevertheless, the energy separation between these two levels is small, with no readily-observable features (Fig. 5.7). Discussions on Cu(II) electronic levels based on crystal field theory are more prevalent, [139, 147, 148] but are less applicable due to the lack of symmetry in our complex.

The magnetic susceptibility measurement of [Cu(en-N)(en-N,N')$_2$](NO$_3$)$_2$ is shown in Fig. 5.8. It showed paramagnetic behavior at all measured temperatures which follows Curie's Law. The perfect overlap between zero-field-cooled and field-cooled curves demon-

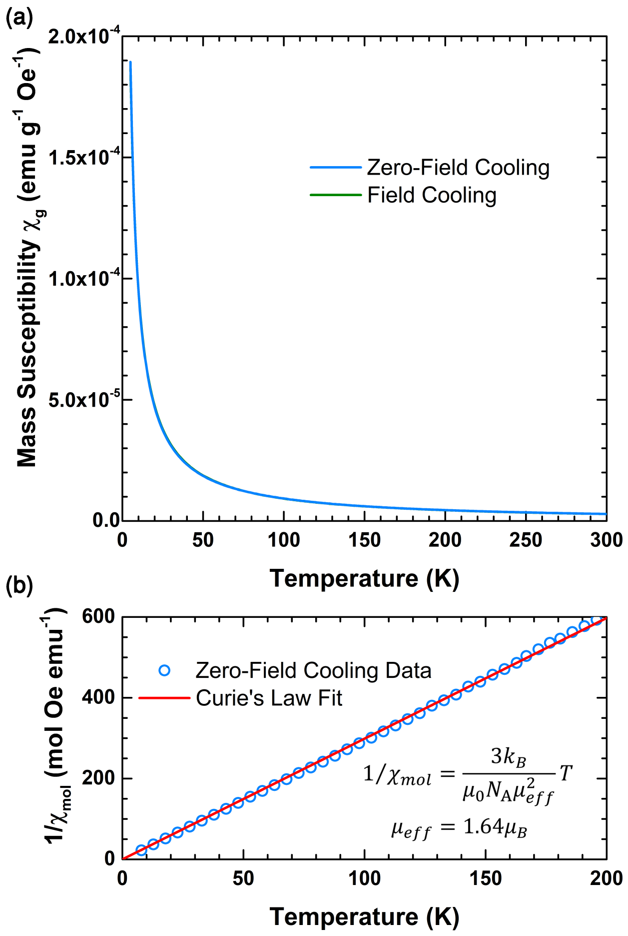

Figure 5.8: (a) Temperature dependence of the magnetic susceptibility of [Cu(en-N)(en-N,N')$_2$](NO$_3$)$_2$ crystals under zero-field cooling and field cooling, which overlap each other. (b) Fitting of the zero-field cooling data to Curie's Law over the temperature range of 5–200 K. This crystal is a paramagnet, with an estimate of 1.64 μ_B effective moment per Cu(II).

strates no remnant magnetization in this compound. Paramagnetism is expected in this structure since the magnetic Cu(II) ions are far from each other (closest Cu–Cu distance is 6.83 Å).

Based on the Curie constant derived from linear regression of the data over the temperature range of 5–200 K, the effective moment for the magnetic center was calculated to be 1.64 Bohr magnetron (μ_B). Because of expected solvent molecules being adsorbed onto the crystal, the measured sample mass should be an overestimate. Therefore the calculated 1.64 μ_B is a low bound for the effective moment per Cu(II) center, consistent with the theoretical effective moment of 1.73 μ_B for a pure spin-1/2 system.

5.4 Conclusions

A new coordination crystal $[Cu(en\text{-}N)(en\text{-}N,N')_2](NO_3)_2$ is presented. Its Cu(II) ions are penta-coordinated to two chelating and one monodentate en ligands. The coordination structure of this crystal is particularly unique in the following ways. (1) It is the first crystal with penta-coordination containing monodentate en using exclusively en ligands. (2) It is the first crystal with Cu coordinated to a monodentate en ligand. (3) It has severe trigonal distortion to the basal square pyramidal stereochemistry. (4) It is an uncommon racemate Cu crystal with $\delta\delta$ (and $\lambda\lambda$) en chelate ring conformations. (5) Its non-coordinating en amine N is not protonated but H-bonded to chelating amine H atom in the adjacent complex. (6) It realizes the penta-ammine effect with only bi-amine ligands. The unique coordination chemistry of $[Cu(en\text{-}N)(en\text{-}N,N')_2](NO_3)_2$ is corroborated by spectroscopic analysis. Magnetic susceptibility indicates that it is a S=1/2 paramagnet. We speculate that the formation of this complex crystal occurs when the effective en concentration is too high to permit $[Cu(en)_2]^{2+}$ crystal formation but too low to stabilize octahedral $[Cu(en)_3]^{2+}$ in solution.

CHAPTER 6

CRITICAL FACTORS LEADING TO SOLID STATE Fe_2SiS_4 FORMATION REVEALED BY *IN SITU* XRD

In the following chapters of the dissertation, I will focus on the generic solid state synthesis method where the starting precursor is a mixture of solid phases. It is one of the easiest and most widely used methods for the production of multi-element ceramic materials. However, although this method is traditional and effective, less is truly understood about the detailed events during reaction. I selected to investigate into this method because of the vast material systems suitable for solid state synthesis. These imply that the extracted thermodynamic and kinetic information from one target system can be easily exported to other systems. The ultimate goal is to synthesize inorganic materials more efficiently with solid state methods, and find high throughput methods to discover new materials.

6.1 Introduction

Efficient synthetic exploration of unknown chemical spaces is a crucial capability in the discovery of structures that exhibit improved functionality or exotic properties. [8, 10, 149] In particular, tremendous effort continues to focus on dense inorganic crystals, which address fundamental questions in condensed matter physics [150–152] and have established applications in electronics, [153] telecommunication, [154] energy, [155, 156] and spintronics, [157,158] *etc.* Despite the development of novel synthesis methods (*e.g.* sol-gel, [159,160] solvothermal, [84, 85, 161] colloidal method, [162, 163] flux method, [164, 165] thin film technology, [166] *etc.*), the conventional solid-state method remains widely used for synthesis of complex inorganic compounds, especially non-oxides, due its versatility. [31, 32, 156] However, the post-mortem examination of most solid state chemistry procedures overlooks the intermediate reaction stages. The lack of available kinetic information in such reactions can preclude the discovery of critical events that determine the fate of synthetic reactions, even in “simple” systems without additives, fluxes, or catalysts.

Solid-state synthesis from individual elements should follow a relatively predictable drop in overall free energy and has been widely adopted in the synthesis of ternary or higher-order chalcogenides. For example, the solar absorber $Cu_2ZnSnSe_4$, [33] thermoelectric $Pb_{1-x}Na_xTe$–$Pb_{1-x}Na_xS$, [34] and superconductor $FeSe_{1-x}Te_x$, [35] *etc.* were prepared using elemental powders. However, this thermodynamic approach does not concern itself with kinetic barriers in any detail.

Via unconventional kinetically-defined intermediate states, synthetic control can be achieved by directing reactions into alternate chemical spaces. Such methods are very mature in organic chemistry, where molecules can be designed and fabricated in a stepwise manner. [167–170] Comparatively, kinetic manipulation in inorganic crystal synthesis is less advanced. Recent developments in this field include the use of salts (MCl_2 + Na_2S_2 or Na_2Se_2), where metathesis reaction allows for low temperature materials design. [171, 172] With considerable emphasis on high-throughput materials design and structure prediction, [8, 10, 13, 173, 174] improved synthetic control and understanding of the critical factors determining inorganic crystal formation has become increasingly valuable.

In this study, we deployed *in situ* X-ray diffraction (XRD) to examine the formation of the model compound Fe_2SiS_4. Iron-based semiconducting sulfides such as pyrite FeS_2 have been considered as candidate photovoltaic absorbers, but have been plagued by poor transport due to defects and non-stoichiometry. [175, 176] Through density functional theory calculations, Yu *et al.* demonstrated that with the inclusion of Si, the resultant Fe-Si-S ternary compound will have stable FeS_6 coordination and Fe^{2+} valence, with a reasonable band structure and fewer defects. [177] Fe_2SiS_4 with the olivine structure (Fig. 6.1(a)) is the only known ternary Fe-Si-S compound. The reported synthesis conditions of Fe_2SiS_4 have been temperature

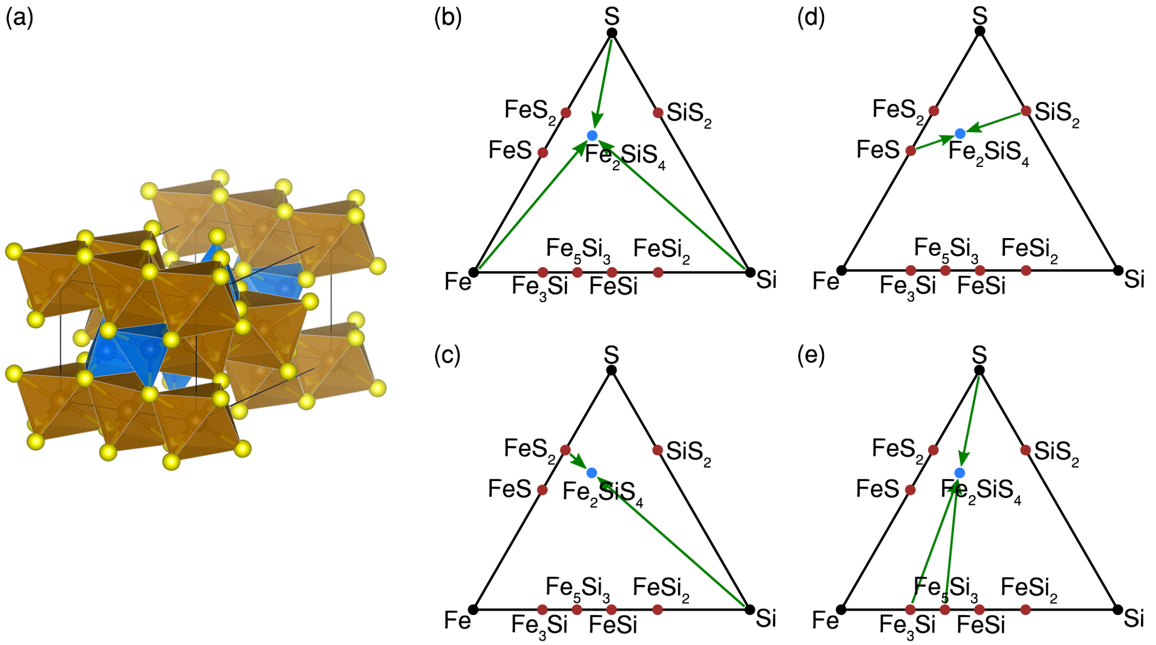

Figure 6.1: (a) Crystal structure of olivine Fe_2SiS_4. Brown octahedra: FeS_6; blue tetrahedra: SiS_4; yellow spheres: S. (b-e) The approaches undertaken in this study in reaching the same equilibrium state via examining different reaction pathways. Sulfidation kinetics, invariant points, and atomic mixing led the system to experience different intermediates and products.

demanding (> 700 °C, quite high for sulfides), and the formation mechanisms and physical properties of Fe_2SiS_4 have barely been investigated. [178–180]

Utilizing *in situ* XRD, we surveyed the disparate progression of phases formed by reagents with the same overall stoichiometry but different bonding within. Kinetic factors expediting Fe_2SiS_4 crystal formation were revealed by *in situ* reaction progress maps. Four different reaction schemes were chosen in this study (Fig. 6.1(b-e)). The replacement of elements by binary compounds serves to direct the system through alternate intermediate states, which have profound kinetic consequences. Divergent behaviors were seen for the different schemes. Ultimately, the goal is to produce a ternary phase (Fe_2SiS_4 here) quickly and at low temperature. To that end, we noted kinetic acceleration via peritectic liquid generation from FeS_2, and more facile Si-S bond formation achieved by first breaking Si-Si bonds to form Fe-Si silicides. The failure of the conventional practice (elemental reaction) to produce the thermodynamic product without excessive heating is also demonstrated. The methods and mechanisms in this study can be applied to other inorganic systems to facilitate crystal formation and discover new materials.

6.2 Synthesis and Characterization

All powder manipulations were performed in an Ar-filled glovebox. All powder mixtures were mixed and ground prior to heat treatment.

FeS, FeS_2, SiS_2 and iron silicides were synthesized in evacuated fused silica ampoules, with heating rates of 10 °C/min, and cooling rates not faster than -10 °C/min unless specified. FeS was synthesized with an equimolar mixture of Fe and S, heating at 600 °C for 24 h. FeS_2 was synthesized with Fe and S mixture in 1:3 molar ratio, heating at 400 °C, 500 °C for 3 h each, and then at 600 °C for 24 h, forming an FeS_2 and S mixture. Sulfur was sublimed out of this sample using a temperature gradient treatment, with the bottom of the ampoule placed inside box furnace heated to 400 °C for 6 h, while the ampoule top remained outside of the furnace near room temperature. After cooling, the powder at the ampoule bottom was retrieved and the sublimation was repeated to yield pure FeS_2 powder. SiS_2 was synthesized with Si and S mixture in 2:5 molar ratio, heating at 400 °C, 500 °C for 3 h each, and then at 600 °C for 66 h, forming SiS_2 and S mixture. The same sublimation process described above was performed to remove excess S and produce pure SiS_2. Iron silicides (with 2:1 Fe:Si molar ratio) were prepared via stoichiometric Fe and Si mixtures heated to 1050 °C for 24 h. Fe_3Si, FeSi, and Fe_5Si_3 were synthesized by mixing stoichiometric amount of Fe and S, pressed into pellets, and reacted at 1050 °C for 24 h. FeSi used a cooling rate not faster than -5 °C/min. Fe_5Si_3 underwent a second cycle of pelletizing and heat treatment with the same conditions and was finally cooled by water quenching. In the test with ball milling, Fe and Si in the stoichiometric ratio were placed inside a SPEX SamplePrep 8001 hardened steel grinding vial and ball milled with one 3/8 inch and three 1/2 inch hardened steel balls for

1 h in SPEX SamplePrep 8000D Mixer/Mill. Stoichiometric amount of S was added to the ball-milled Fe and Si mixture and ground with mortar and pestle before further synthesis.

Reagents used for *in situ* XRD syntheses were prepared by placing stoichiometric powder mixtures inside 0.7 mm-diameter fused silica capillaries. Capillaries were sealed under vacuum and then fixed inside 1.0 mm diameter fused silica capillaries. *In situ* XRD reactions were performed by heating from room temperature at 1 °C/min to 800 °C, holding at 800 °C for 4 h, and then cooling at -1 °C/min to room temperature.

As with the preliminary binary reactions above, all *ex situ* reactions of Fe_2SiS_4 were performed in fused silica ampoules sealed under vacuum. The maximum temperature and duration of heating are specified in the discussion section for each sample. All heating rates were 1 °C/min (to match the *in situ* procedure) and cooling rates were not faster than -10 °C/min. If a second heat treatment cycle is specified, then the retrieved sample from the first cycle was reground, sealed under vacuum, and heat treated for a second time with the same procedure. Materials for SEM-EDS mapping analysis were prepared *ex situ* by heating to the specified temperatures, and then quenched in water.

Powder XRD data were collected on a Bruker D8 ADVANCE diffractometer equipped with Mo K_α source and LYNXEYE XE detector in transmission geometry. *In situ* XRD reactions utilized a home-built anti-scatter slit system and a synchronized TC-Transmission furnace with polyimide windows. A 2θ range of 4-30° was used with a scan speed of 1° min^{-1}. This translates to a temperature span of 26 °C for a single XRD pattern during heating and cooling. Quantitative Rietveld refinements to the XRD data were performed using the Bruker TOPAS 5 suite. Because fast *in situ* XRD acquisition limits the collection of very high-angle peaks, atomic displacement parameters B were fixed to 1 and the stoichiometry of pyrrhotite $Fe_{1-x}S$ was fixed to $Fe_{0.875}S$ in all refinements. The Rietveld results were used to construct *in situ* reaction progress maps, where the “amount” specified is proportional to the total number of atoms contained in each phase. Normalization is performed by dividing by the total number of Fe and Si atoms present in all phases in the respective XRD pattern. Because of the complex polymorphic transformations of elemental S and its absence from the normalization equation, we display all reaction progress maps from 156 °C onwards. No changes in Fe- or Si-containing phases are seen below this temperature. Scanning electron microscopy (SEM) with energy dispersive X-ray spectroscopy (EDS) mapping were performed with a JEOL JSM-6060LV microscope at 30 kV accelerating voltage. The SEM samples were placed on carbon tape and sputter-coated with Au/Pd. Crystal structures were visualized using VESTA. [88]

6.3 Results and Discussion

6.3.1 *In situ* identification of peritectic liquid S initiating Fe_2SiS_4 crystal formation

The *in situ* reaction progress map for Fe_2SiS_4 synthesis at 800 °C was first obtained for the traditional reaction from the pure elements (Fig. 6.1(b)). It is clear from the map in Fig. 6.2(a) that this elemental scheme produces a distinct, rapid onset of Fe_2SiS_4 at around 743 °C.

Fig. 6.2(a) reveals that, prior to Fe_2SiS_4 formation, Si remained nonreactive and all changes involved the interaction of Fe and S, which can be tracked on the Fe–S binary phase diagram in Fig. 6.3, which is well-studied. [181] Upon heating to the temperature range of 276 °C to 443 °C, S reacted with Fe to form FeS_2 and $Fe_{1-x}S$ until the depletion of available elemental Fe. These processes correspond to the red arrows in Fig. 6.3. Further heating led to the invariant point at 743 °C. This is a peritectic point, where FeS_2 decomposes incongruently into $Fe_{1-x}S$ and elemental S (green arrows in Fig. 6.3). The peritectic decomposition of FeS_2 is clearly captured in our *in situ* reaction map as the FeS_2 amount dropped to zero with a concurrent burst in $Fe_{1-x}S$ content. The peritectic reaction must also produced a large amount of S liquid at this time (Fig. 6.3).

Before the peritectic decomposition of FeS_2, we expect the reaction mixture to have only

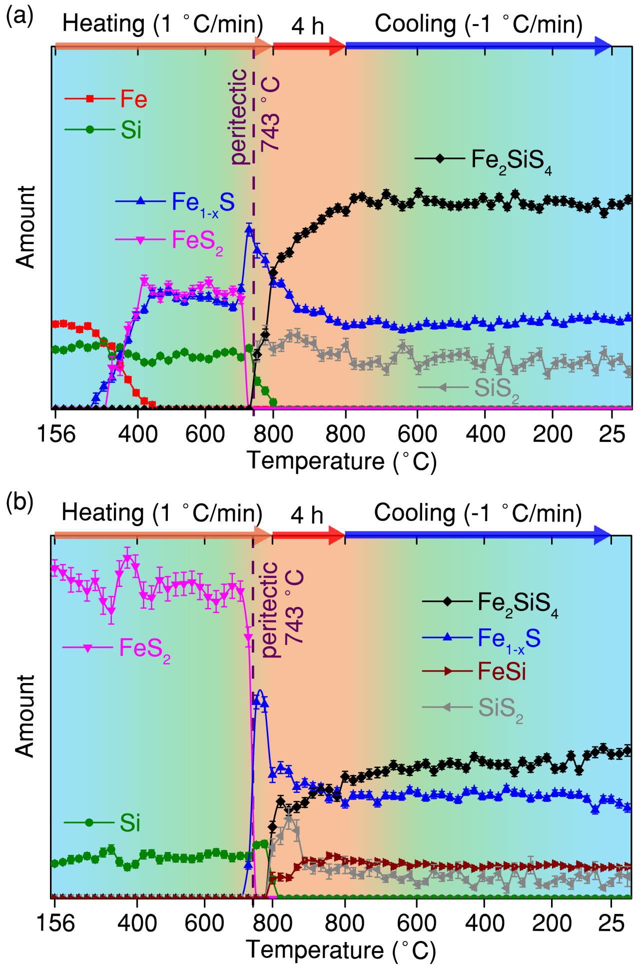

Figure 6.2: Reaction progress maps constructed from *in situ* XRD for the reaction schemes (a) 2 Fe + Si + 4 S and (b) 2 FeS_2 + Si. The appearance of peritectic liquid S (from FeS_2 decomposition) initiated fast Fe_2SiS_4 crystal formation.

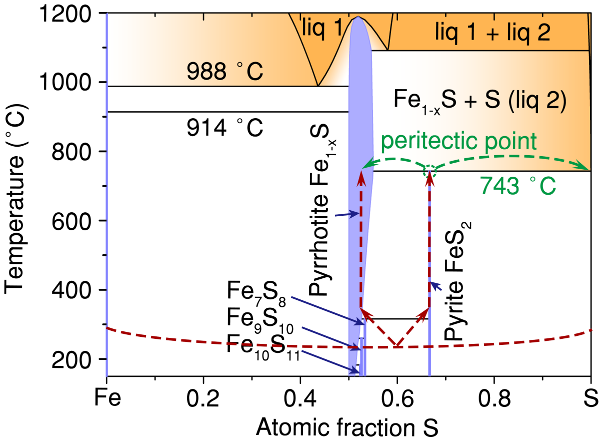

Figure 6.3: Binary phase diagram of Fe–S. The arrows indicate the progression in the Fe-S phase space during early stages for the reaction 2 Fe + Si + 4 S until the peritectic decomposition of FeS_2.

contained a scarce amount of elemental S. No sulfidation was occurring, as evidenced by the lack of consumption of Si or $Fe_{1-x}S$.

The peritectic decomposition of FeS_2 at 743 °C released a sudden burst of elemental S, which exceeded the equilibrium S vapor pressure at that temperature. Thus superheated liquid S must formed, which wetted and immersed the other reaction components. The surge of available high mobility, high reactivity S liquid led to the consumption of $Fe_{1-x}S$ and Si, and the onset of SiS_2 and Fe_2SiS_4 formation (Fig. 6.2(a)). The peritectic FeS_2 decomposition not only initiated Fe_2SiS_4 formation, but also ushered in fast kinetics, as seen from the sharp upward rise in Fe_2SiS_4 content between the peritectic at 743 °C and the maximum temperature of 800 °C.

The proportion of Fe_2SiS_4 continued to increase during the maximum 800°C hold time of this *in situ* XRD investigation. Fe_2SiS_4 (and other phases) did not display any prominent changes during slow cooling, indicating that Fe_2SiS_4 is fairly stable once formed.

This scheme where the FeS_2 peritectic initiates the growth of Fe_2SiS_4 was investigated more directly by a second reaction where Fe and S were pre-reacted to first form FeS_2, which was subsequently reacted with Si (Fig. 6.1(c)). *In situ* reaction progress maps for this 2 FeS_2 + Si reaction are displayed in Fig. 6.2(b). Before the peritectic temperature of 743 °C, FeS_2 and Si remained nonreactive. The instantaneous decomposition of FeS_2 and burst of $Fe_{1-x}S$ + S at 743 °C is clear in Fig. 6.2(b). Fast kinetics between $Fe_{1-x}S$, Si and S took place, with Fe_2SiS_4 being the major product formed.

We credit the burst of highly reactive peritectic liquid S to be responsible for the rapid formation of Fe_2SiS_4. A similar observation was found in Sato *et al.*'s work, where the formation of Ti-Si eutectic liquid was postulated to be critical to drive enhanced formation of Ti_3SiC_2. [182, 183] Intentional addition of molten salt fluxes has proven useful in other systems, [149, 164, 184–186] but the power of self-generating invariant liquid seen here has been under-investigated and under-utilized in promoting complex crystal formation. Here, through *in situ* XRD, we provide direct evidence on the role of a peritectic liquid in expediting inorganic crystal creation.

6.3.2 *In situ* identification of low temperature Fe_2SiS_4 crystal formation by directed intermediate reactions

From the previous reactions, the question arises whether Fe_2SiS_4 is thermodynamically stable in the presence of FeS_2, and if so, can it be formed at lower temperatures than 743 °C? In fact, kinetics barriers were present in the reaction schemes of Fig. 6.1(b,c). Specifically, scrutiny of the reaction progress maps shows that Si did not participate in any reaction until FeS_2 decomposed. Clearly, there is a great disparity between the kinetic affinity of Fe and Si sulfidation — Si remained in its elemental state while Fe became fully sulfidized. Only the superheated (>743°C) S liquid from the FeS_2 peritectic drove a reaction with elemental Si.

Two methods were applied to sidestep the sluggish reaction kinetics of elemental Si. In one scheme, Si was reacted with S first to form SiS_2, which then reacted with FeS (Fig. 6.1(d)). In the other scheme, Si was reacted with Fe first to form iron silicides, which were then sulfidized (Fig. 6.1(e)). Both schemes are stoichiometric and succeeded in initiating Fe_2SiS_4 generation at lower temperatures than the FeS_2 peritectic.

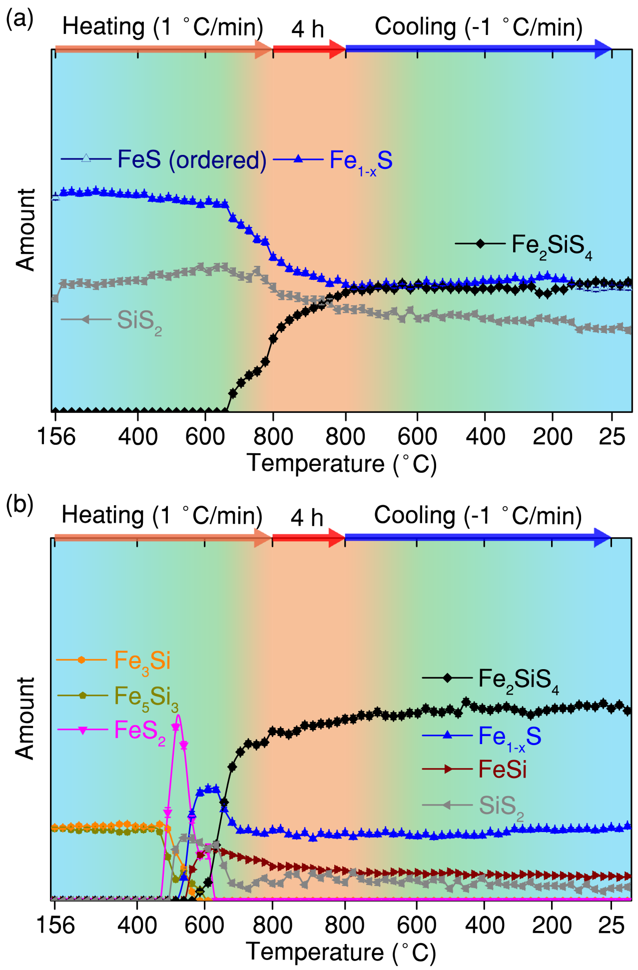

Figure 6.4: Reaction progress maps constructed from *in situ* XRD for the reaction schemes (a) 2 FeS + SiS_2 and (b) Fe_5Si_3 + Fe_3Si + 16 S. Both reactions eschewed elemental Si as a reagent and allowed the system to form the ternary phase at lower temperature.

The reaction progress map in which both Si and Fe were pre-bonded to S (SiS_2 and FeS in 1:2 molar ratio) is displayed in Fig. 6.4(a). The progress of this reaction was found to proceed in a very different and simple fashion: a slow reaction of $Fe_{1-x}S$ and SiS_2 making Fe_2SiS_4 took place. It is clear from Fig. 6.4(a) that Fe_2SiS_4 can be formed without the involvement of peritectic liquid S. Moreover, Fe_2SiS_4 started to form at 682 °C, which is lower than the peritectic temperature of 743 °C.

The silicide reaction progress map is shown in Fig. 6.4(b). The iron silicides used were a mixture of Fe_3Si and Fe_5Si_3, with an overall stoichiometry of 2:1 Fe:Si. In this scheme,

Fe_2SiS_4 started to form at 586 °C, which is the lowest of all reaction schemes we have investigated.

Comparison between Fig. 6.2(a) and Fig. 6.4(b) reveals that the sulfidation proceeded very differently in these two systems. In the native elemental Fe + Si + S reaction (Fig. 6.2(a)), only iron sulfides formed while Si remained inactive. However, when iron silicides were reacted with S, the formation of both iron sulfides and silicon disulfide began at 491 °C. This implies the kinetic barrier on Si sulfidation was lowered when Si was presented as a product of iron silicide dealloying, despite the driving force for the reaction being reduced. The result of iron silicide sulfidation was the early presence of fine-grained $Fe_{1-x}S$ and SiS_2, combined to form ternary Fe_2SiS_4 at a lower temperature (586 °C).

Use of iron silicides as a reagent led to consistently low onset temperatures for Fe_2SiS_4 formation regardless of the specific silicide phases used. We performed *in situ* XRD investigation on reactions of Fe_3Si + 5S, Fe_5Si_3 + 11S, and FeSi + 3S. While these reactions did not have the 2:1 Fe:Si ratio to form phase-pure Fe_2SiS_4, they nevertheless consistently formed Fe_2SiS_4 with onset around 586 °C. Therefore, pre-reaction of Si with Fe is a generally applicable method to direct the reaction progress to lower the required thermal energy for the formation of the ternary Fe_2SiS_4.

To further demonstrate the benefit of using iron silicides in producing Fe_2SiS_4 at low temperatures, we conducted *ex situ* reactions at 550 °C (consisted of two 48-hour cycles with powder remixing in between). The chosen temperature of 550 °C is slightly lower than the *in situ* observed onset temperature of 586 °C. This is because any induction period for *ex situ* growth is manifested as an increase in apparent reaction onset during the continuously-heated *in situ* process. Therefore, a small overheating is generally required for *in situ* observation of slow reactions. Fig. 6.5 clearly displays the contrast in end product between the reaction schemes of 2 Fe + Si + 4 S and Fe_5Si_3 + Fe_3Si + 16 S. Following the conventional route of elemental reaction, no trace of Fe_2SiS_4 could be produced (Fig. 6.5(a)). However, when the reaction was driven to proceed via iron silicide sulfidation, Fe_2SiS_4 became the major

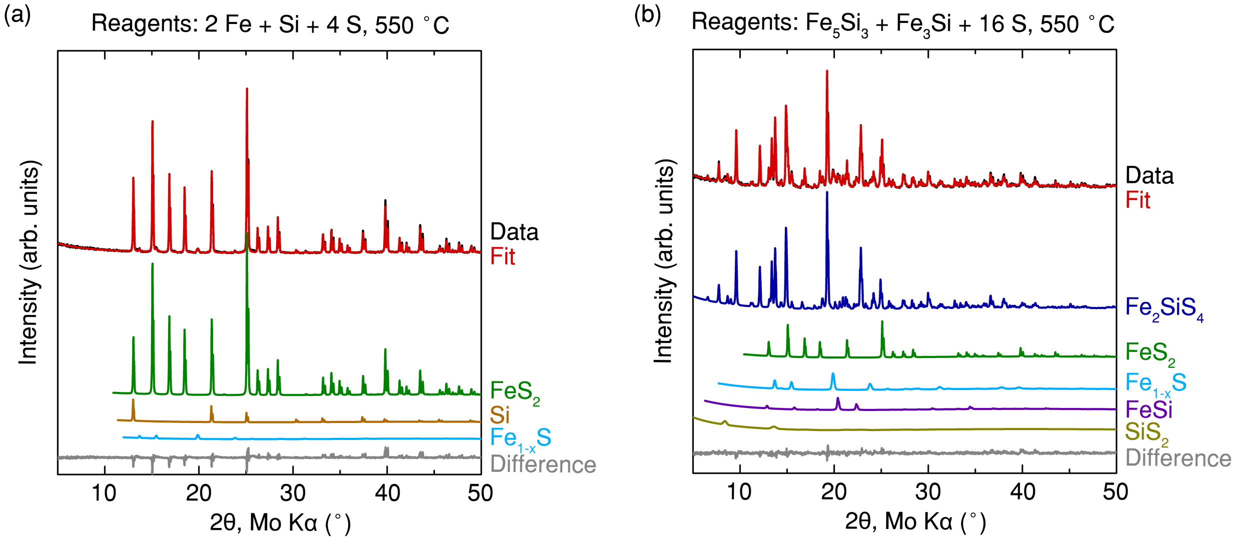

Figure 6.5: Rietveld refinements showing the products at the end of a 96 h heat treatment at 550 °C for the reactions of (a) 2 Fe + Si + 4 S and (b) Fe_5Si_3 + Fe_3Si + 16 S. The sulfidation of iron silicides produced large quantities of Fe_2SiS_4, whereas reactions of the elements failed (yielding only binaries).

product at 550 °C (Fig. 6.5(b)). To the best of our knowledge, with early literature typically using close to or more than 800 °C, [178–180] this is the lowest reported temperature of Fe_2SiS_4 formation.

The failure of the elemental reaction to produce the stable ternary chalcogenide (Fe_2SiS_4 in this case) at low temperature can be seen as a warning signal. Without the addition of non-stoichiometric flux or additives, the direct elemental route to complex materials must have the largest thermodynamic driving force. The system will minimize its free energy, but only by routes that are kinetically accessible. Separation of cations, such as Fe and Si here, in early stages of the reaction may block a route to reach the thermodynamic equilibrium. Using Fe_2SiS_4 as a model example, one may mistakenly conclude that Fe_2SiS_4 is not an equilibrium phase, or worse, is non-existent, if their maximum synthesis temperature is below 743°C (a quite high temperature for sulfur in a sealed tube). Without the efforts to engineer the progress of reactions, one may also miss the opportunity to discover metastable compounds that decompose at higher temperatures.

6.3.3 Factors contributing to expedited Fe_2SiS_4 formation at low temperatures

Expedited formation of Fe_2SiS_4 below the FeS_2 peritectic temperature was achieved when iron silicides were used as the reactants, likely due to two factors: the kinetic effects that limit reactions based on intrinsic diffusion, and the degree of contact in the microstructure developed from the reagents.

Understanding these kinetics at the outset of a synthetic procedure is actually practical. Metal corrosion is well-studied, and metal sulfidation rates are confirmed to be fast compared to oxidation due to the higher degree of non-stoichiometry and larger defect mobility in sulfides. [187, 188] Fe is the classic example of a metal prone to sulfidation corrosion, where the sulfide scales form by vacancy-enhanced Fe solid-state diffusion, with kinetics well-described by Wagner's theory. [189, 190] Its sulfidation kinetics are on the fast end among common metals and its sulfide ($Fe_{1-x}S$) has one of the largest non-stoichiometry ranges (Fig. 6.3). [191,192] These vacancies in pyrrhotite $Fe_{1-x}S$ are one major cause of the disparity in sulfidation kinetics between Fe and Si. SiS_2 has not been reported to contain extensive point defects leading to non-stoichiometry, and is presumably a line compound. For this reason, slow sulfidation kinetics of crystalline Si may be expected. In fact, Si alloying has been reported to enhance sulfidation resistance at high temperature. [193] In essence, our elemental 2 Fe + Si + 4 S reaction began with fast Fe sulfidation, but its effectiveness in forming stable Fe_2SiS_4 crystals was hampered by slow Si sulfidation until high-activity superheated liquid S appeared.

With iron silicides, fast Fe sulfidation kinetics in turn accelerated the formation of SiS_2, since the dealloying of iron silicide left defective Si network that was more favorable to form SiS_2 rather than crystalline Si. This formation of intimately contacting binary sulfides in turn expedited their final transformation into Fe_2SiS_4.

The second factor that expedites Fe_2SiS_4 formation from iron silicides is increased physical mixing, which can be viewed through micrographs of quenched samples. Manual grinding or

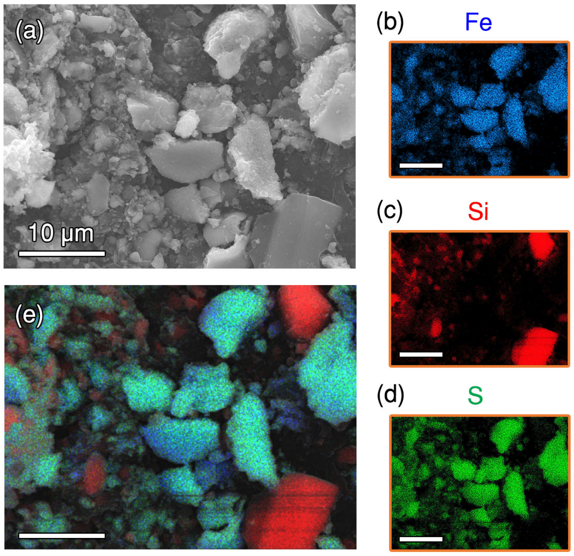

Figure 6.6: SEM EDS maps of the product from the reaction 2 Fe + Si + 4 S quenched at 550 °C: (a) SEI image, (b) Fe, (c) Si, and (d) S EDS distributions. The overlay of the SEI and Fe, Si, S EDS signals is displayed in (e). All scale bars are 10 μm. The sample consisted of FeS_2, $Fe_{1-x}S$, and Si. Significant spatial segregation among iron sulfides and Si crystals is apparent.

ball-milling are limited in size-reduction to the scale of microns, while higher-energy techniques typically have the disadvantages of limited chemical compatibility or the introduction of impurities. Without sufficient phase homogenization, segregation can lead to lack of contact between particles, which may prevent the effectiveness of reaction. An example of such spatial segregation is shown in Fig. 6.6, which depicts the state during the reaction between Fe, Si and S elements quenched from 550 °C. A clear separation is seen in the SEM-EDS mappings: Si grains (red) were separated from the blue-green Fe–S grains (blue for Fe and green for S). The sulfidation of Fe did not fragment the initial Fe particles into much smaller pieces. The segregation among iron sulfides and Si resulted in poor contact between them, which prevented the formation of Fe_2SiS_4 at low temperatures.

In contrast, the reaction between iron silicides and S maintained an intimate level of mixing between Fe and Si throughout. When sulfidation of the atomically-mixed iron silicides commenced, Fe and Si were first separated to form binary sulfides rather than the ternary directly. The aforementioned high defect concentration of Fe-sulfides is likely the root of

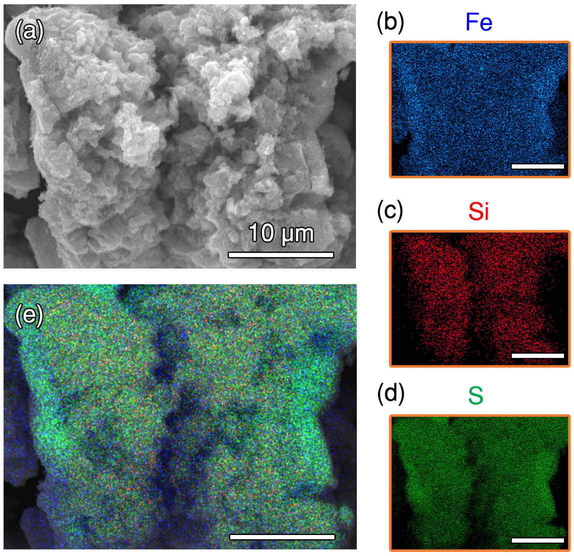

Figure 6.7: SEM EDS maps of the product from the reaction Fe_5Si_3 + Fe_3Si + 16 S quenched from 520°C: (a) SEI image, (b) Fe, (c) Si, and (d) S EDS distributions. The overlay of the SEI and Fe, Si, S EDS signals is displayed in (e). All scale bars are 10 μm. The reduced Si signal at the sample periphery is an artifact caused by the geometric arrangement of the sample and detector. The sample consisted of FeS_2, $Fe_{1-x}S$, SiS_2, and FeSi phases, mixed at the nanoscale even after dealloying of the silicides due to sulfidation.

this behavior. Nevertheless, the resultant binary sulfides remained mixed on the nanometer scale. This is seen in Fig. 6.7, where the materials were quenched from 520 °C. In contrast to Fig. 6.6, even at a lower temperature, the three elements in Fig. 6.7 were found to be distributed uniformly within the resolution limit of the technique. This level of mixing is not practically achievable by mechanical means. In addition, the particles after sulfidation were found to be porous and contained fine grains (Fig. 6.7(a)). The evolution of such porous structure is expected to arise from the kinetic competition between sulfidation and surface diffusion, similar to the well-studied phenomenon of nanoporosity evolution during dealloying. [194, 195] The finer microstructure and pervasive mixing during iron silicides sulfidation provides a distinct advantage in expediting ternary Fe_2SiS_4 formation.

6.3.4 *In situ* identification on the effect of particle size reduction on Fe_2SiS_4 formation

Apart from devising alternate reaction pathways by controlling the order in which the initial precursors Fe, Si, and S react, another way to accelerate the formation of Fe_2SiS_4 is to modify the physical characteristics of the reagents. Particle size has long been known to have significant effects on the rate of solid state reactions. [196] Smaller particle size results in larger interface area between different chemicals, which are the reaction fronts. Smaller particle sizes also shorten the diffusion distance that needs to be covered for complete transformation. It is imperative to test if the effectiveness of particle size reduction can free the elemental reaction system from the requirement of peritectics, and if so, how does the effectiveness of particle size reduction compare with that derived from reaction pathway engineering.

We used ball milling as an effective method to reduce the particle sizes of the reagents. Fe and Si were ball milled for 1 hour before mixed with sulfur (2:1:4 Fe:Si:S molar ratio) and packed into a capillary for *in situ* XRD measurement. The effect of ball milling on particle size reduction can be clearly seen from the XRD peak broadening effect (Figure 6.8). Compared with the sample prepared by hand-grinding using mortar and pestle, the sample prepared with ball milling clearly had broader XRD peaks.

The *in situ* reaction progress map for the ball milled sample with elemental precursor mixture is shown in Figure 6.9. It is seen that Fe_2SiS_4 formed at a temperature as low as 539 °C, far below the temperature that peritectic dissociation of FeS_2 is expected. This shows that even for the elements, peritectic dissociation of FeS_2 is not a necessary requirement to form Fe_2SiS_4, as long as the kinetics are fast enough. This ball milled sample had even lower Fe_2SiS_4 onset temperature than the temperature obtained with the previous “optimum” reaction path. Hand-grinding is still the dominant practice to mix reagents in many areas of solid-state research. The large kinetic barriers within these reactions raise concerns about the accuracy of phase diagrams derived from experiments using such practices. The implications of this will be illustrated further in ternary sulfide and selenide systems in Chapter 8.

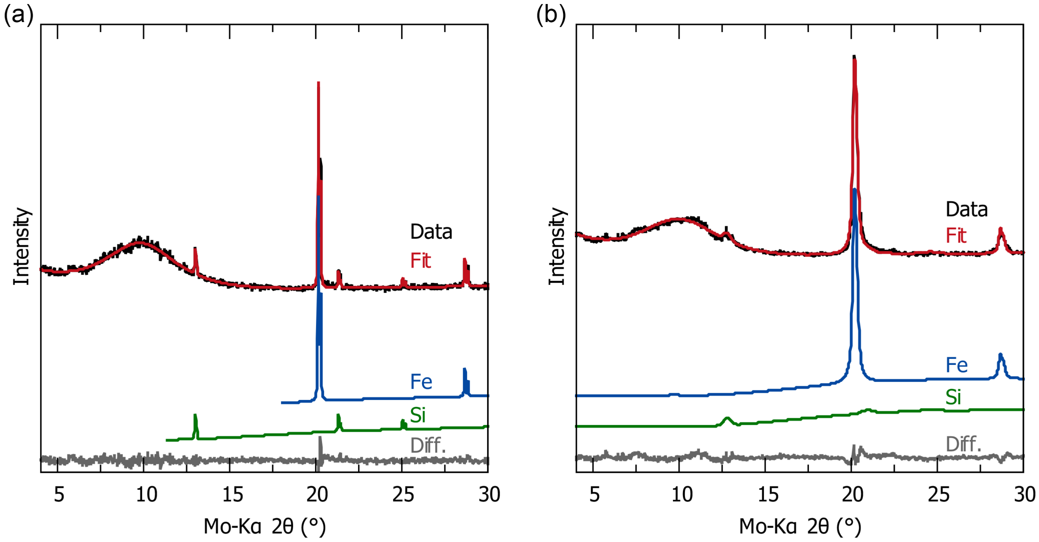

Figure 6.8: XRD patterns for a mixture of 2 Fe + Si + 4 S that were prepared by (a) hand-grind, and (b) ball milling. The ball-milled sample had significant XRD peak broadening due to its small particle sizes.

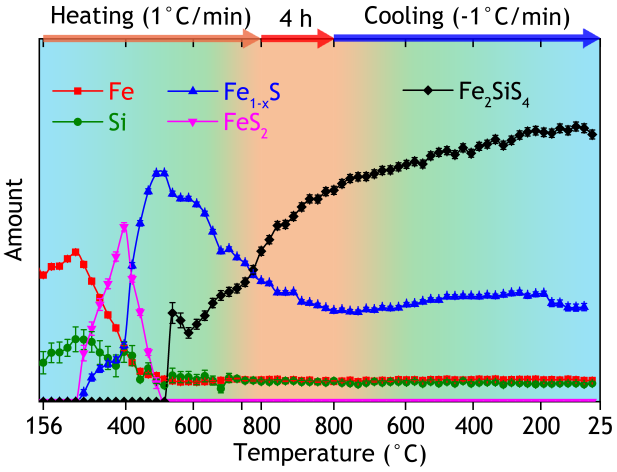

Figure 6.9: Reaction progress map constructed from *in situ* XRD for the reaction 2 Fe + Si + 4 S after ball milling the reagents.

6.4 Conclusions

In situ X-ray diffraction was employed to analyze the progress of reactions leading to the formation of inorganic crystal Fe_2SiS_4. The intermediate reactions were engineered by varying the initial bonding in the precursors. This allows the system to approach the same thermodynamic equilibrium state through different phase space pathways. With detailed reaction progress maps, we identified critical kinetic factors governing the success of exploratory reactions. It was found that if FeS_2 survived until 743 °C, its peritectic decomposition released a burst of superheated S liquid that initiated fast Fe_2SiS_4 formation. It is also shown that by pre-reacting Si with other elements, we can steer the reaction to avoid sluggish states and expedite Fe_2SiS_4 formation. This scheme allows for more effective exploration of complex phase diagrams without involving excessive chalcogen (S) vapor pressure at extreme temperatures. The best outcome was achieved from the sulfidation of iron silicides. This scheme not only offers a smooth transition from iron silicides to binary sulfides and finally to the ternary sulfide, but also developed a microstructure with intimate phase mixing. Ball milling to reduce the particle sizes of the reagents was also confirmed to be a very effective method for Fe_2SiS_4 to form at low temperatures. The kinetic expediting factors identified *in situ* were expected to guide new material discoveries in other inorganic systems.

CHAPTER 7

DISCOVERY OF NEW Ba–Fe–S MATERIALS USING A REACTIVE FLUX

7.1 Introduction

During the *in situ* examination of the formation of Fe_2SiS_4 with elements as the reagents, it was discovered that ternary crystal formation was assisted by the kinetic boost introduced from peritectic dissociation of FeS_2. Crossing this invariant point generated superheated liquid S that greatly enhanced reaction kinetics. The paths toward lower energy configurations at the atomic-scale (*i.e.* bond breaking, formation, structural rearrangement) under such violent conditions might be very different than during milder reactions (*e.g.* between FeS and SiS_2). In a system which has few energy minima in the composition space (*e.g.* the Fe–Si–S system), this violent development probably ends up the same as in a mild reaction. However, this may not be the case for systems with an abundance of local minima that are very close in compositions. The disturbance could result in some particular configurations that are not accessible in normal solid state conditions. An appropriate system to manifest these effects needs to meet two requirements. First, it should have a first-order transition in its sub-system that produces liquid phase with heating. Besides peritectic transformations, melting is another option. This idea is actually the so-called flux synthesis, which has been established as a common method for multi-element material synthesis and growth of large crystals. [149, 164, 184, 197] The second requirement is that they should preferentially have a crowded phase diagram. A crowded phase diagram implies the multi-element system has many known energy minima. This is manifested as different forms of stable materials that were only slightly different in their compositions, geometrical arrangement of their subunits,

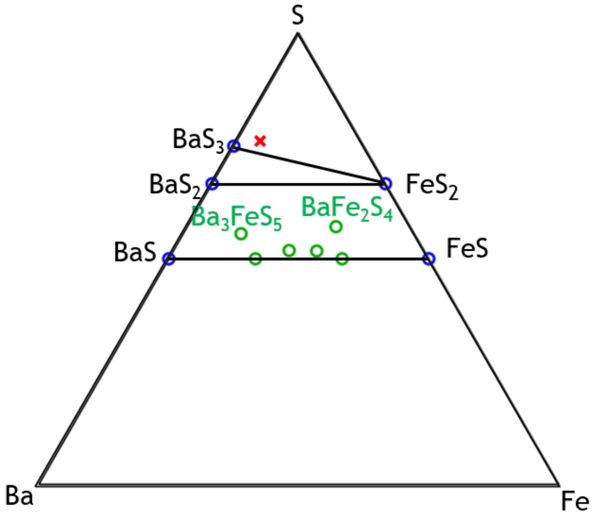

Figure 7.1: Ba–Fe–S composition diagram showing the known binary compounds (open blue circles) and representative known ternary compounds (open green circles). The overall stoichiometry of the reagents used in the *in situ* XRD study is shown with a red cross.

and their formation energies per atom. Therefore there is a higher possibility in the existence of an undiscovered material whose structure is a slight variation from the known ones and whose energy is comparable to the known stable ones. The Ba–Fe–S system is one such system that meets these requirements, which we test for evidence of new material structures using *in situ* XRD.

The Ba–Fe–S system is known to contain a plethora of ternary crystal structures. At lease 17 ternary structure types have been documented, with some representative ones shown in Figure 7.1. [198] Among them include two infinitely adaptive series $\mathrm{Ba}_{1+x}\mathrm{Fe}_2\mathrm{S}_4$ and $\mathrm{Ba}_3\mathrm{Fe}_{1+x}\mathrm{S}_5$. [199–201] Within these infinitely adaptive series are compounds with stacking layers. Any combinations of these layers can be accommodated in these series. Therefore these generate similar but distinct structures whose compositions are very close. A large number of known structure types, together with the existence of infinitely adaptive series, shows that ternary Ba–Fe–S structures are very tolerable to the geometrical reorganization of the sulfide polyhedra, and that the energy difference between distinct structures is not large.

The method of inorganic material crystallization with the utilization of a high-temperature

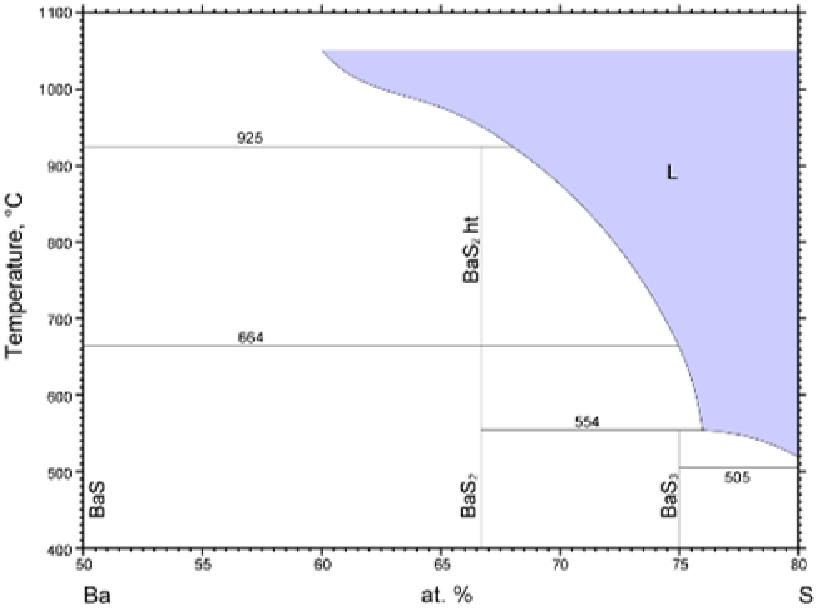

Figure 7.2: Binary Ba–S phase diagram Proposed by H. Okamoto. [202]

melt is termed flux synthesis. [164] It requires the presence of flux-forming species which melt at conveniently low temperatures. The liquid fluxes aid in the diffusion of reactants and enable rapid formation of materials. [149] In the historical use of flux synthesis, fluxes are treated as a medium from which precipitates slowly formed. But with the use of *in situ* XRD, we showed that with reactive flux, the onset of flux formation might already trigger unique events that crystallized inorganic materials immediately.

In our study of Ba–Fe–S system, a reactive flux was used where atoms from the flux were expected to be incorporated into the crystallized materials. The flux chemicals used were a combination of BaS_3 and S. Elemental sulfur melts at a very low temperature (115 °C), but without the dissolution of Ba, its effectiveness as a flux in inducing ternary Ba–Fe–S crystallization is limited. BaS_3 is the real effective flux agent in this case. Based on the binary Ba–S phase diagram proposed by Okamoto *et al.* (Figure 7.2), BaS_3 melts at 554 °C. [202, 203] Some additional amount of S was added to decrease the melting point and increase the total amount of liquid phase.

Most of the known ternary Ba–Fe–S materials were discovered via conventional solid state chemistry using a high reaction temperature ($\geq$ 800 °C). [198] We conducted a series of traditional solid state reactions using BaS, Fe, and S as the reagents with different stoichiometries and reaction temperatures. These *ex situ* tests used sample stoichiometries that did not form fluxes, falling within the composition space bound by BaS–BaS_2–FeS_2–FeS in Figure 7.1. These traditional solid state reactions showed that 600 °C is the approximate temperature that formation of ternary Ba–Fe–S structures are beginning. This is comparable to the flux formation temperature of BaS_3 (554 °C). Thus it is expected that if BaS_3 melts and forms a flux, flux-assisted crystal formation is very probable. The kinetic boost introduced by the formation of flux may not necessarily result in the same thermodynamic crystalline phases as formed in normal stoichiometric solid state reactions.

Inspired by the above arguments, we attempted to discover new materials in the Ba–Fe–S system using the reactive flux BaS_3. The precursor stoichiometry used in these study is marked with a red cross in Figure 7.1. *In situ* XRD was the primary method for detecting evidence of the existence of materials formation. We conducted both lab *in situ* XRD with a tube furnace and synchrotron *in situ* XRD. Both cases showed clear evidence of crystallizations when the reaction system entered the flux state. These crystals have diffraction patterns that do not match any known materials in the Ba–Fe–S system.

7.2 Synthesis and Characterization

All powder manipulations were performed in an Ar-filled glovebox. All reagents were mixed in stoichiometric ratios, ground, and sealed inside fused silica tubes prior to heat treatment. In the traditional *ex situ* solid state reactions, BaS, Fe, and S are used as reagents. They were sealed inside 15mm O.D., 13 mm I.D. fused silica tubes. The reaction temperature study involved reacting samples for 24 h at 400, 600, and 800 °C respectively. The heating and cooling rates were both 10 °C/min. BaS_3 was synthesized using traditional solid state method with Ba and S in 3:1 molar ratio, heated at 600 °C for 24 h with heating and cooling rates of 10 °C/min. Reagents for *in situ* XRD syntheses were prepared by placing stoichiometric powder mixtures of BaS_3, Fe, and S (typical mole ratio for BaS_3:Fe:S is 4:1:4) inside 0.7 mm-diameter fused silica capillaries, which were sealed under vacuum. For lab *in situ* XRD measurement, the sealed capillaries were further fixed inside 1.0 mm diameter fused silica capillaries. *In situ* XRD reactions were performed by heating from room temperature at 1 °C/min to 600 °C, holding at 600 °C for 6 h, and then cooling at -1 °C/min to room temperature. Lab *in situ* and *ex situ* XRD were both collected on a Bruker D8 ADVANCE diffractometer equipped with Mo K_α source and LYNXEYE XE detector in transmission geometry. *In situ* XRD reactions utilized a home-built anti-scatter slit system and a synchronized TC-Transmission furnace with polyimide windows. A 2θ range of 4-30° was used with a scan speed of $1^\circ\ \text{min}^{-1}$. This translates to a temperature span of 26 °C for a single XRD pattern during heating and cooling. Quantitative Rietveld refinements to the XRD data were performed using the Bruker TOPAS 5 suite.

In situ XRD were also performed at beamline 17-BM-B at APS in ANL. The incident X-ray was monochromatic with a wavelength of 0.2412 Å. The setup used a heating flow cell configuration developed at 17-BM-B (Figure 7.3). Although the capillary was sealed, helium gas flowed outside of it to prevent accidental capillary rupture. Coiled wires above and below the capillary were used for sample heating, with a thermocouple at the end of the capillary for temperature feedback (Figure 7.3). The whole sample stage was moved left and right so that around sample gauge length was 8 mm. The sample was heated and cooled during *in situ* experiment. The system had a change in heating rate once it entered the flux stage. The cooling rate was faster than both the heating rates used. A Varex 4343CT 2D detector was used to capture the diffraction pattern. GSAS-II was used to integrate the 2-D diffraction image over 5° to 355 ° azimuth range (to exclude beam-stop affected area) and 0.7° to 11.29° 2θ range to generate intensity versus 2θ data for further analysis. GSAS-II and Topas 5 were used to process the data.

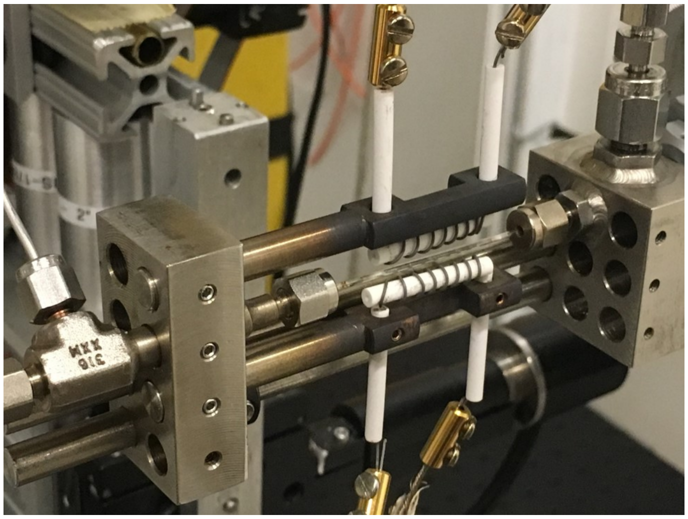

Figure 7.3: A photo that shows the instrumentation for mounting sample capillary used in synchrotron *in situ* XRD at 17-BM-B.

7.3 Results and Discussion

7.3.1 Lab *In Situ* XRD Study on Flux-grown Ba–Fe–S

In situ lab XRD was performed for a precursor system containing BaS_3, Fe, and S in 4:1:4 molar ratio. The overall progress of the reaction can be clearly divided into three stages.

The first stage took place before the formation of the flux. Quantitative Rietveld analysis of the *in situ* XRD patterns in this stage resulted in the phase progression diagram shown in Figure 7.4(a). BaS_3 remained unreactive in this pre-flux stage, with no obvious change in its X-ray intensities except for a small shift due to thermal expansion. Fe was seen with a decrease in its amount starting as early as 250 °C, which was probably attributed to its reaction with S. The signal from the resulting FeS or FeS_2 however, remained low. It was only until 450 °C that the presence of FeS_2 could be ascertained with our *in situ* XRD quality. These developments in the pre-flux states are expected. They followed our observation of Fe–S reaction kinetics in Chapter 6 and obeyed the predictions from Ba–S (Figure 7.3) and Fe–S phase diagrams (Figure 6.3).

The second stage was where BaS_3 melted and the system was in the flux state. The *in*

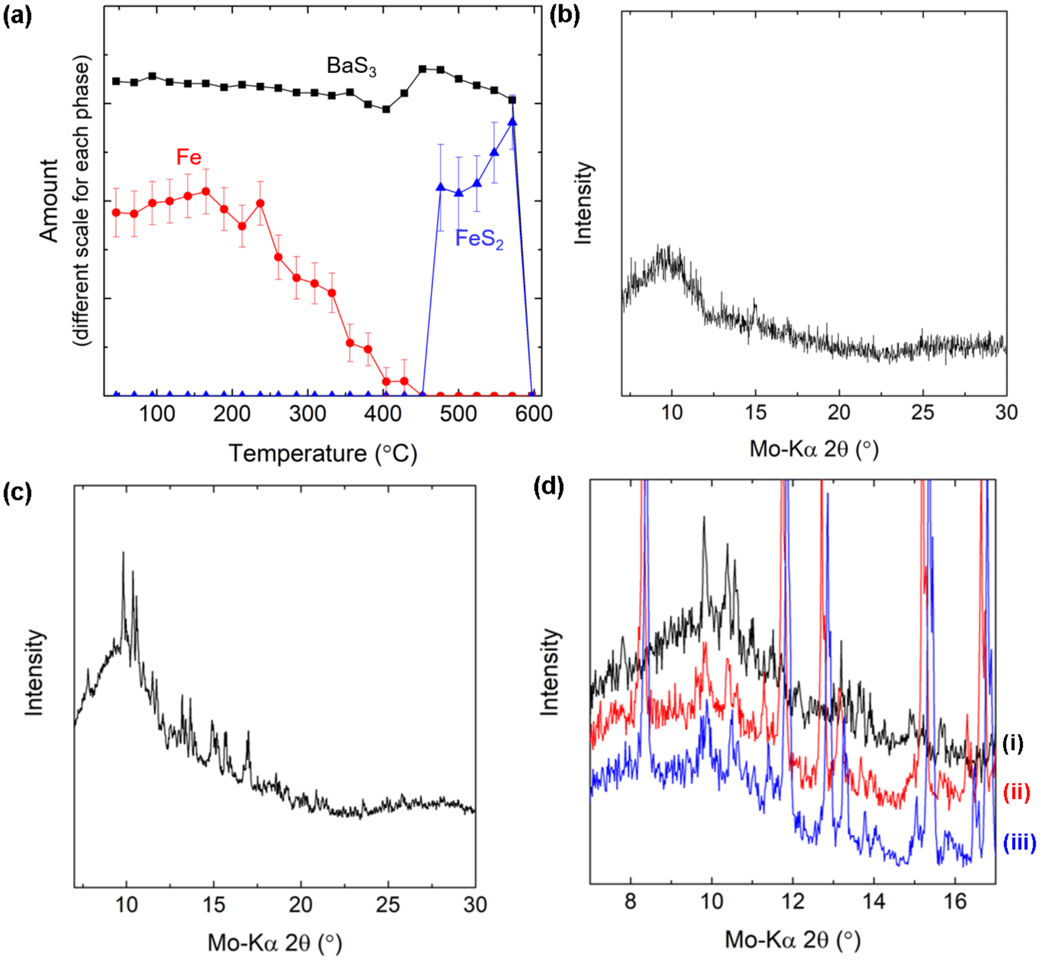

Figure 7.4: (a) Quantitative Rietveld refinement result on the lab *in situ* XRD for the $4BaS_3 + Fe + 4S$ reaction in the pre-flux stage. (b) The first *in situ* lab XRD pattern for the sample in the flux stage. (c) The summed diffraction intensity for all lab *in situ* flux-stage XRD patterns with 2 to 6 h after entering flux stage. (d) Lab *in situ* XRD patterns showing cooling from the flux stage with: (i) the last pattern in the flux stage, (ii) the first pattern in the post-flux stage, and (iii) the pattern after cooling to room temperature.

situ XRD pattern of the system when it just entered the flux state is shown in Figure 7.4(b). It shows a completely amorphous diffraction pattern. The hump around $2\theta=10°$ was mainly attributed by the interfering signals from the furnace instead of the sample. It is interesting that prior to flux formation, there were two crystalline phases: BaS_3 and FeS_2. At this temperature, only BaS_3 was supposed to melt. However, the completely amorphous XRD pattern means that BaS_3 flux (together with some S) was able to dissolve those few FeS_2 crystals present. The XRD patterns in the flux state changed gradually with time. After entering into the flux state for more than 2 hours, Bragg peaks in the XRD pattern were very obvious. The signal-to-noise ratios for these Bragg peaks were very low though, so I summed up all the *in situ* XRD patterns in the flux stage (with >2h flux time), which is shown in Figure 7.4(c). The presence of these Bragg peaks shows that crystalline materials grew within the flux. Phase matching on these peaks showed that they corresponded to no known structures in the Ba–Fe–S system. These findings prove our postulation that BaS_3 flux can trigger the system to precipitate crystalline phase(s) that are different from what was known from stoichiometric solid state reactions.

The last stage is the post-flux stage, during which cooling has condensed the flux to BaS_3 crystals. XRD patterns for the system at this stage were dominated by the Bragg signals of BaS_3, so the intensity scale had to be changed to observe the peaks relevant to the flux-grown phases (Figure 7.4(d)). The observation that Bragg intensities from flux-grown phases were tiny compared to BaS_3 showed that crystal growth yield was low for this flux synthesis. Nevertheless, it can be seen that when the reaction system cooled below the flux stage and BaS_3 crystallized, the Bragg signals of the flux-grown phases did not disappear (Figure 7.4(d)).

However, it is challenging to get more information regarding the nature of the flux-grown phases relying simply on lab XRD. We did not know how many phases together contribute to the Bragg signals seen in the flux stage (Figure 7.4(c)). It is practically impossible to solve crystal structure of unknown phase mixtures using powder diffraction. Also, lab XRD did not have sufficient X-ray intensity for such a purpose even if only one flux-grown phase was present. We used *in situ* XRD using synchrotron source at 17-BM-B in APS to investigate the flux-driven processes in more detail.

7.3.2 Synchrotron-based *In Situ* XRD Study of Flux-grown Ba–Fe–S

Synchrotron *in situ* XRD of new Ba–Fe–S phases was carried out at beamline 17-BM-B in APS. This effort was made to improve time resolution and diffraction intensities of the new phases.

However, there were several shortcomings in my practice of this *in situ* XRD design. First, temperature uniformity over the length of sample capillary was poor. During lab *in situ* XRD practice, the capillary was placed inside a tube furnace which had ceramic insulations over most of the furnace wall. This created a decent temperature uniformity. However, in the 17-BM-B *in situ* XRD experiments, two heating coils situated above and below the sample capillary were used for sample heating without any thermal insulation. The overall heating power was not uniformly distributed, being stronger in the middle and fading quickly towards the edge. An ideal design would require the capillary length to be $<$ 25% of the coil length for approximately uniform sample temperature. Such short capillary lengths were hard to make with our sealing torch, so the sample capillaries used here were about 80% of the coil length. These temperature variations in the sample may cause further complications due to the presence of mobile liquid / gas phases involved in the reactions. Since we translated the capillary horizontally with a travel distance of 8 mm, the resultant XRD pattern had contributions from samples at different temperatures, further complicating the analysis. Second, the thermocouple did not provide accurate temperature feedback due to the temperature inhomogeneity problem. The thermocouple was placed near the end of the capillary. Therefore, the sample at the middle of the capillary was expected to be at a higher temperature than the thermocouple reading. As a result, the thermocouple readings could be used as temperature trends, but not as absolute sample temperature values. Third, the reactor could not rotate due to the electrical leads and gas flow tubes. Therefore if texturing existed in the sample due to large crystallite sizes or small number of particles in the gauge volume, its effects were going to be significant.

One observation from the *in situ* XRD experiment at 17-BM-B was that these flux-forming Ba–Fe–S reaction systems were extremely sensitive. We tested samples very close in stoichiometry ($\sim$4:1:4 BaS_3:Fe:S molar ratio), but they behaved differently. These samples had similar developments during the pre-flux stage judged from *in situ* XRD. However, once they entered the flux state, their diffraction patterns diverged. In all cases, Bragg peaks were seen in the flux states, but they differed in 2θ values. This showed that crystallization processes from the BaS_3 flux were sensitively dependent on some features that were hard to control with our practice of sample preparation. Nevertheless, crystalline inorganic materials formation from the flux happened for all samples. From here onwards, the focus will be devoted to the flux state of a single representative reaction test.

Figure 7.5 shows a waterfall plot for the evolution of *in situ* XRD patterns that will be discussed. The three pre-flux, flux, and post-flux stages discussed in the previous section are obvious. The developments of the system in the pre-flux and post-flux stages were very similar to that observed from lab *in situ* XRD, so only the flux-stage will be addressed in detail.

The diffraction patterns kept evolving during the flux-stage, showing that more than one phase was crystallized. The differential changes of the Bragg peak intensities gave clues on how to bundle the Bragg peaks group into different groups. With this approach representative *in situ* XRD patterns corresponding to different combinations of phases were picked out.

At the highest examined temperature, the diffraction pattern contained the least number of Bragg peaks (Figure 7.6(a)). It is reasonable to argue that the majority of crystalline phases were unstable / melted at this temperature so that only a few compounds could survive. Here it is assumed that only one phase remained at such high temperature and therefore

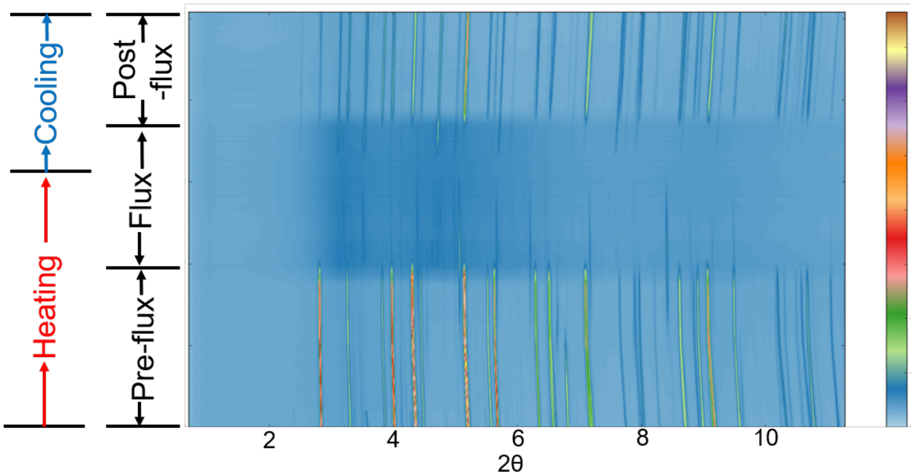

Figure 7.5: Waterfall plot showing the overall evolution of *in situ* XRD patterns for the 4BaS3 + Fe + 3S reaction.

these Bragg peaks were from this phase alone. This is termed phase "HT1." As can be seen from Figure 7.6(a), the diffraction intensities from the "HT1" phase were extremely low. They were merely visible over the amorphous background contributed from the liquid flux. Using GSAS-II, the amorphous background was manually defined and subtracted (Figure 7.6(b)). The Bragg peaks were then selected and fitted in Topas as a "peak phase" whose refined contribution is shown in Figure 7.6(c). Phase indexing was carried out to look for potential space group for this "HT1" phase. The top candidates were the following: space group $Pmc2_1$ with lattice parameters a = 5.55Å, b = 7.24Å, and c = 9.00Å; space group $P222$ with a = 9.00Å, b = 5.55Å, and c = 7.23Å; space group $P2_12_12_1$ with a = 9.00Å, b = 7.24Å, and c = 5.55Å; space group $P2_12_12$ with a = 9.00Å, b = 7.24Å, and c = 5.55Å. Figure 7.6(d) shows the Le Bail fit result to the diffraction pattern with space group $Pmc2_1$.

Starting from the "HT1" phase patterns and looking in the reverse heating direction, another group of diffraction patterns composed of similar peaks was identified. Here some of the Bragg peaks could be assigned to "HT1" or FeS_2 while some could not be assigned to anything known (Figure 7.7(a)). We assumed these unassigned peaks were from another phase termed "HT2." Following the same procedure of removing amorphous flux background (Figure 7.7(b)), the pattern was fit with FeS_2 using crystal structure information and the

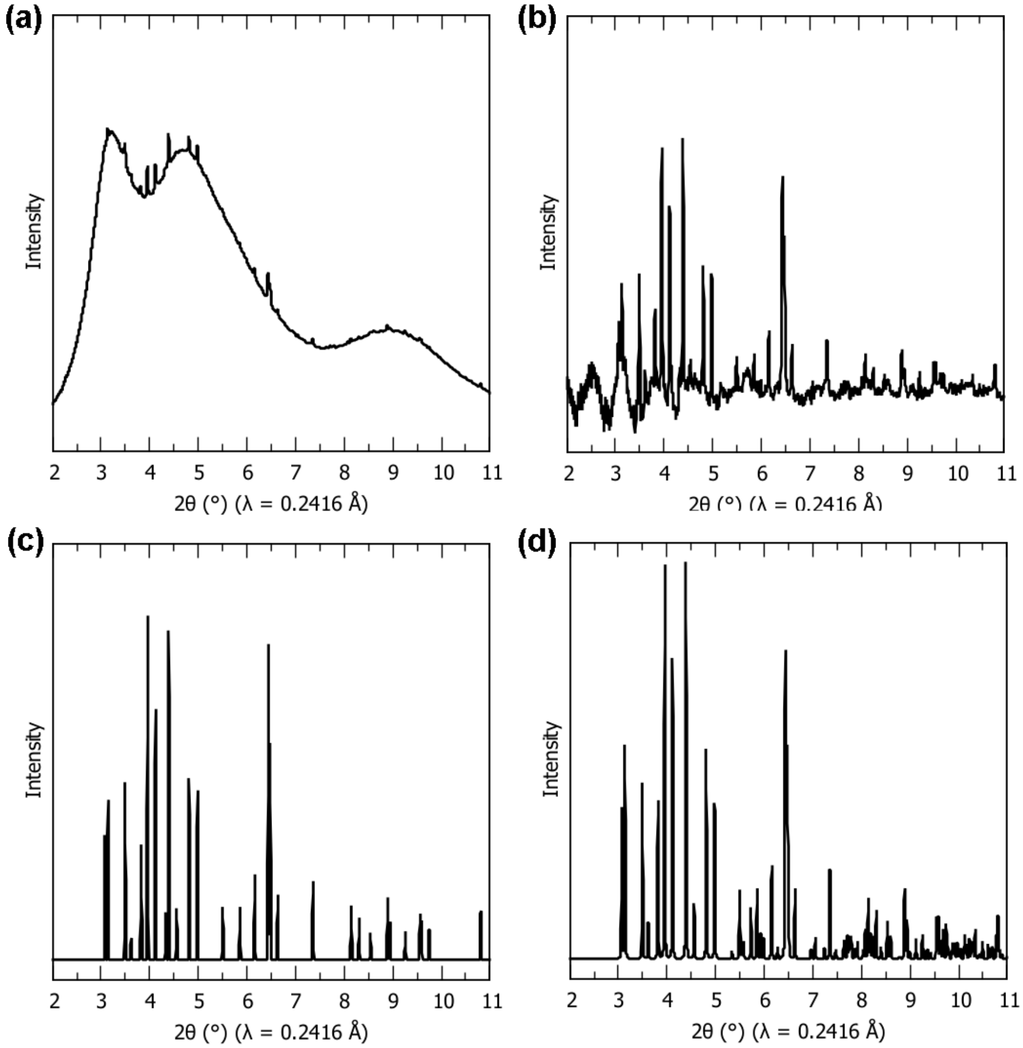

Figure 7.6: (a) *In situ* diffraction pattern showing phase "HT1." (b) The diffraction pattern of (a) with flux background removed. (c) Suggested diffraction pattern of "HT1" based on "peak phase" fitting. (d) Suggested diffraction pattern of "HT1" based on Le Bail fitting.

previously Le Bail fitted “HT1” model. The remaining peaks were selected and fitted as a “peak phase” for “HT2,” whose contribution is shown in Figure 7.7(c). The top indexing result of this profile were the following: space group $P2$ with a = 8.94Å, b = 1.96Å, c = 12.7Å, and β = 94.8°; space group $P\bar{1}$ with a = 4.73Å, b = 5.16Å, c = 6.18Å, α = 108°, β = 94.4°, and γ = 70.2°; space group $P\bar{1}$ with a = 5.01Å, b = 5.70Å, c = 7.14Å, α = 88.6°, β = 74.8°, and γ = 111°. Figure 7.7(d) shows the Le Bail fit of the “HT2” contribution to the diffraction pattern with space group $Pmc2_1$.

Going further in the reverse heating direction, the peaks from “HT2” phase faded in intensities while another group of peaks came up. Figure 7.8(a) shows a representative diffraction pattern for this group of patterns which composed of FeS_2, “HT1,” and this new phase coded as “HT3.” Following the same procedure of removing amorphous flux background (Figure 7.8(b)), the pattern was fit with FeS_2 using crystal structure information and the previously Le Bail fitted “HT1” model. The remaining peaks were selected and fitted as a “peak phase” for “HT3,” whose contribution is shown in Figure 7.8(c). The top indexing result of this profile were the following: space group Pc with a = 18.4Å, b = 4.71Å, c = 8.87Å, and β = 62.5°; space group $P2_1/c$ with a = 18.4Å, b = 4.71Å, c = 8.87Å, and β = 62.5°; space group $P2_1$ with a = 18.4Å, b = 4.71Å, c = 8.87Å, and β = 62.5°; space group $C2$ with a = 13.9Å, b = 11.9Å, c = 8.91Å, and β = 83.5°; space group $P2$ with a = 26.3Å, b = 4.12Å, c = 4.65Å, and β = 97.8°. Figure 7.8(d) shows the Le Bail fit of the “HT2” contribution to the diffraction pattern with space group Pc.

Working in the other direction, the cooling direction, and starting from the “HT1” phase patterns, we found the emergence of a group of peaks which we assigned to phase “CO1” (Figure 7.9(a)). Following the same procedure of removing amorphous flux background (Figure 7.9(b)), the pattern was fit with the previously Le Bail fitted “HT1” model. The remaining peaks were selected and fitted as a “peak phase” for “CO1,” whose contribution is shown in Figure 7.9(c). The top indexing result of this profile were the following: space group $F222$ with a = 11.1Å, b = 7.81Å, and c = 6.19Å; space group $C2$ with a = 7.82Å,

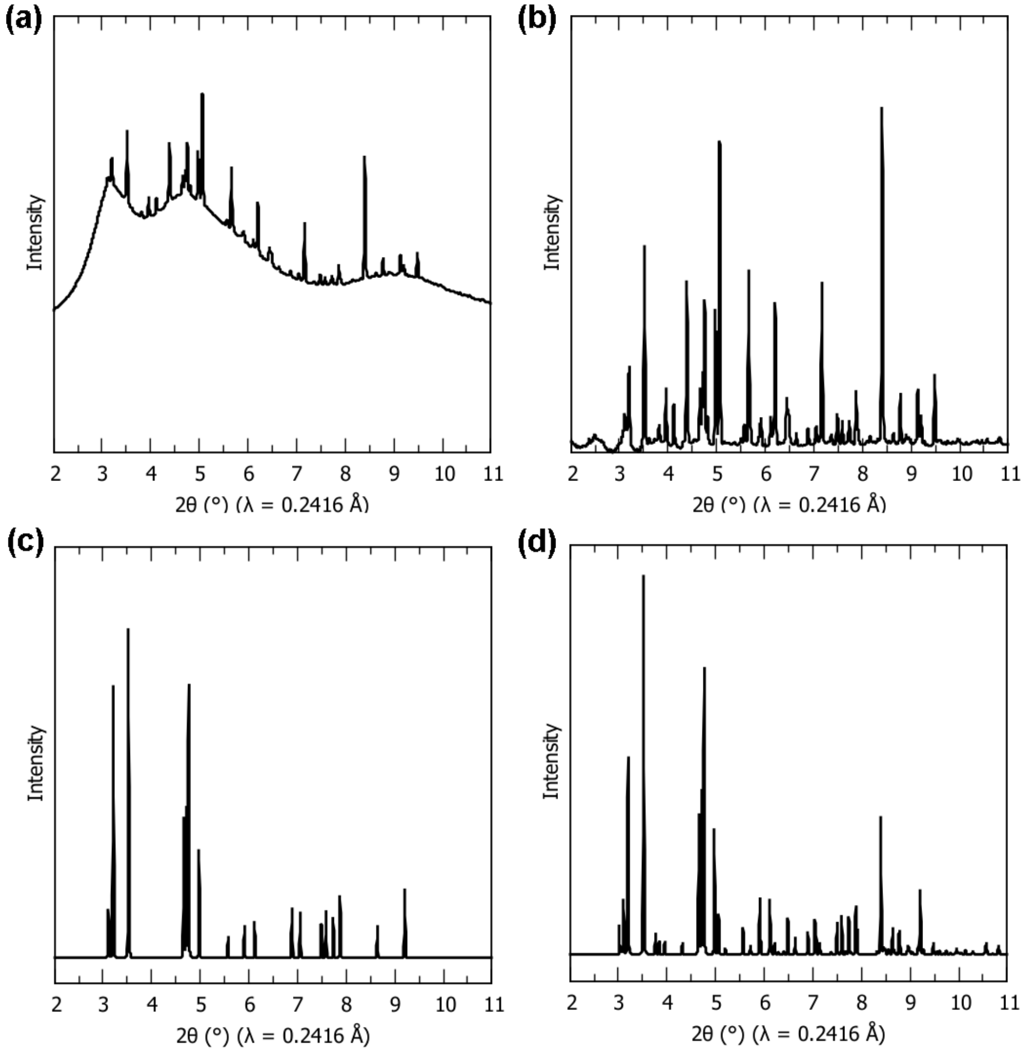

Figure 7.7: (a) *In situ* diffraction pattern showing phases FeS_2 + "HT1" + "HT2." (b) The diffraction pattern of (a) with flux background removed. (c) Suggested diffraction pattern of "HT2" based on "peak phase" fitting. (d) Suggested diffraction pattern of "HT2" based on Le Bail fitting.

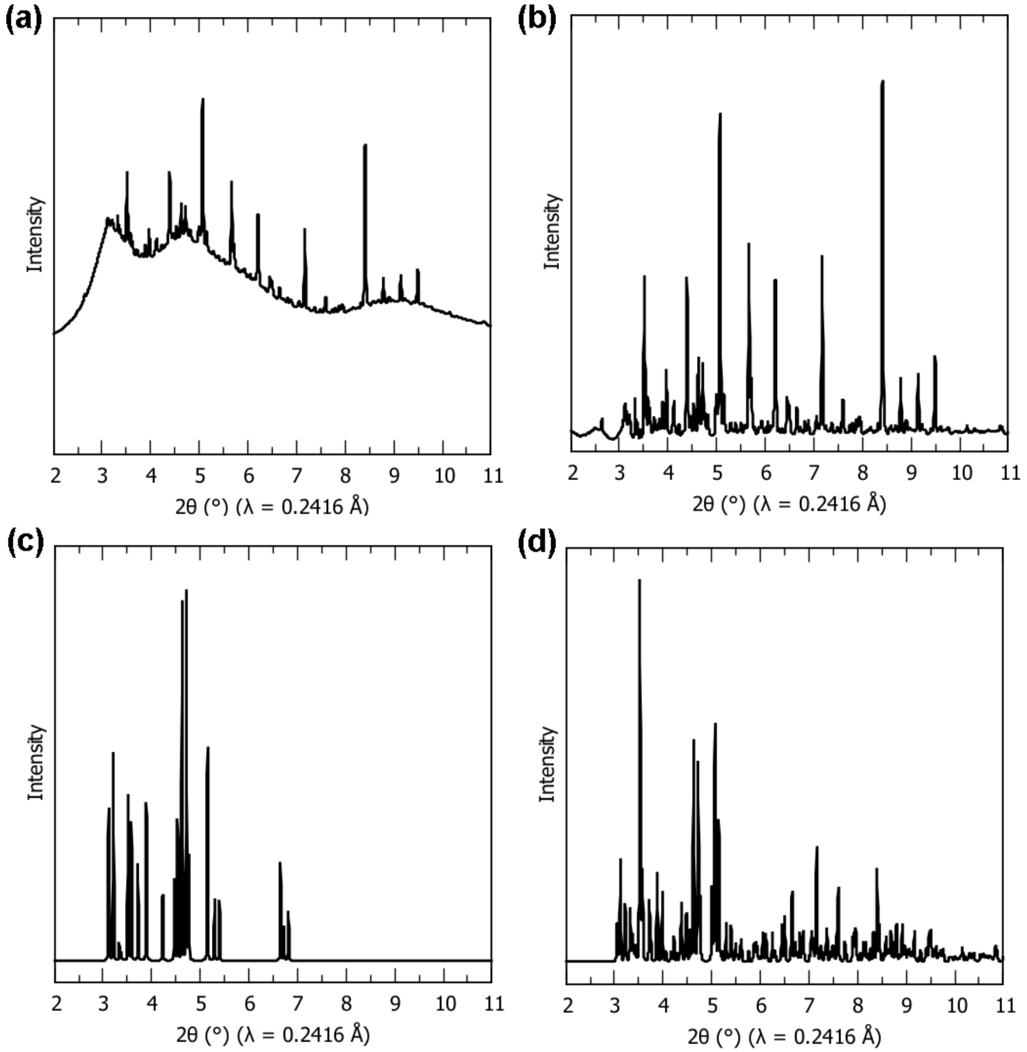

Figure 7.8: (a) *In situ* diffraction pattern showing phases FeS_2 + "HT1" + "HT3". (b) The diffraction pattern of (a) with flux background removed. (c) Suggested diffraction pattern of "HT3" based on "peak phase" fitting. (d) Suggested diffraction pattern of "HT3" based on Le Bail fitting.

$b = 6.18$Å, $c = 6.77$Å, and $\beta = 125°$. Figure 7.9(d) shows the Le Bail fit of the "HT2" contribution to the diffraction pattern with space group $F222$.

Going further in the cooling direction, another group of peaks appeared. These peaks were assigned with phase "CO2" (Figure 7.10(a)). Following the same procedure of removing amorphous flux background (Figure 7.10(b)), the pattern was fit with the previously Le Bail fitted "HT1" and "CO1" model. The remaining peaks were selected and fitted as a "peak phase" for "CO2," whose contribution is shown in Figure 7.10(c). The top indexing result of this profile are the following: space group $P2$ with $a = 10.9$Å, $b = 3.47$Å, $c = 5.52$Å, and $\beta = 129°$; space group $P2$ with $a = 7.49$Å, $b = 3.48$Å, $c = 4.46$Å, and $\beta = 74.9°$; Figure 7.10(d) shows the Le Bail fit of the "HT2" contribution to the diffraction pattern with space group $P2$ using the first set of cell parameters.

Structure solution of these identified phases is challenging with the data quality we have here. First, many of these crystallites grown from the flux showed significant texture effects. These can be seen by detailed examinations of the 2-D diffraction image data. Structural solution requires statistical significance from the powder data. Textured data is not suitable for this purpose. Furthermore, most of the *in situ* diffraction intensities for the flux-grown phases were not high, even with the use of synchrotron source at 17-BM-B. In the future, it could be more desirable to do isothermal scans over a small sample volume with longer detection time to improve data quality. With the current data quality, the credibility of the results from peak phase assignments, indexings, and Le Bail refinements are not good. These errors propagated, so the more phases there were in the pattern, the less the results should be trusted. This can be seen from "HT3" and "CO2" phases, whose indexing results have low symmetry and are therefore questionable. In general, diffraction patterns suggested for each phase with "peak phase" fit can be expected to under-count peak numbers, and that with Le Bail fit can be expected to over-count peak numbers. Nevertheless, the evolution of the *in situ* diffraction patterns with the use of synchrotron showed that there were at least 5 new structural types buried in the Ba–Fe–S compositional space, and flux synthesis using

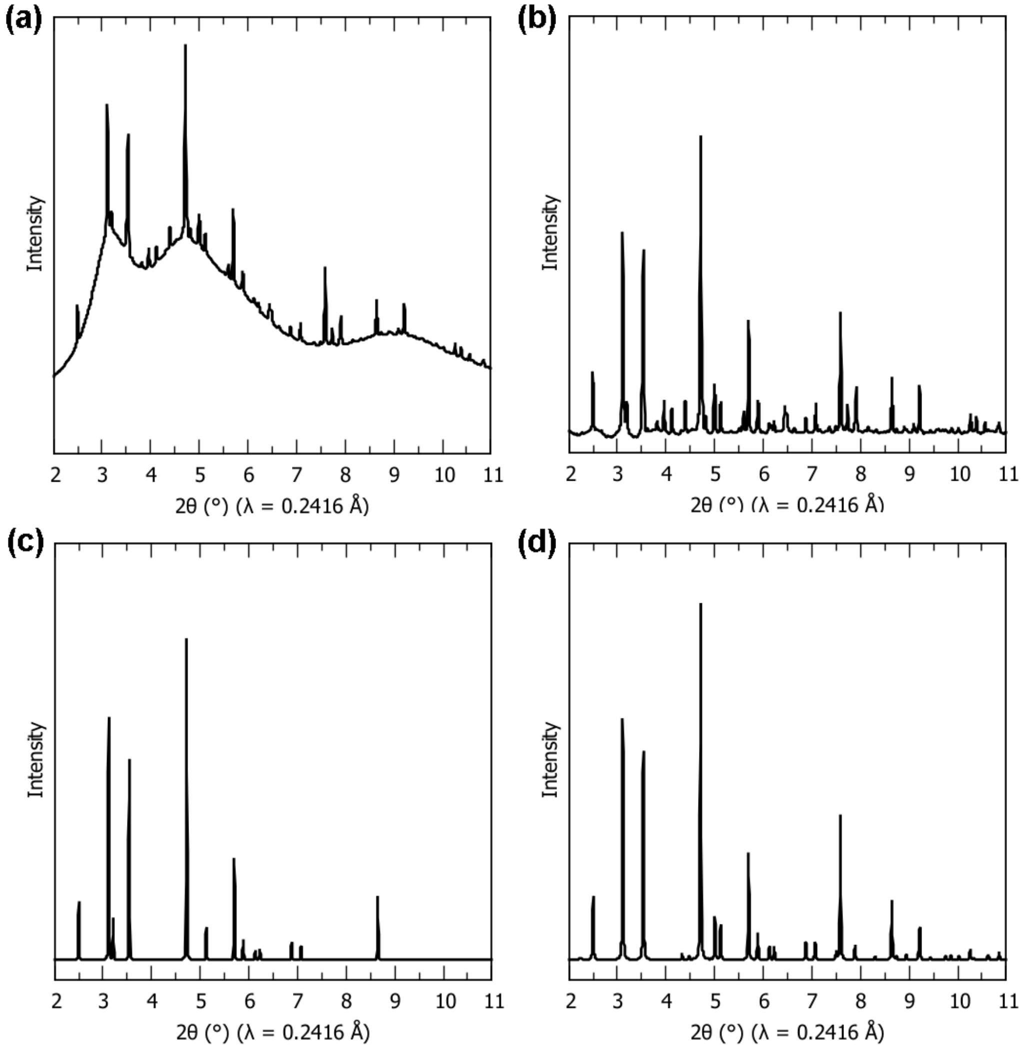

Figure 7.9: (a) *In situ* diffraction pattern showing phases "HT1" + "CO1." (b) The diffraction pattern of (a) with flux background removed. (c) Suggested diffraction pattern of "CO1" based on "peak phase" fitting. (d) Suggested diffraction pattern of "CO1" based on Le Bail fitting.

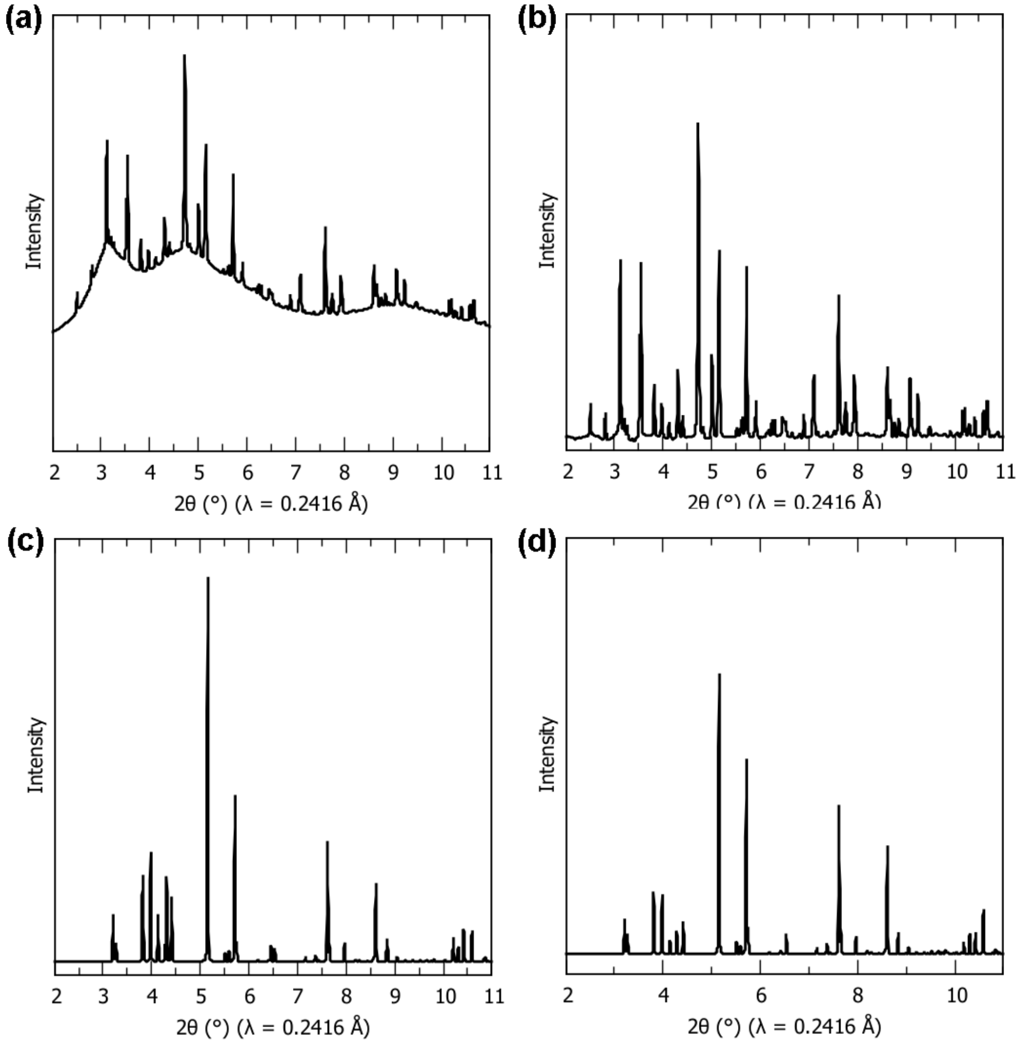

Figure 7.10: (a) *In situ* diffraction pattern showing phases “HT1” + “CO1” + “CO2”. (b) The diffraction pattern of (a) with flux background removed. (c) Suggested diffraction pattern of “CO2” based on “peak phase” fitting. (d) Suggested diffraction pattern of “CO2” based on Le Bail fitting.

BaS_3 was a useful method to access them.

7.4 Conclusions

Flux synthesis is an effective method to access material structures that cannot be accessed with traditional stoichiometric solid state synthesis. This was tested in the Ba–Fe–S system to look for new ternary compounds with the use of BaS_3 as the main reactive flux and five new material phases were discovered. Lab *in situ* XRD revealed that crystalline materials grew from the flux formed by the melting of BaS_3. These materials had diffraction patterns not matched by any known structures and are likely unreported materials. *In situ* XRD of the flux-growth of ternary Ba–Fe–S crystals was further conducted at APS beamline 17-BM-B. Analysis showed that the diffraction patterns for the flux-grown crystals changed with temperature, and we were able to allocate the peaks seen in the flux stage to five distinct phases. We gave suggested appearances for the diffraction patterns of these five newly discovered phases, although their full structure solution would require more effort. This would require a more consistent manner to produce sample capillaries that are better mixed, a better temperature uniformity during *in situ* XRD experiment, a smaller sampling volume during diffraction, and a strategy for data collection to get more statistical "powder" data.

CHAPTER 8

DISCOVERY OF TERNARY CHALCOGENIDE PHASES USING BALL MILLING

8.1 Introduction

During *in situ* examinations of the formation of Fe_2SiS_4 with elements as the starting reagents in Chapter 6, it was discovered that ball milling the reagents could effectively reduce the formation temperature of Fe_2SiS_4 so that peritectic dissociation of FeS_2 was no longer relevant. These raised the following question: in our group's previous studies that constructed phase diagrams for ceramic materials, were there materials hidden from discovery due to insufficient reaction kinetics?

Narayan *et al.* performed a systematic theoretical search using density functional theory (DFT) over 27 ternary systems containing selenium or sulfur for unknown materials that may be thermodynamically stable. [204] A probabilistic model was used to reduce the likelihood of false negative predictions. A list of 24 candidate materials was thus proposed, which is copied in Figure 8.1. To experimentally verify the phase stabilities predicted by calculation, my groupmate, Ankita Bhutani conducted syntheses in the suggested systems using solid state synthesis and CS_2 gas flow reactions. However, no new phases were experimentally verified.

Since the previous solid state syntheses experiments were performed using hand-grinding, their effectiveness in forming ternary structures could be hindered by kinetic effects. Ball milling might be used to overcome these kinetic barriers, as demonstrated in Chapter 6. Inspired by this, we re-verified phase stabilities of a subset of the DFT-predicted materials experimentally. This time all reagents were mixed and ball milled prior to heat treatment

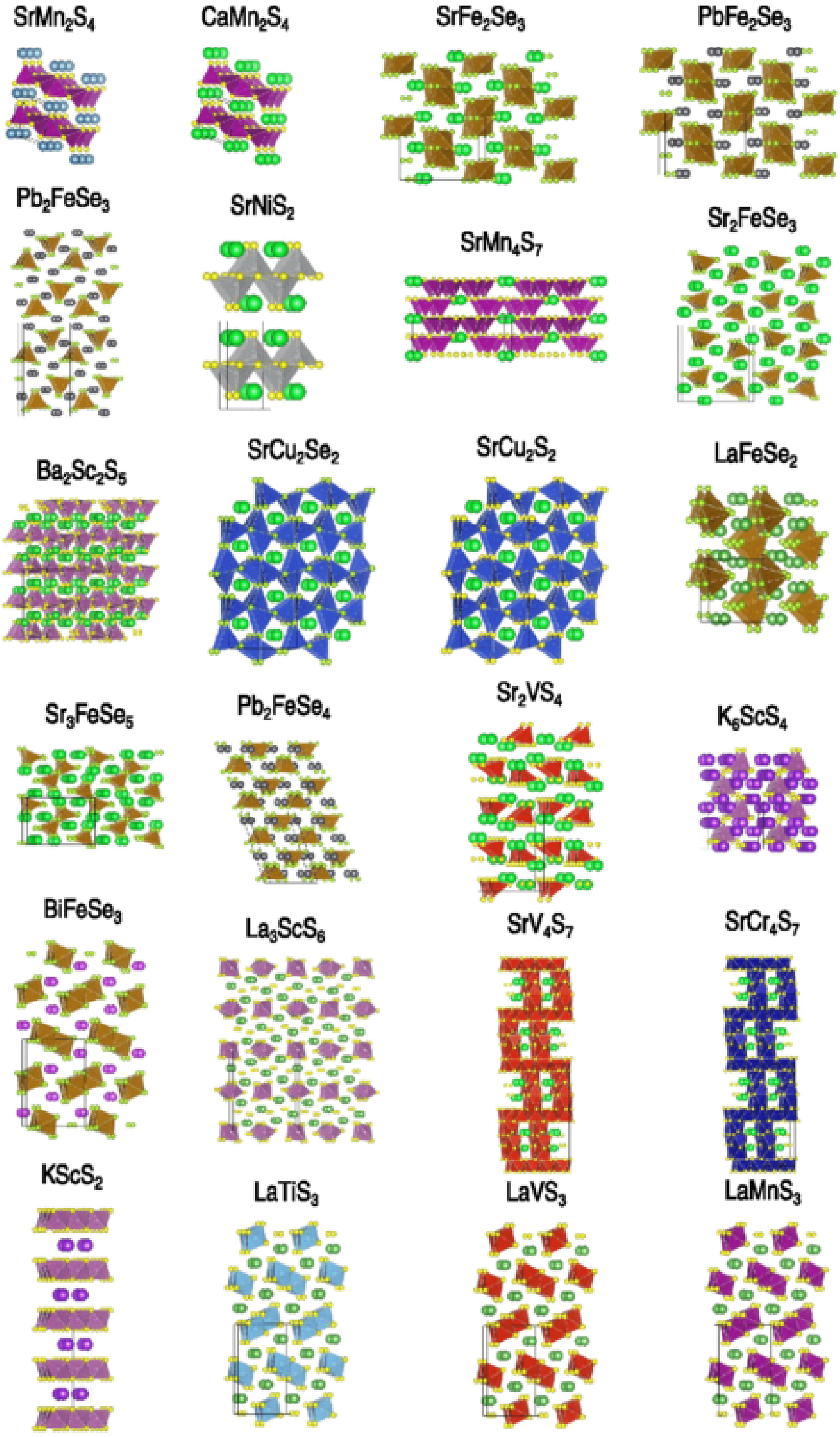

Figure 8.1: The list of materials that were predicted to be potentially thermodynamically stable by DFT calculations performed by Narayan *et al.* [204]

at different temperatures. A total of 11 ternary phase systems were investigated with this approach, with a total of 15 stoichiometries. The tested stoichiometries were 1:2:4 Ca:Mn:S, 1:2:4 and 1:4:7 Sr:Mn:S, 1:2:2 Sr:Cu:S, 2:1:4 and 1:4:7 Sr:V:S, 1:4:7 Sr:Cr:S, 1:1:2 Sr:Ni:S, 1:1:5 La:Fe:Se, 1:2:3 and 2:1:3 Sr:Fe:Se, 1:2:2 Sr:Cr:Se, 1:2:3 and 2:1:4 Pb:Fe:Se, and 1:1:3 Bi:Fe:Se (all in molar ratio).

The majority of the systems examined only formed mixtures of binary compounds (hence the DFT-predicted phases were absent) and produced similar products to the previous experiments without using ball milling. But in three systems, we obtained diffraction patterns that contained Bragg peaks that we could not assign to any known phases, which were different from what we saw previously. These systems are Sr–V–S, Sr–Cr–S, and Sr–Ni–S. We also saw interesting developments in the Ca–Mn–S system, which seemed to form solid solutions from ball-milling that violated known phase diagrams.

8.2 Synthesis and Characterization

All reagents were weighed in the stoichiometric ratio (total weight ~2 g) in an Argon-filled glovebox and placed inside a SPEX SamplePrep 8001 hardened steel grinding vial. One 3/8 inch and three 1/2 inch hardened steel balls were used for ball milling. The grinding vial was then transformed to a SPEX SamplePrep 8000D Mixer/Mill in another Ar-filled glovebox and ball milled for 1 h. The grinding vial was then taken to the original sample preparation glovebox and separated into 4 parts. Three parts were each placed inside a 15 mm O.D. (13 mm I.D.) fused silica tube which was later flame sealed under vacuum. These samples were then heated inside box furnaces at 300 °C, 500 °C, and 700 °C (with 10 °C/min heating rate) respectively. Isothermal heating time was 24 h. After that the samples were quenched in water, retrieved and ground in the glovebox.

The reagents and final elemental molar stoichiometries of the examined samples are listed below. Ca particles, Mn chips, and S flakes were mixed to make 1:2:4 Ca:Mn:S. SrS powder, Mn chips, and S flakes were mixed to make 1:2:4 and 1:4:7 Sr:Mn:S. SrS powder, V powder, and S flakes were mixed to make 2:1:4 and 1:4:7 Sr:V:S. SrS powder, Cr powder, and S flakes were mixed to make 1:4:7 Sr:Cr:S. SrS powder, Ni powder, and S flakes were mixed to make 1:1:2 Sr:Ni:S. SrS powder, Cu powder, and S powders were mixed to make 1:2:2 Sr:Cu:S. La powder, Fe powder, and Se powder were mixed to make 1:1:5 La:Fe:Se. Sr chunk, Fe powder, and Se powder were mixed to make 1:2:3 and 2:1:3 Sr:Fe:Se. Sr chunk, Cu powder, and Se powder were mixed to make 1:2:2 Sr:Cu:Se. Pb powder , Fe powder, and Se powder were mixed to make 1:2:3 and 2:1:4 Pb:Fe:Se. Bi needles, Fe powder, and Se powder were mixed to make 1:1:3 Bi:Fe:Se.

The as-ball-milled powders and the heat-treated samples were ground and packed inside 0.7 mm diameter polyimide capillaries for X-ray diffraction measurements. Certain samples were diluted with amorphous silica powder to reduce X-ray absorption, whose details were listed below. 2:1:4 Sr:V:S, and 1:1:2 Sr:Ni:S were diluted to 50 wt%. 1:1:5 La:Fe:Se, 1:2:3 Sr:Fe:Se, 2:1:3 Sr:Fe:Se, and 1:2:2 Sr:Cu:Se were diluted to 20 wt%. 1:2:3 Pb:Fe:Se and 1:1:3 Bi:Fe:Se were diluted to 10 wt%.

Powder XRD data were collected on a Bruker D8 ADVANCE diffractometer equipped with Mo K_α source and LYNXEYE XE detector in transmission geometry. Rietveld refinement were performed on Bruker Topas 5 suite.

8.3 Results and Discussion

XRD patterns for the various ternary system studied with ball milling the reagents and reacted at various temperatures are summarized in Table 8.1. Note that only the crystalline components can be revealed by XRD and included in the table. Discussion of the specific systems is presented below.

Table 8.1: Products after heat treatment of ball-milled reagents

Reagents	**Overall stoichiometry**	**As-ground products**	**300°C products**	**500°C products**	**700°C products**
Ca,Mn,S	1:2:4 Ca:Mn:S	CaS, Mn, (Ca,Mn)S / **Unknown**	CaS, MnS, Mn, (Ca,Mn)S / **Unknown**	CaS, MnS	CaS, MnS
SrS,Mn,S	1:2:4 Sr:Mn:S	SrS, Mn, S	SrS, Mn, S	SrS, MnS	SrS, MnS
	1:4:7 Sr:Mn:S	SrS, Mn, S	SrS, MnS, Mn	SrS, MnS	SrS, MnS
SrS,V,S	2:1:4 Sr:V:S	SrS, V, S	SrS, V, **Unknown**	SrS, **Unknown**	SrS, **Unknown**
	1:4:7 Sr:V:S	SrS, V, S	SrS, V, S	V_5S_8, **Unknown**	V_5S_8, **Unknown**
SrS,Cr,S	1:4:7 Sr:Cr:S	SrS, Cr, S	SrS, Cr, S	SrS, Cr_2S_3	Cr_2S_3, **Unknown**
SrS,Ni,S	1:1:2 Sr:Ni:S	SrS, Ni	SrS, NiS, **Unknown**	SrS, NiS	SrS, NiS
SrS,Cu,S	1:2:2 Sr:Cu:S	SrS, $Cu_{2-x}S$	SrS, CuS/Cu_2S	SrS, $Cu_{2-x}S$	SrS, $Cu_{2-x}S$, Cu_2S
La,Fe,Se	1:1:5 La:Fe:Se	LaSe, Fe, $FeSe_2$	$LaSe_2$, $FeSe_2$	$LaSe_2$, $FeSe_2$	$LaSe_2$, $FeSe_{1-x}$
Sr,Fe,Se	1:2:3 Sr:Fe:Se	SrSe, Fe, FeSe	SrSe, Fe–Se, Fe	SrSe, $Fe_{1-x}Se$	SrSe, $Fe_{1-x}Se$
	2:1:3 Sr:Fe:Se	SrSe, Fe	SrSe, $FeSe_2$, Fe–Se, Fe	SrSe, FeSe	SrSe, $Fe_{1-x}Se$
Sr,Cu,Se	1:2:2 Sr:Cu:Se	SrSe, $Cu_{2-x}Se$	SrSe, $Cu_{2-x}Se$	SrSe, $Cu_{2-x}Se$	SrSe, $Cu_{2-x}Se$
Pb,Fe,Se	1:2:3 Pb:Fe:Se	PbSe, Fe	PbSe, $FeSe_2$, Fe–Se, Fe	PbSe, FeSe, Fe	PbSe, FeSe
	2:1:4 Pb:Fe:Se	PbSe, Fe	PbSe, $FeSe_2$	PbSe, $FeSe_2$	PbSe, Fe_3Se_4
Bi,Fe,Se	1:1:3 Bi:Fe:Se	Bi_2Se_3, Fe	Bi_2Se_3, $FeSe_2$, Fe_3Se_4?	Bi_2Se_3, FeSe?	Bi_2Se_3, FeSe?

8.3.1 Selenide Systems

We did not observe any formation of ternary selenides in the tested systems. All reactions produced only binary selenides. It was shown that ball-milling was energetic enough to cause binary selenide-forming reactions for the following metals: Sr, Pb, Bi, La, Cu.

After ball milling La, Fe, and Se (1:1:5 molar ratio), XRD suggested that the sample contained crystalline LaSe, $FeSe_2$ and Fe. The extent of Fe to $FeSe_2$ transformation was low, indicating that ball milling was effective for the selenization of La, but not Fe. The diffraction intensities for the as-ground sample were low. Heating increased the crystallinities of the samples. Starting from 300 °C, LaSe was transformed to $LaSe_2$, and Fe was transformed to $FeSe_2$. At 700 °C, $FeSe_{0.92}$ became stable instead of $FeSe_2$.

The reactions in the Sr–Fe–Se, Pb–Fe–Se, Bi–Fe–Se, and Sr–Cu–Se systems had selenizations of different metals taken place independently. After ball milling, selenization caused Sr to become SrSe, Pb to become PbSe, Bi to become Bi_2Se_3, and Cu to become Cu_2Se. SrSe, PbSe, and Bi_2Se_3 remained unchanged with reaction temperatures up to 700 °C. Some transformations between different forms of binary iron selenides and copper selenides took place with increasing temperature, but all changes were confined within binary selenides and no ternaries were seen.

In short, ball milling was very effective to form binary selenides (SrSe, PbSe, Bi_2Se_3, $LaSe_2$, Cu_2Se) with elements are reagents, but did not induce any ternary formation with increased reaction temperature.

8.3.2 Sulfide Systems

Ball milling was found to have more drastic influences of the formation of ternary sulfides. Many ball-milled samples had diffraction patterns with unmatched peaks after heat treatment. These likely contain new materials.

For the Sr–Mn–S system, ball milling did not make a significant difference compared to hand-grinding. With the use of SrS as a starting reagent, no reaction happened after ball milling. After 24 hours of reaction at 300 °C, some Mn were sulfizied to MnS. Complete sulfidations (MnS and SrS) were achieved at 500 and 700 °C. These results are exactly the same as obtained by hand-grinding. [204] For the Sr–Cu–S system, SrS remained unreactive at all tested temperatures, whereas Cu probably formed various forms of binary copper sulfides. The exact nature of the binary copper sulfides can be hard to establish, but no promising signs for the formation of any ternary compounds were evident.

The story for ball-milled Ca–Mn–S (1:2:4 stoichiometry) is more complicated. While both the ball-milled and hand-ground samples showed MnS and CaS after reactions at 500 and 700 °C (Figure 8.2(c,d)), their behaviors at low temperatures were less similar. With hand-grinding, the sample consisted of MnS, CaS, as well as metallic Mn at 300 °C. [204] When the reagents were ball milled, there was an additional phase in the as-ground and 300 °C reacted samples. This phase co-existed with CaS and Mn in the as-ground state, and co-existed with CaS, MnS, and Mn after reacted at 300 °C, with its XRD peak intensities higher than the other phases (Figure 8.2(a,b)). The diffraction peak profile for this phase implied that it had a similar rock salt crystal structure to MnS and CaS, but with a lattice parameter in between them. These seem to suggest that this new phase was a solid solution of CaS and MnS in the form of $Ca_xMn_{1-x}S$. Based on our Rietveld refinement fit the 300 °C pattern (Figure 8.2(b)), and assuming a linear dependence on the lattice parameter with x in $Ca_xMn_{1-x}S$, it was calculated that this phase had a composition of $Ca_{0.33}Mn_{0.67}S$. The Rietveld refinement results in Figure 8.2(a,b) was done by assuming this phase to be rock salt $Ca_{0.33}Mn_{0.67}S$. Based on the current CaS–MnS phase diagram, full solid miscibility is thermodynamically stable above 1150 °C. [205] At room temperature, the solubility limit is low and $Ca_xMn_{1-x}S$ (with x around 0.5) is unstable. This instability can explain the changes from heating as the decomposition of $Ca_{1-x}Mn_xS$ to CaS and MnS. However, if ball-milling made a solid-solution-type $Ca_xMn_{1-x}S$ with a full continuous range of chemically allowed x ($0 \leq x \leq 1$), then this phase should not co-exist with CaS or MnS as they should merge together with a single set of rock salt XRD peaks. However, distinct peaks for CaS and $Ca_xMn_{1-x}S$ were seen in the as-ground sample, indicating two phases with discontinuous composition ranges. For 300 °C sample, even three distinct composition ranges were seen. It is also hard to believe the mechanochemical process from ball milling can produce $Ca_xMn_{1-x}S$ ($x \sim 0.33$), which requires > 1000 °C to be thermodynamically stable. Chemically it makes more sense that ball-milling made a new material that is stoichiometrically precise instead of a solid solution. The same explanations on temperature behaviors apply where this new material was not high-temperature stable and dissociated into CaS and MnS when heated. However, these arguments require the new phase to have an ordered structure that is related to rock salt, which was intriguing. Both scenarios (a solid solution and a new order phase) are plausible and further studies were required to settle the debate.

Although no changes of crystalline phases were detected in the Sr–V–S system after ball milling (*i.e.* the sample consisted of SrS, V, and S), their reactions at higher temperature generated extra XRD peaks which were unable to be matched (Figure 8.3 and Figure 8.4). The unmatched peaks in the diffraction patterns were similar for the two stoichiometries tested: 2:1:4 and 1:4:7 Sr:V:S. After reactions at 300°C, XRD peaks from SrS and V still remained, but there appeared some additional peaks (Figure 8.3(b)). These peaks did not have high intensity with 300 °C reactions (Figure 8.3). Unmatched peaks were more significant with the reactions increased to 500 °C. With 2:1:4 Sr:V:S composition, the known phases in the XRD pattern were SrS, whereas with 1:4:7 Sr:V:S composition, the known phases were V_5S_8. However, there were additional peaks (Figure 8.3(c) and Figure 8.4(c)) that were similar for both compositions. We attribute these peaks to a new Sr-V-S phase. Ternary SrV_2S_5 has been suggested to exist with its diffraction pattern shown, [206] but no crystal structure of it was provided and its diffraction pattern does not fit that of our samples. With the temperature further increased to 700 °C, nothing drastically happened based on XRD but there were slight changes to the peaks of the unknown (Figure 8.3(d) and Figure 8.4(d)). Therefore, the structure of this new phase might have slight variations

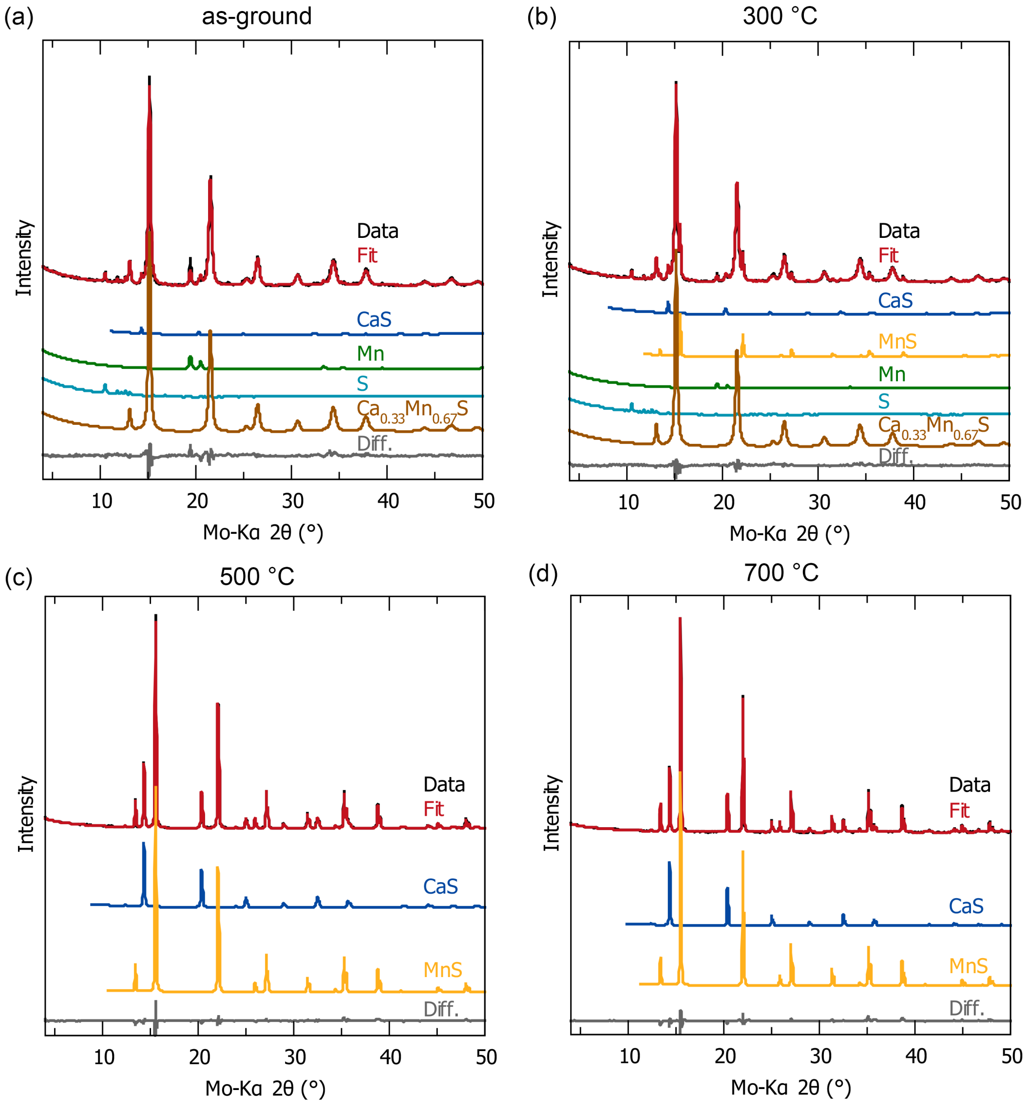

Figure 8.2: XRD patterns with Rietveld refinement for the (a) ball-milled Ca, Mn, and S (1:2:4), and their reaction products with (b) 300 °C, (c) 500 °C, and (d) 700 °C reactions.

with temperature.

Another new phase was discovered in the Sr–Cr–S system (1:4:7 Sr:Cr:S) when the reaction temperature was 700 °C (Figure 8.5). No significant phase changes happened with ball milling and 300 °C heat treatment (Figure 8.5(a,b)). At 500 °C, Cr was fully reacted with S to form $Cr_{0.67}S$, and at this stage the phases consisted of SrS and Cr_2S_3 (Figure 8.5(c)). SrS disappeared when the reaction temperature was increased to 700 °C. The overall diffraction peak intensities for the 700 °C sample were not high, but they were sufficient for phase matching. The only phase that can be matched was Cr_2S_3. Many additional Bragg peaks are present that we could not associate with known structures. Therefore, it was expected that a new phase was formed here, which was Sr-rich (Figure 8.5(d)).

Evidence for a new low-temperature phase was found in the Sr–Ni–S system (Figure 8.6). No phase change happened with ball milling for SrS, Ni, and S (1:1:2 Sr:Ni:S) (Figure 8.6(a)). The reaction at 300 °C removed Ni with the introduction of NiS. However, SrS and NiS could not account for all peaks (Figure 8.6(b)). Many strong peaks were seen, which we suspected were due to the presence of a new phase. When reacted at 500 °C, this new phase disappeared, and NiS underwent a phase transformation (Figure 8.6(c)). Little changes to the system happened when reaction temperature increased to 700 °C (Figure 8.6(d)). Therefore, it is suggested that this new phase is only potentially thermodynamically stable at low temperature (< 500 °C)

These new structures discovered with ball milling reagents were not the same as the phases predicted by DFT. The structures of these new phases need to be solved in the future.

8.4 Conclusions

We discovered the presence of at least 3 new sulfide materials while examining the phase stabilities of a series of ternary sulfides and selenides. These new materials were made by ball milling their reagents, and were not observed in the same reactions performed with

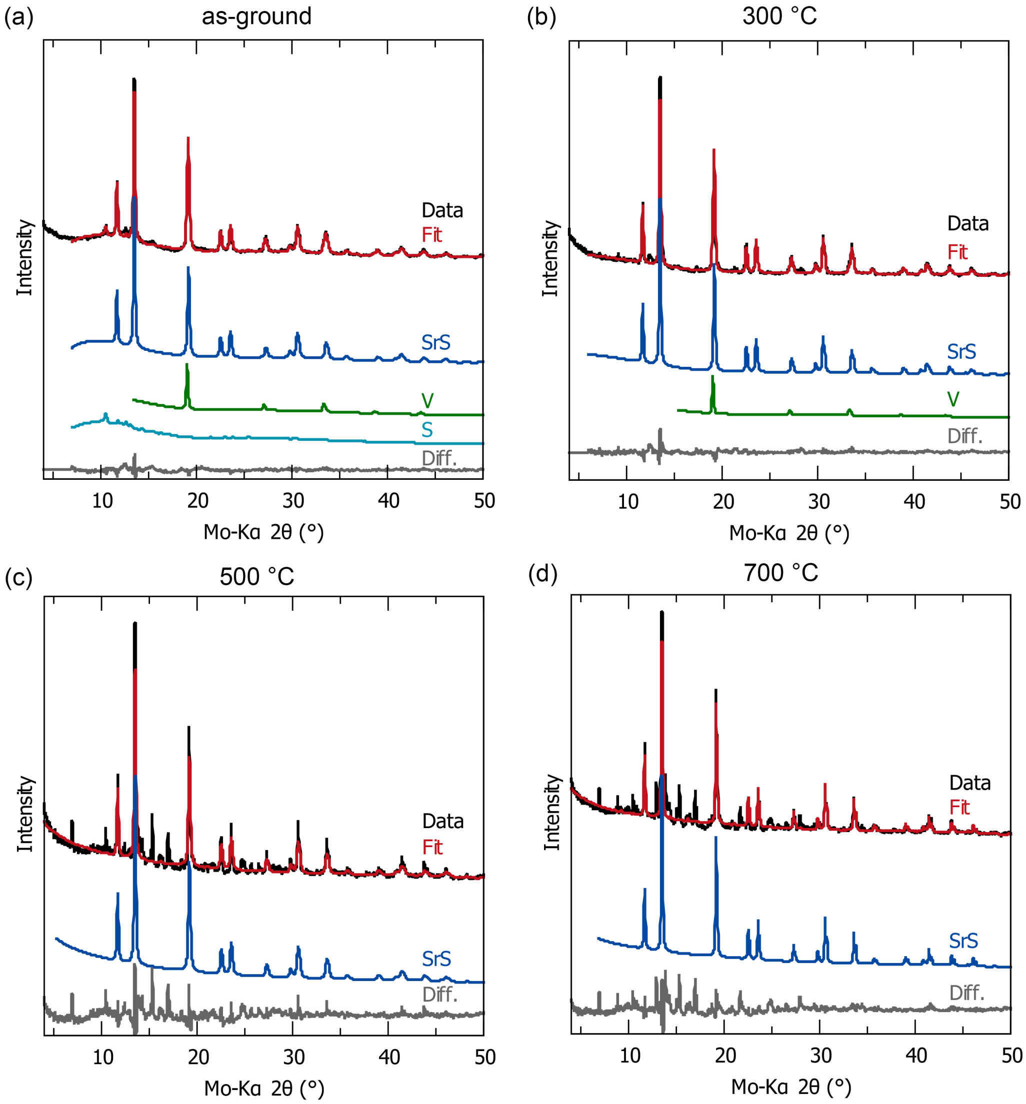

Figure 8.3: XRD patterns with Rietveld refinement for the (a) ball-milled SrS, V, and S (2:1:4 Sr:V:S), and their reaction products with (b) 300 °C, (c) 500 °C, and (d) 700 °C reactions.

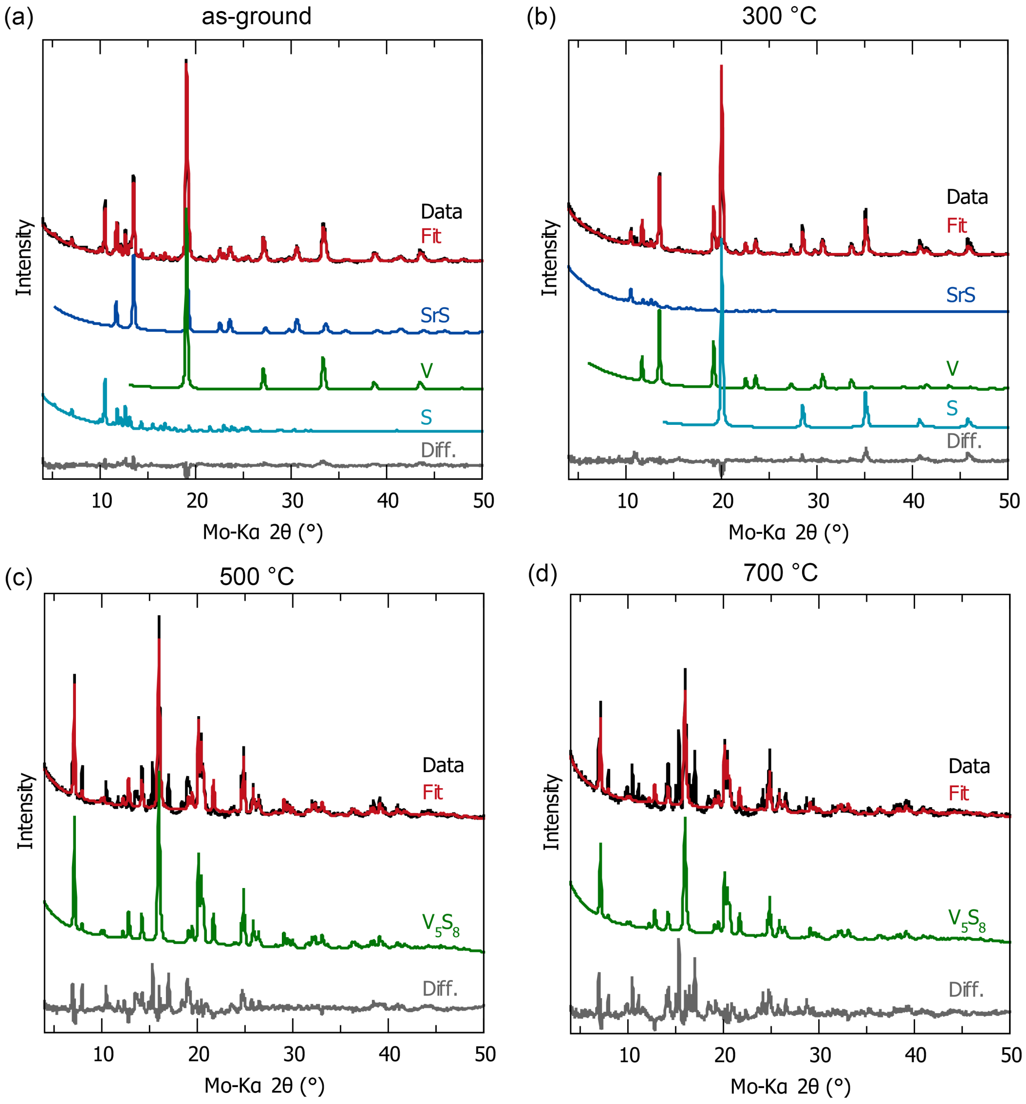

Figure 8.4: XRD patterns with Rietveld refinement for the (a) ball-milled SrS, V, and S (1:4:7 Sr:V:S), and their reaction products with (b) 300 °C, (c) 500 °C, and (d) 700 °C reactions.

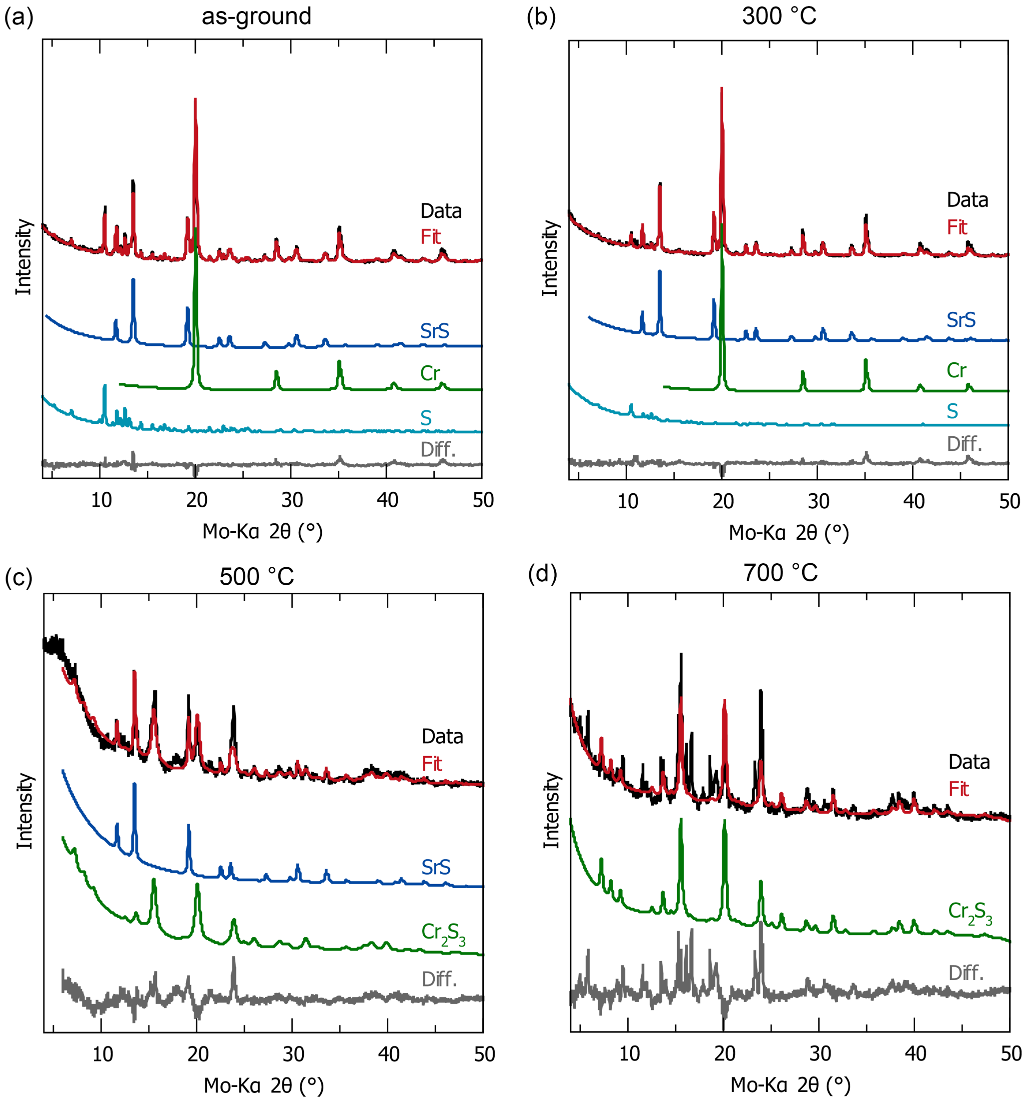

Figure 8.5: XRD patterns with Rietveld refinement for the (a) ball-milled SrS, Cr, and S (1:4:7 Sr:Cr:S), and their reaction products with (b) 300 °C, (c) 500 °C, and (d) 700 °C reactions.

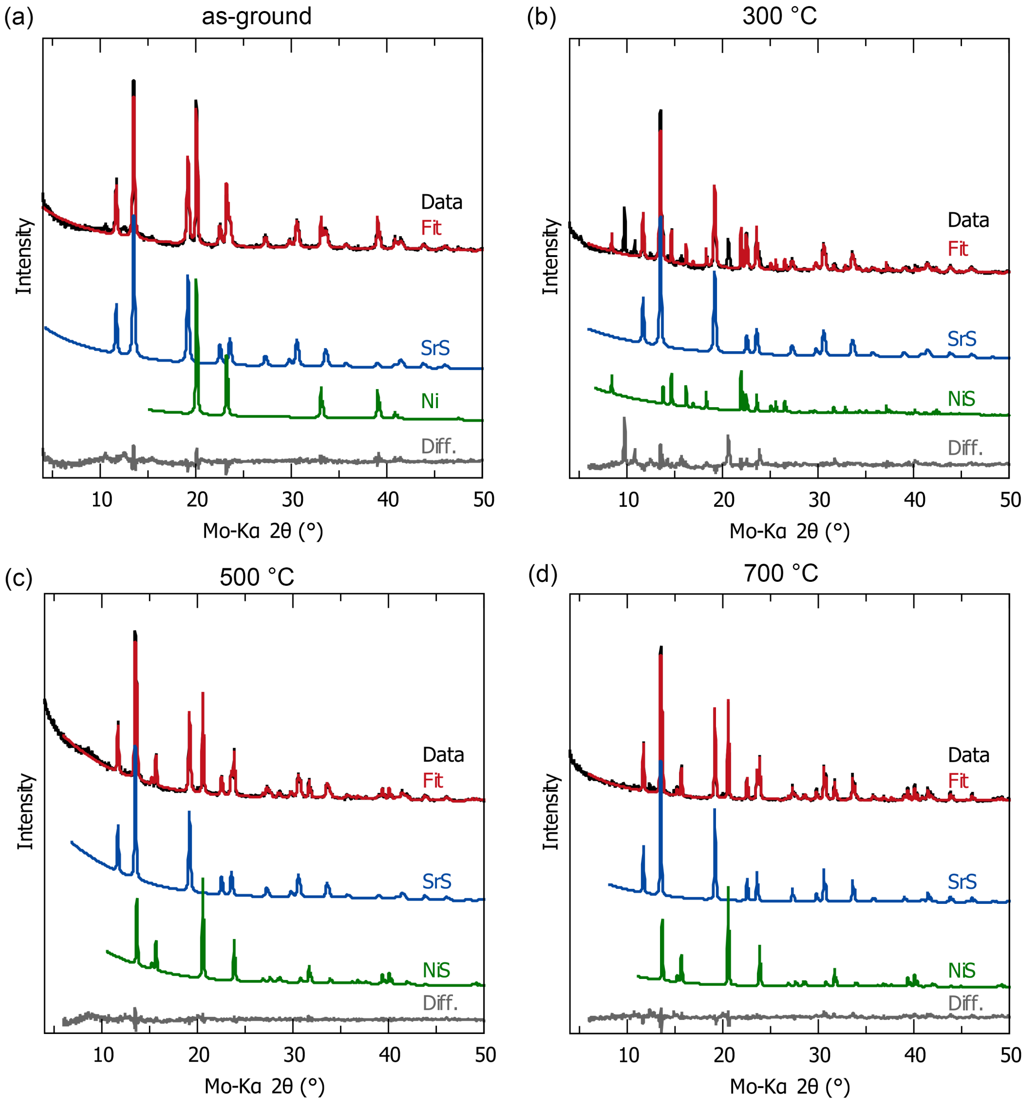

Figure 8.6: XRD patterns with Rietveld refinement for the (a) ball-milled SrS, Ni, and S (1:1:2 Sr:Ni:S), and their reaction products with (b) 300 °C, (c) 500 °C, and (d) 700 °C reactions.

reagents hand-ground using mortar and pestle. Although ball milling of the elements was found to be very effective in forming binary selenides (for the metals Sr, Pb, Bi, La, Cu), no strong evidence for the presence of unknown ternary selenides was seen. On the other hand, based on XRD, we discovered evidence for the presence of 4 unknown sulfides, all of them were strontium-based. A new possible Sr–V–S phase was identified to be present with 300 to 700 °C reaction temperature, although it might undergo slight structural changes with temperature. A high-temperature phase of Sr–Cr–S was discovered that formed at 700 °C and is assumed to be Sr-rich in composition. A new low-temperature and a new high-temperature phase of Sr–Ni–S were identified. A low-temperature Sr–Ni–S phase formed at 300 °C but was no longer stable at 500 °C. We also saw behaviors in the Ca–Mn–S system that could not be fully explained yet. While the X-ray patterns might be fit by the solid solution $Ca_xMn_{1-x}S$, they do not comply with known thermodynamic phase diagrams. The possibility of having a new ordered Ca–Mn–S phase could not be ruled out. To summarize, using ball milling or similar comminution techniques to reduce the kinetic barriers to inorganic materials formation can be extremely effective in the search for new materials using solid state reactions.

CHAPTER 9

SUMMARY AND FUTURE WORK

Time-resolved studies were used to understand the thermodynamics and kinetics in two reaction types: solvothermal synthesis and solid state synthesis. It was shown that thermodynamic and kinetic information thus obtained can be used to understand the mechanisms of reactions. The knowledge allowed us to improve synthesis designs and discover new inorganic materials.

Ex situ studies were performed on the solvothermal formation of Cu_4O_3 by quenching the reactions, which allowed the construction of kinetic maps and the proposal of reaction mechanisms. *In situ* examination using EDXRD gave further support for these mechanisms. Solvothermal chemistries were tested by substituting DMF in the solvent with other reagents, which allowed us to discover four new Cu-containing crystalline phases. One of them had its crystal structure solved and was found to possess a unique stereochemistry.

In situ lab XRD was used to reveal the factors relevant to the solid state formation of Fe_2SiS_4. Inspired by the effective factors that expedited Fe_2SiS_4 formation, investigations of new inorganic materials were carried out in various ternary sulfide and selenide systems. BaS_3 was used as a reactive flux to discover flux-assisted crystallization of Ba–Fe–S compounds. Both lab and synchrotron *in situ* XRD revealed the formation of unknown phases crystallized from the flux. Ball milling was performed on the reagents used in solid state synthesis, which formed products that were different from that made using hand mortar-and-pestle grinding in some systems. The existence of three new materials was suggested in systems of Sr–V–S, Sr–Cr–S, and Sr–Ni–S.

We have discovered many new materials based on the observation of unmatched diffraction patterns: 4 Cu-containing inorganic materials with organic groups, 5 flux-grown Ba–Fe–S crystals, and 3 other ternary sulfides containing Sr, and a possible ordered Ca–Mn–S structure. Except for one copper-tris(ethylenediamine) compound, the crystal structures of the other newly discovered phases are not solved yet. With the present information available, structure solutions are challenging. The best way to carry out structure solution is to prepare these samples as single crystals, which requires optimization of the synthesis and crystal growth. For the Cu-containing powders developed by solvothermal synthesis, neutron diffraction in conjugation with X-ray diffraction will be needed so that C, H, N, and O can have more contributions to diffraction. Elemental analysis and thermal analysis also aid determination of phase compositions. For the ternary sulfides, elemental analysis on a small volume-scale (*e.g.* energy-dispersive X-ray spectroscopy with transmission electron microscopy) would help to suggest approximate compositions of the new materials. If phase pure samples can be made by adjustment of precursor stoichiometries, structure solution will be made more straightforward with the help of high-resolution synchrotron diffraction at 11-BM-B in APS.

Several of our *in situ* environments for synchrotron diffraction had unforeseen shortcomings that can be improved upon. Better *in situ* monitoring of solvothermal reactions with EDXRD can be realized with the following: a larger gauge volume (∼2mm in each direction), higher X-ray energies, a smaller scattering angle, and a specially-designed sample holder to fix the sample position. The use of *in situ* diffraction in 17-BM-B for high-temperature solid state reactions in capillaries can also be improved upon by having a shorter capillary length (or longer heating coil lengths) and a smaller sampling length. An automated tool of computer-aided analysis of cluster diffraction patterns can also be used to detect and group similar patterns. The Bruker PolySNAP 3 suite is a potential candidate for this purpose. This may improve the efficiency of working with the giant number of patterns involved in *in situ* studies.

REFERENCES

[1] Nicola Spaldin, “Fundamental materials research and the course of human civilization”, *VSH-Bulletin* **2**, pp. 11–15 (2017).

[2] Michael A. Gevelber and George Stephanopoulos, “Dynamics and control of the czochralski process: I. modelling and dynamic characterization”, *J. Cryst. Growth* **84**(4), pp. 647 – 668 (1987).

[3] Xiaofang Lai, Hui Zhang, Yingqi Wang, Xin Wang, Xian Zhang, Jianhua Lin, and Fuqiang Huang, “Observation of Superconductivity in Tetragonal FeS”, *J. Am. Chem. Soc.* **137**(32), pp. 10148–10151 (2015).

[4] Hiroki Takahashi, Akira Sugimoto, Yusuke Nambu, Touru Yamauchi, Yasuyuki Hirata, Takateru Kawakami, Maxim Avdeev, Kazuyuki Matsubayashi, Fei Du, Chizuru Kawashima, Hideto Soeda, Satoshi Nakano, Yoshiya Uwatoko, Yutaka Ueda, Taku J. Sato, and Kenya Ohgushi, “Pressure-induced superconductivity in the iron-based ladder material $BaFe_2S_3$”, *Nat. Mater.* **14**(10), pp. 1008–1012 (2015).

[5] C.-Y. Kuo, Z. Hu, J. C. Yang, S.-C. Liao, Y. L. Huang, R. K. Vasudevan, M. B. Okatan, S. Jesse, S. V. Kalinin, L. Li, H. J. Liu, C.-H. Lai, T. W. Pi, S. Agrestini, K. Chen, P. Ohresser, A. Tanaka, L. H. Tjeng, and Y. H. Chu, “Single-domain multiferroic $BiFeO_3$ films”, *Nat. Commun.* **7**, pp. 12712 (2016).

[6] Man-Rong Li, Peter W. Stephens, Maria Retuerto, Tapati Sarkar, Christoph P. Grams, Joachim Hemberger, Mark C. Croft, David Walker, and Martha Greenblatt, “Designing Polar and Magnetic Oxides: Zn2fetao6 - in Search of Multiferroics”, *J. Am. Chem. Soc.* **136**(24), pp. 8508–8511 (2014).

[7] Martin A. Green, Anita Ho-Baillie, and Henry J. Snaith, “The emergence of perovskite solar cells”, *Nat. Photonics* **8**(7), pp. 506–514 (2014).

[8] Juan J. de Pablo, Barbara Jones, Cora Lind Kovacs, Vidvuds Ozolins, and Arthur P. Ramirez, “The Materials Genome Initiative, the interplay of experiment, theory and computation”, *Curr. Opin. Solid State Mat. Sci.* **18**(2), pp. 99–117 (2014).

[9] Geoffroy Hautier, Anna Miglio, Gerbrand Ceder, Gian-Marco Rignanese, and Xavier Gonze, “Identification and design principles of low hole effective mass p-type transparent conducting oxides”, *Nat. Commun.* **4** (2013).

[10] Stefano Curtarolo, Gus L. W. Hart, Marco Buongiorno Nardelli, Natalio Mingo, Stefano Sanvito, and Ohad Levy, "The high-throughput highway to computational materials design", *Nat. Mater.* **12**(3), pp. 191–201 (2013).

[11] Martin Jansen, "Conceptual Inorganic Materials Discovery A Road Map", *Adv. Mater.* **27**(21), pp. 3229–3242 (2015).

[12] Chiara Panosetti, Konstantin Krautgasser, Dennis Palagin, Karsten Reuter, and Reinhard J. Maurer, "Global Materials Structure Search with Chemically Motivated Coordinates", *Nano Lett.* **15**(12), pp. 8044–8048 (2015).

[13] Hideomi Koinuma and Ichiro Takeuchi, "Combinatorial solid-state chemistry of inorganic materials", *Nat. Mater.* **3**(7), pp. 429–438 (2004).

[14] Yan Wang, William Davidson Richards, Shyue Ping Ong, Lincoln J. Miara, Jae Chul Kim, Yifei Mo, and Gerbrand Ceder, "Design principles for solid-state lithium superionic conductors", *Nat. Mater.* **14**(10), pp. 1026–1031 (2015).

[15] Yun Liu and Jeffrey C. Grossman, "Accelerating the Design of Solar Thermal Fuel Materials through High Throughput Simulations", *Nano Lett.* **14**(12), pp. 7046–7050 (2014).

[16] "Asm alloy phase diagram database", https://matdata.asminternational.org/apd/, Accessed July 6, 2019.

[17] "Springermaterials – properties of materials", https://materials.springer.com/, Accessed July 6, 2019.

[18] "Fact – facility for the analysis of chemical thermodynamics", http://www.crct.polymtl.ca/fact/, Accessed July 6, 2019.

[19] P Norby and J. C Hanson, "Hydrothermal synthesis of the microporous aluminophosphate CoAPO-5; in situ time-resolved synchrotron X-ray powder diffraction studies", *Catal. Today* **39**(4), pp. 301–309 (1998).

[20] Kasper T. Møller, Bjarne R. S. Hansen, Ann-Christin Dippel, Jens-Erik Jørgensen, and Torben R. Jensen, "Characterization of Gas-Solid Reactions using In Situ Powder X-ray Diffraction", *Z. Anorg. Allg. Chem.* **640**(15), pp. 3029–3043 (2014).

[21] Helena Van Swygenhoven and Steven Van Petegem, "In-situ mechanical testing during X-ray diffraction", *Mater. Charact.* **78**, pp. 47–59 (2013).

[22] Thomas W. Cornelius and Olivier Thomas, "Progress of in situ synchrotron X-ray diffraction studies on the mechanical behavior of materials at small scales", *Prog. Mater. Sci.* **94**, pp. 384–434 (2018).

[23] Giovanni Esteves, Chris M. Fancher, and Jacob L. Jones, "In situ characterization of polycrystalline ferroelectrics using x-ray and neutron diffraction", *J. Mater. Res.* **30**(3), pp. 340–356 (2015).

[24] Johanna Nelson, Sumohan Misra, Yuan Yang, Ariel Jackson, Yijin Liu, Hailiang Wang, Hongjie Dai, Joy C. Andrews, Yi Cui, and Michael F. Toney, "In Operando X-ray Diffraction and Transmission X-ray Microscopy of Lithium Sulfur Batteries", *J. Am. Chem. Soc.* **134**(14), pp. 6337–6343 (2012).

[25] Ashkan Salamat, Rebecca A. Fischer, Richard Briggs, Malcolm I. McMahon, and Sylvain Petitgirard, "In situ synchrotron X-ray diffraction in the laser-heated diamond anvil cell: Melting phenomena and synthesis of new materials", *Coord. Chem. Rev.* **277-278**, pp. 15–30 (2014).

[26] Gérard Demazeau, "Solvothermal processes: a route to the stabilization of new materials", *J. Mater. Chem.* **9**(1), pp. 15–18 (1999).

[27] Jing Li, Zhen Chen, Ru-Ji Wang, and Davide M. Proserpio, "Low temperature route towards new materials: solvothermal synthesis of metal chalcogenides in ethylenediamine", *Coord. Chem. Rev.* **190-192**, pp. 707–735 (1999).

[28] Devaraju Murukanahally Kempaiah and Honma Itaru, "Hydrothermal and Solvothermal Process Towards Development of LiMPO4 (M = Fe, Mn) Nanomaterials for LithiumIon Batteries", *Adv. Energy Mater.* **2**(3), pp. 284–297 (2012).

[29] Insung Han, Zhelong Jiang, Clarina dela Cruz, Hong Zhang, Huaping Sheng, Ankita Bhutani, Dean J. Miller, and Daniel P. Shoemaker, "Accessing magnetic chalcogenides with solvothermal synthesis: KFeS2 and KFe2s3", *J. Solid State Chem.* **260**, pp. 1–6 (2018).

[30] Xiao-Ming Chen and Ming-Liang Tong, "Solvothermal in Situ Metal/Ligand Reactions: A New Bridge between Coordination Chemistry and Organic Synthetic Chemistry", *Acc. Chem. Res.* **40**(2), pp. 162–170 (2007).

[31] Athena S. Sefat, "Bulk synthesis of iron-based superconductors", *Curr. Opin. Solid State Mat. Sci.* **17**(2), pp. 59–64 (2013).

[32] Daniel P. Shoemaker, Efrain E. Rodriguez, Ram Seshadri, Ivana Sabaj Abumohor, and Thomas Proffen, "Intrinsic exchange bias in $\mathrm{Zn}_x\mathrm{Mn}_{3-x}\mathrm{O}_4$ ($x\leq1$) solid solutions", *Phys. Rev. B* **80**(14), pp. 144422 (2009).

[33] Rachmat Adhi Wibowo, Woon Hwa Jung, and Kyoo Ho Kim, "Synthesis of $Cu_2ZnSnSe_4$ compound powders by solid state reaction using elemental powders", *J. Phys. Chem. Solids* **71**(12), pp. 1702–1706 (2010).

[34] Steven N. Girard, Jiaqing He, Xiaoyuan Zhou, Daniel Shoemaker, Christopher M. Jaworski, Ctirad Uher, Vinayak P. Dravid, Joseph P. Heremans, and Mercouri G. Kanatzidis, "High Performance Na-doped PbTe–PbS Thermoelectric Materials: Electronic Density of States Modification and Shape-Controlled Nanostructures", *J. Am. Chem. Soc.* **133**(41), pp. 16588–16597 (2011).

[35] Kuo-Wei Yeh, Tzu-Wen Huang, Yi-lin Huang, Ta-Kun Chen, Fong-Chi Hsu, Phillip M. Wu, Yong-Chi Lee, Yan-Yi Chu, Chi-Lian Chen, Jiu-Yong Luo, Der-Chung Yan, and Maw-Kuen Wu, "Tellurium substitution effect on superconductivity of the α-phase iron selenide", *Europhys. Lett.* **84**(3), pp. 37002 (2008).

[36] Mara Valeria Blanco, Katja Kohopää, Irina Snigireva, and Federico Cova, "Low temperature solid state synthesis of Li5feo4 and CO2 capture mechanism via real time in situ synchrotron X-ray diffraction", *Chem. Eng. J.* **354**, pp. 370–377 (2018).

[37] Zhelong Jiang, Arun Ramanathan, and Daniel P. Shoemaker, "In situ identification of kinetic factors that expedite inorganic crystal formation and discovery", *J. Mater. Chem. C* **5**(23), pp. 5709–5717 (2017).

[38] Richard I.Walton, "Subcritical solvothermal synthesis of condensed inorganic materials", *Chem. Soc. Rev.* **31**(4), pp. 230–238 (2002).

[39] Shengjie Xu, Dian Li, and Peiyi Wu, "One-Pot, Facile, and Versatile Synthesis of Monolayer MoS2/WS2 Quantum Dots as Bioimaging Probes and Efficient Electrocatalysts for Hydrogen Evolution Reaction", *Adv. Funct. Mater.* **25**(7), pp. 1127–1136 (2015).

[40] Walter H. Brattain, "The Copper Oxide Rectifier", *Rev. Mod. Phys.* **23**(3), pp. 203–212 (1951).

[41] B. P. Rai, "Cu_2O solar cells: A review", *Sol. Cells* **25**(3), pp. 265–272 (1988).

[42] Ki Hyun Yoon, Woo Jin Choi, and Dong Heon Kang, "Photoelectrochemical properties of copper oxide thin films coated on an n-Si substrate", *Thin Solid Films* **372**(12), pp. 250–256 (2000).

[43] K. Akimoto, S. Ishizuka, M. Yanagita, Y. Nawa, Goutam K. Paul, and T. Sakurai, "Thin film deposition of Cu_2O and application for solar cells", *Sol. Energy* **80**(6), pp. 715–722 (2006).

[44] Yingchi Liu, Hubert K. Turley, John R. Tumbleston, Edward T. Samulski, and Rene Lopez, "Minority carrier transport length of electrodeposited Cu_2O in ZnO/Cu_2O heterojunction solar cells", *Appl. Phys. Lett.* **98**(16), pp. 162105 (2011).

[45] Mingdong Wang, Fangyan Xie, Weiguang Xie, Shizhao Zheng, Ning Ke, Jian Chen, Ni Zhao, and J. B. Xu, "Device lifetime improvement of polymer-based bulk heterojunction solar cells by incorporating copper oxide layer at Al cathode", *Appl. Phys. Lett.* **98**(18), pp. 183304 (2011).

[46] B. K. Meyer, A. Polity, D. Reppin, M. Becker, P. Hering, P. J. Klar, Th. Sander, C. Reindl, J. Benz, M. Eickhoff, C. Heiliger, M. Heinemann, J. Bläsing, A. Krost, S. Shokovets, C. MüFller, and C. Ronning, "Binary copper oxide semiconductors: From materials towards devices", *Phys. Status Solidi B* **249**(8), pp. 1487–1509 (2012).

[47] David Snoke, "Spontaneous Bose Coherence of Excitons and Polaritons", *Science* **298**(5597), pp. 1368–1372 (2002).

[48] Jia Ling Lin and J. P. Wolfe, "Bose-Einstein condensation of paraexcitons in stressed Cu_2O", *Phys. Rev. Lett.* **71**(8), pp. 1222–1225 (1993).

[49] M. Y. Shen, T. Yokouchi, S. Koyama, and T. Goto, "Dynamics associated with Bose-Einstein statistics of orthoexcitons generated by resonant excitations in cuprous oxide", *Phys. Rev. B* **56**(20), pp. 13066–13072 (1997).

[50] X. K. Chen, J. C. Irwin, and J. P. Franck, "Evidence for a strong spin-phonon interaction in cupric oxide", *Phys. Rev. B* **52**(18), pp. R13130–R13133 (1995).

[51] A. B. Kuz'menko, D. van der Marel, P. J. M. van Bentum, E. A. Tishchenko, C. Presura, and A. A. Bush, "Infrared spectroscopic study of CuO: Signatures of strong spin-phonon interaction and structural distortion", *Phys. Rev. B* **63**(9), pp. 094303 (2001).

[52] Haiming Fan, Bingsuo Zou, Yulong Liu, and Sishen Xie, "Size effect on the electron-phonon coupling in CuO nanocrystals", *Nanotechnology* **17**(4), pp. 1099 (2006).

[53] Jorge Ramírez-Ortiz, Tetsuya Ogura, Jorge Medina-Valtierra, Sofa E Acosta-Ortiz, Pedro Bosch, J Antonio de los Reyes, and Victor H Lara, "A catalytic application of Cu_2O and CuO films deposited over fiberglass", *Appl. Surf. Sci.* **174**(34), pp. 177–184 (2001).

[54] Eli A. Goldstein and Reginald E. Mitchell, "Chemical kinetics of copper oxide reduction with carbon monoxide", *Proc. Combus. Inst.* **33**(2), pp. 2803–2810 (2011).

[55] Marie Claire Marion, Edouard Garbowski, and Michel Primet, "Catalytic properties of copper oxide supported on zinc aluminate in methane combustion", *J. Chem. Soc., Faraday Trans.* **87**(11), pp. 1795–1800 (1991).

[56] Tatsumi Ishihara, Masakazu Higuchi, Toshiaki Takagi, Masami Ito, Hiroyasu Nishiguchi, and Yusaku Takita, "Preparation of CuO thin films on porous $BaTiO_3$ by self-assembled multibilayer film formation and application as a CO_2 sensor", *J. Mater. Chem.* **8**(9), pp. 2037–2042 (1998).

[57] T. J. Richardson, J. L. Slack, and M. D. Rubin, "Electrochromism in copper oxide thin films", *Electrochim. Acta* **46**(1314), pp. 2281–2284 (2001).

[58] M. Wei, N. Braddon, D. Zhi, P. A. Midgley, S. K. Chen, M. G. Blamire, and J. L. MacManus-Driscoll, "Room temperature ferromagnetism in bulk Mn-Doped Cu_2O", *Appl. Phys. Lett.* **86**(7), pp. 072514 (2005).

[59] S. G. Yang, T. Li, B. X. Gu, Y. W. Du, H. Y. Sung, S. T. Hung, C. Y. Wong, and A. B. Pakhomov, "Ferromagnetism in Mn-doped CuO", *Appl. Phys. Lett.* **83**(18), pp. 3746–3748 (2003).

[60] X. P. Gao, J. L. Bao, G. L. Pan, H. Y. Zhu, P. X. Huang, F. Wu, and D. Y. Song, "Preparation and Electrochemical Performance of Polycrystalline and Single Crystalline CuO Nanorods as Anode Materials for Li Ion Battery", *J. Phys. Chem. B* **108**(18), pp. 5547–5551 (2004).

[61] Ji Chan Park, Jeonghan Kim, Hyuksang Kwon, and Hyunjoon Song, "Gram-Scale Synthesis of Cu_2O Nanocubes and Subsequent Oxidation to CuO Hollow Nanostructures for Lithium-Ion Battery Anode Materials", *Adv. Mater.* **21**(7), pp. 803–807 (2009).

[62] Lin Hu, Yimin Huang, Fapei Zhang, and Qianwang Chen, "CuO/Cu_2O composite hollow polyhedrons fabricated from metalorganic framework templates for lithium-ion battery anodes with a long cycling life", *Nanoscale* **5**(10), pp. 4186–4190 (2013).

[63] George A. Koenig, "On paramelaconite, and the associated minerals", *Proc. Nat. Acad. Sci. Phila.* **43**, pp. 284–291 (1892).

[64] Clifford Frondel, "Paramelaconite: A Tetragonal Oxide of Copper", *Am. Mineral.* **26**, pp. 657 (1941).

[65] M. O'Keeffe and J. O. Bovin, "The crystal structure of paramelaconite, Cu_4O_3", *Am. Miner.* **63**(1-2), pp. 180–185 (1978).

[66] Jason S. Gardner, Michel J. P. Gingras, and John E. Greedan, "Magnetic pyrochlore oxides", *Rev. Mod. Phys.* **82**(1), pp. 53–107 (2010).

[67] J. D. M. Champion, M. J. Harris, P. C. W. Holdsworth, A. S. Wills, G. Balakrishnan, S. T. Bramwell, E. Čižmár, T. Fennell, J. S. Gardner, J. Lago, D. F. McMorrow, M. Orendáč, A. Orendáčová, D. McK. Paul, R. I. Smith, M. T. F. Telling, and A. Wildes, "$Er_2Ti_2O_7$: Evidence of quantum order by disorder in a frustrated antiferromagnet", *Phys. Rev. B* **68**(2), pp. 020401 (2003).

[68] M. J. P. Gingras, C. V. Stager, N. P. Raju, B. D. Gaulin, and J. E. Greedan, "Static Critical Behavior of the Spin-Freezing Transition in the Geometrically Frustrated Pyrochlore Antiferromagnet $Y_2Mo_2O_7$", *Phys. Rev. Lett.* **78**(5), pp. 947–950 (1997).

[69] Steven T. Bramwell and Michel J. P. Gingras, "Spin Ice State in Frustrated Magnetic Pyrochlore Materials", *Science* **294**(5546), pp. 1495–1501 (2001).

[70] J. S. Gardner, G. Ehlers, N. Rosov, R. W. Erwin, and C. Petrovic, "Spin-spin correlations in $Yb_2Ti_2O_7$: A polarized neutron scattering study", *Phys. Rev. B* **70**(18), pp. 180404 (2004).

[71] L. Pinsard-Gaudart, J. Rodríguez-Carvajal, A. Gukasov, and P. Monod, "Magnetic properties of paramelaconite (Cu4o3): A pyrochlore lattice with S=1/2", *Phys. Rev. B* **69**(10), pp. 104408 (2004).

[72] M. A. de Vries, J. R. Stewart, P. P. Deen, J. O. Piatek, G. J. Nilsen, H. M. Rønnow, and A. Harrison, "Scale-Free Antiferromagnetic Fluctuations in the S=1/2 Kagome Antiferromagnet Herbertsmithite", *Phys. Rev. Lett.* **103**(23), pp. 237201 (2009).

[73] M.-H. Whangbo and H.-J. Koo, "Spin Dimer Analysis of the Spin Exchange Interactions in Paramelaconite Cu_4O_3 and Its Analogue $Ag_2Cu_2O_3$ and the Spin Ordering of the Cu_2O_3 Spin Lattice Leading to Their Magnetic Phase Transitions", *Inorg. Chem.* **41**(13), pp. 3570–3577 (2002).

[74] K. J. Blobaum, D. Van Heerden, A. J. Wagner, D. H. Fairbrother, and T. P. Weihs, "Sputter-deposition and characterization of paramelaconite", *J. Mater. Res.* **18**(07), pp. 1535–1542 (2003).

[75] Markus Heinemann, Bianca Eifert, and Christian Heiliger, "Band structure and phase stability of the copper oxides Cu_2O, CuO, and Cu_4O_3", *Phys. Rev. B* **87**(11), pp. 115111 (2013).

[76] P. E. D. Morgan, D. E. Partin, B. L. Chamberland, and M. O'Keeffe, "Synthesis of Paramelaconite: Cu4o3", *J. Solid State Chem.* **121**(1), pp. 33–37 (1996).

[77] R. Vijaya Kumar, Y. Mastai, and A. Gedanken, "Sonochemical Synthesis and Characterization of Nanocrystalline Paramelaconite in Polyaniline Matrix", *Chem. Mater.* **12**(12), pp. 3892–3895 (2000).

[78] Jorge Medina-Valtierra, Claudio Frausto-Reyes, Gabriela Camarillo-Martínez, and Jorge A. Ramírez-Ortiz, "Complete oxidation of isopropanol over Cu_4O_3 (paramelaconite) coating deposited on fiberglass by CVD", *Appl. Catal. A* **356**(1), pp. 36–42 (2009).

[79] Neil J. Long and Amanda K. Petford-Long, "In-situ electron-beam-induced reduction of CuO: A study of phase transformations in cupric oxide", *Ultramicroscopy* **20**(1), pp. 151–159 (1986).

[80] Kazuyuki Amikura, Takeshi Kimura, Mika Hamada, Noriko Yokoyama, Jun Miyazaki, and Yasuhiro Yamada, "Copper oxide particles produced by laser ablation in water", *Appl. Surf. Sci.* **254**(21), pp. 6976–6982 (2008).

[81] Wenhao Chen, Hong Zhang, Zhiyuan Ma, Bao Yang, and Zhicheng Li, "High electrochemical performance and lithiationdelithiation phase evolution in CuO thin films for Li-ion storage", *J. Mater. Chem. A* **3**(27), pp. 14202–14209 (2015).

[82] J. F. Pierson, A. Thobor-Keck, and A. Billard, "Cuprite, paramelaconite and tenorite films deposited by reactive magnetron sputtering", *Appl. Surf. Sci.* **210**(34), pp. 359–367 (2003).

[83] Lirun Zhao, Han Chen, Yingli Wang, Hongwei Che, Poernomo Gunawan, Ziyi Zhong, Hong Li, and Fabing Su, "Facile Solvothermal Synthesis of Phase-Pure Cu_4O_3 Microspheres and Their Lithium Storage Properties", *Chem. Mater.* **24**(6), pp. 1136–1142 (2012).

[84] Yuxin Tang, Yanyan Zhang, Jiyang Deng, Jiaqi Wei, Hong Le Tam, Bevita Kallupalathinkal Chandran, Zhili Dong, Zhong Chen, and Xiaodong Chen, "Mechanical

Force-Driven Growth of Elongated Bending TiO_2-based Nanotubular Materials for Ultrafast Rechargeable Lithium Ion Batteries", *Adv. Mater.* **26**(35), pp. 6111–6118 (2014).

[85] Zhelong Jiang, Yuxin Tang, Qiuling Tay, Yanyan Zhang, Oleksandr I. Malyi, Danping Wang, Jiyang Deng, Yuekun Lai, Huanfu Zhou, Xiaodong Chen, Zhili Dong, and Zhong Chen, "Understanding the Role of Nanostructures for Efficient Hydrogen Generation on Immobilized Photocatalysts", *Adv. Energy Mater.* **3**(10), pp. 1368–1380 (2013).

[86] Yuxin Tang, Zhelong Jiang, Qiuling Tay, Jiyang Deng, Yuekun Lai, Dangguo Gong, Zhili Dong, and Zhong Chen, "Visible-light plasmonic photocatalyst anchored on titanate nanotubes: A novel nanohybrid with synergistic effects of adsorption and degradation", *RSC Adv.* **2**(25), pp. 9406–9414 (2012).

[87] Mark J. Nilges, Karen Mattson, and R. Linn Belford, "SIMPOW6: A software package for the simulation of ESR powder-type spectra", In *ESR Spectroscopy in Membrane Biophysics, Biological Magnetic Resonance* volume 27 , pp. 261–281. Springer US (2007), "SIMPOW6: A software package for the simulation of ESR powder-type spectra" in ESR Spectroscopy in Membrane Biophysics, Biological Magnetic Resonance, Vol. 27, Hemminga, Marcus A., and Berliner, Lawrence Eds. Springer, New York.

[88] Koichi Momma and Fujio Izumi, "*VESTA*: A three-dimensional visualization system for electronic and structural analysis", *J. Appl. Crystallogr.* **41**(3), pp. 653–658 (2008).

[89] S. K. Hoffmann, J. Goslar, S. Lijewski, K. Tadyszak, A. Zalewska, A. Jankowska, P. Florczak, and S. Kowalak, "EPR and UV-Vis study on solutions of Cu(II) *dmit* complexes and the complexes entrapped in zeolite A and ZIF-$Cu(IM)_2$", *Microporous Mesoporous Mat.* **186**, pp. 57–64 (2014).

[90] Eugenio Garribba and Giovanni Micera, "The Determination of the Geometry of Cu(II) Complexes: An EPR Spectroscopy Experiment", *J. Chem. Educ.* **83**(8), pp. 1229 (2006).

[91] Yasuhiro Inada, Hiroo Hayashi, Ken-ichi Sugimoto, and Shigenobu Funahashi, "Solvation Structures of Manganese(II), Iron(II), Cobalt(II), Nickel(II), Copper(II), Zinc(II), and Gallium(III) Ions in Methanol, Ethanol, Dimethyl Sulfoxide, and Trimethyl Phosphate As Studied by EXAFS and Electronic Spectroscopies", *J. Phys. Chem. A* **103**(10), pp. 1401–1406 (1999).

[92] L. Debbichi, M. C. Marco de Lucas, J. F. Pierson, and P. Krüger, "Vibrational Properties of CuO and Cu_4O_3 from First-Principles Calculations, and Raman and Infrared Spectroscopy", *J. Phys. Chem. C* **116**(18), pp. 10232–10237 (2012).

[93] Yu Chang, Joong Jiat Teo, and Hua Chun Zeng, "Formation of Colloidal CuO Nanocrystallites and Their Spherical Aggregation and Reductive Transformation to Hollow Cu_2O Nanospheres", *Langmuir* **21**(3), pp. 1074–1079 (2005).

[94] Joong Jiat Teo, Yu Chang, and Hua Chun Zeng, “Fabrications of Hollow Nanocubes of Cu_2O and Cu via Reductive Self-Assembly of CuO Nanocrystals”, *Langmuir* **22**(17), pp. 7369–7377 (2006).

[95] Tim Ahnfeldt, Jens Moellmer, Vincent Guillerm, Reiner Staudt, Christian Serre, and Norbert Stock, “High-Throughput and Time-Resolved Energy-Dispersive X-Ray Diffraction (EDXRD) Study of the Formation of CAU-1-(OH)2: Microwave and Conventional Heating”, *Chem. Eur. J.* **17**(23), pp. 6462–6468 (2011).

[96] Alexej Michailovski, Jan-Dierk Grunwaldt, Alfons Baiker, Ragnar Kiebach, Wolfgang Bensch, and Greta R. Patzke, “Studying the Solvothermal Formation of MoO3 Fibers by Complementary In Situ EXAFS/EDXRD Techniques”, *Angew. Chem. Int. Edit.* **44**(35), pp. 5643–5647 (2005).

[97] Andrew M. Beale and Gopinathan Sankar, “In Situ Study of the Formation of Crystalline Bismuth Molybdate Materials under Hydrothermal Conditions”, *Chem. Mater.* **15**(1), pp. 146–153 (2003).

[98] “Plot85”, http://www.mpi.stonybrook.edu/NSLS/X17B2/Support/Plot85/plot85.htm, Accessed July 6, 2019.

[99] Wenwen Wang, Lianjie Zhu, Pengzhao Lv, Guokai Liu, Yanmiao Yu, and Jianfa Li, “Novel Candy-like Cu4o3 Microstructure: Facile Wet Chemical Synthesis, Formation Mechanism, and Good Long-Term Antibacterial Activities”, *ACS Appl. Mater. Interfaces* **10**(43), pp. 37287–37297 (2018).

[100] Axel Nørlund Christensen, Bente Lebech, Niels Hessel Andersen, and Jean-Claude Grivel, “The crystal structure of paramagnetic copper(II) oxalate (CuC2o4): formation and thermal decomposition of randomly stacked anisotropic nano-sized crystallites”, *Dalton Trans.* **43**(44), pp. 16754–16768 (2014).

[101] Geoffrey Wilkinson, Robert D Gillard, and Jon A McCleverty, *Comprehensive coordination chemistry: the synthesis, reactions, properties & applications of coordination compounds*, Oxford, England; New York: Pergamon Press 1st ed edition (1987), Includes bibliographies and indexes.

[102] W.A. Korfmacher, T.A. Getek, E.B. Hansen, and C.E. Cerniglia, “Direct analysis of microbial extracts containing metabolites of ethylenediamine-type antihistamines via high-performance liquid chromatography-thermospray mass spectrometry”, *Anal. Biochem.* **185**(1), pp. 136–142 (1990).

[103] Filippo Crea, AlfredoR. Galassi, Juan Carlos Kaski, Giuseppe Pupita, Hassan El Tamimi, GrahamJ. Davies, and Attilio Maseri, “Effect of theophylline on exercise-induced myocardial ischaemia”, *Lancet* **333**(8640), pp. 683–686 (1989), Originally published as Volume 1, Issue 8640.

[104] S.J. Hermansky, R.S.H. Yang, R.H. Garman, and H.W. Leung, “Chronic toxicity and carcinogenicity studies of ethylenediamine dihydrochloride by dietary incorporation in fischer 344 rats”, *Food Chem. Toxicol.* **37**(7), pp. 765–776 (1999).

[105] D. F. Clemens, B. M. Whitehurst, and G. B. Whitehurst, “Chelates in agriculture”, *Fertil. Res.* **25**(2), pp. 127–131 (1990).

[106] Marcia C. Delpech and Gisele S. Miranda, “Waterborne polyurethanes: influence of chain extender in ftir spectra profiles”, *Cent. Eur. J. Eng.* **2**(2), pp. 231–238 (2012).

[107] Jinhua Wang and Gita N. Ramaswamy, “One-step processing and bleaching of mechanically separated kenaf fibers: Effects on physical and chemical properties”, *Text. Res. J.* **73**(4), pp. 339–344 (2003).

[108] Gary R. Maxwell, *Ethylenediamine and Chelating Agents* , pp. 325–331, Springer US Boston, MA (2004).

[109] M. Nath, A. Choudhury, A. Kundu, and C.N.R. Rao, “Synthesis and characterization of magnetic iron sulfide nanowires”, *Adv. Mater.* **15**(24), pp. 2098–2101 (2003).

[110] Wenzhong Wang, Yan Geng, Ping Yan, Fuyu Liu, Yi Xie, and Yitai Qian, “A novel mild route to nanocrystalline selenides at room temperature”, *J. Am. Chem. Soc.* **121**(16), pp. 4062–4063 (1999).

[111] Martin Dale Alexander and Charles A. Spillert, “Monodentate ethylenediamine complex of cobalt(iii)”, *Inorg. Chem.* **9**(10), pp. 2344–2346 (1970).

[112] Ray F. Childers, K. G. Vander Zyl, Donald A. House, Robert Graham Hughes, and Clifford S. Garner, “Synthesis of a monodentate ethylenediamine complex of chromium(iii) and kinetics of hydrolysis of tetraaquoethylenediaminechromium(iii) cation and of pentaaquo(2-aminoethylammonium)chromium(iii) cation”, *Inorg. Chem.* **7**(4), pp. 749–754 (1968).

[113] Daryle H. Busch, K. Swaminathan, and Dean W. Cooke, “Stereochemistry and mechanism of the reactions of ethylenediamine with ethylenediaminetetraacetatocobaltate(iii) and propylenediaminetetraacetatocobaltate(iii)”, *Inorg. Chem.* **1**(2), pp. 260–267 (1962).

[114] D. F. Martin and M. L. Tobe, “Mechanism and steric course of octahedral aquation. part v. the isomerisation, racemisation, and water exchange of cis- and trans-aquoamminebis(ethylenediamine)cobalt(iii) salts”, *J. Chem. Soc.* , pp. 1388–1396 (1962).

[115] Stephen C. Pyke and R. G. Linck, “Rate of aquation of trans-difluorobis(ethylenediamine)chromium(iii) through an isolable monodentate ethylenediamine complex”, *Inorg. Chem.* **10**(11), pp. 2445–2449 (1971).

[116] Rachel L. Fanshawe, Akbar Mobinikhaledi, Charles R. Clark, and Allan G. Blackman, “Overcoming the chelate effect: hypodentate coordination of ethylenediamine, diethylenetriamine and tris(2-aminoethyl)amine in co(iii) complexes”, *Inorg. Chim. Acta* **307**(1), pp. 27–32 (2000).

[117] Okan Zafer Yeşilel, Halis Ölmez, and Cengiz Arici, "The first bis(orotato-n,o) cadmium complex with monodentate protonated ethylenediamine ligands: Synthesis, spectrothermal properties of a cadmium(ii)-orotato complex with ethylenediamine crystal structure of trans-[cd(hor)2(enh)2]2h2o and cis-[cd(h2o)2(phen)2](h2or)22h2o", *Polyhedron* **26**(14), pp. 3669–3674 (2007).

[118] Donald A. House and Peter J. Steel, "The first x-ray crystal structures of cobalt complexes containing monodentate and bridging ethylenediamine ligands", *Inorg. Chim. Acta* **288**(1), pp. 53–56 (1999).

[119] Philip O. Brown, Gary D. Enright, and John A. Ripmeester, "Nanocrystalline ag from supramolecular stabilization of metals in 4-tert-butylcalix[4]arene lattices", *Chem. Asian J.* **1**(4), pp. 529–535 (2006).

[120] Mary Duggan, Noel Ray, Brian Hathaway, Gustav Tomlinson, Paul Brint, and Kevin Pelin, "Crystal structure and electronic properties of ammine[tris(2-aminoethyl)amine]copper(II) diperchlorate and potassium penta-amminecopper(II) tris(hexafluorophosphate)", *J. Chem. Soc., Dalton Trans.* **0**(8), pp. 1342–1348 (1980).

[121] Oleg V. Dolomanov, Luc J. Bourhis, Richard J. Gildea, Judith A. K. Howard, and Horst Puschmann, "*OLEX2*: a complete structure solution, refinement and analysis program", *J. Appl. Crystallogr.* **42**(2), pp. 339–341 (2009).

[122] George M. Sheldrick, "*SHELXT* – Integrated space-group and crystal-structure determination", *Acta Crystallogr. A* **71**(1), pp. 3–8 (2015).

[123] George M. Sheldrick, "Crystal structure refinement with *SHELXL*", *Acta Crystallogr. C* **71**(1), pp. 3–8 (2015).

[124] Malcolm A. Halcrow, "Jahnteller distortions in transition metal compounds, and their importance in functional molecular and inorganic materials", *Chem. Soc. Rev.* **42**, pp. 1784–1795 (2013).

[125] B. J. Hathaway, "The evidence for "out-of-the-plane" bonding in axial complexes of the copper(ii) ion", In *Inorganic Chemistry* , pp. 49–67 Berlin, Heidelberg (1973). Springer Berlin Heidelberg.

[126] Anthony W. Addison, T. Nageswara Rao, Jan Reedijk, Jacobus van Rijn, and Gerrit C. Verschoor, "Synthesis, structure, and spectroscopic properties of copper(ii) compounds containing nitrogensulphur donor ligands; the crystal and molecular structure of aqua[1,7-bis(n-methylbenzimidazol-2-yl)-2,6-dithiaheptane]copper(ii) perchlorate", *J. Chem. Soc., Dalton Trans.* , pp. 1349–1356 (1984).

[127] S. F. Palopoli, S. J. Geib, A. L. Rheingold, and T. B. Brill, "Synthesis and modes of coordination of energetic nitramine ligands in copper(ii), nickel(ii), and palladium(ii) complexes", *Inorg. Chem.* **27**(17), pp. 2963–2971 (1988).

[128] Hiroshi Ogino and Junnosuke Fujita, "Cobalt(III) Complexes Containing Large Chelate Rings. I. Syntheses and Properties of Bis(ethylenediamine)-1,-diaminoalkanecobalt(III) Complexes", *Bull. Chem. Soc. Jpn.* **48**(6), pp. 1836–1841 (1975).

[129] M.Dale Alexander and Harold G. Kilcrease, "Binuclear chloropentaaminecobalt(iii) complexes", *J. Inorg. Nucl. Chem.* **35**(5), pp. 1583–1590 (1973).

[130] Y. Komiyama and E. C. Lingafelter, "The crystal structure of bisethylenediaminecopper(II) nitrate", *Acta Crystallogr.* **17**(9), pp. 1145–1148 (1964).

[131] K. R. Maxcy and M. M. Turnbull, "A redetermination of bis(ethylenediamine-*N*,*N'*)bis(perchlorato-*O*)copper(II)", *Acta Crystallogr. C* **55**(12), pp. 1986–1988 (1999).

[132] B. W. Brown and E. C. Lingafelter, "The crystal structure of bis(ethylenediamine)copper(II) thiocyanate", *Acta Crystallogr.* **17**(3), pp. 254–259 (1964).

[133] D. S. Brown, J. D. Lee, and B. G. A. Melsom, "The crystal structure of bis(ethylenediamine)copper(II) fluoroborate", *Acta Crystallogr. B* **24**(5), pp. 730–734 (1968).

[134] Tony D. Keene, Michael B. Hursthouse, and Daniel J. Price, "Recurrent h-bond graph motifs between metal tris-ethylenediamine cations and uncoordinated oxalate anions: Fitting a three pin plug into a two pin socket", *CrystEngComm* **14**, pp. 116–123 (2012).

[135] Duyen N. K. Pham, Mrittika Roy, James A. Golen, and David R. Manke, "The first-row transition-metal series of tris(ethylenediamine) diacetate complexes $[M(\mathrm{en})_3](\mathrm{OAc})_2$ (M is Mn, Fe, Co, Ni, Cu, and Zn)", *Acta Crystallogr. C* **73**(6), pp. 442–446 (2017).

[136] Safaa-Eldin H. Etaiw, Safaa N. Abdou, and Ahmed S. Badr El-din, "Structure and spectral characterization of coordination polymers constructed by cucn and aliphatic diamines", *J. Inorg. Organomet. Polym. Mater.* **25**(6), pp. 1394–1406 (2015).

[137] Ming-Tian Li, Cheng-Gang Wang, Yu Wu, and Xu-Cheng Fu, "Diaquabis(ethylenediamine-$\kappa^2 N,N'$)copper(II) bis(4-aminonaphthalene-1-sulfonate) dihydrate", *Acta Crystallogr. E* **61**(8), pp. m1660–m1661 (2005).

[138] Takashiro Akitsu and Yasuaki Einaga, "Thermal and Photo-Responsibility of Axial Semi-Coordination Bonds in a Copper(II) Complex", *Bull. Chem. Soc. Jpn.* **77**(4), pp. 763–764 (2004).

[139] Jannik Bjerrum, C. J. Ballhausen, Chr. Klixbüll Jørgensen, and Nils Andreas Sörensen, "Studies on Absorption Spectra. I. Results of Calculations on the Spectra and Configuration of Copper(II) Ions.", *Acta Chem. Scand.* **8**, pp. 1275–1289 (1954).

[140] Stef Smeets, Pascal Parois, Hans-Beat Bürgi, and Martin Lutz, "Temperature-dependent analysis of thermal motion, disorder and structures of tris(ethylenediamine)zinc(II) sulfate and tris(ethylenediamine)copper(II) sulfate", *Acta Crystallogr. B* **67**(1), pp. 53–62 (2011).

[141] K. Krishnan and Robert A. Plane, “Raman and infrared spectra of complexes of ethylenediamine with zinc(ii), cadmium(ii), and mercury(ii)”, *Inorg. Chem.* **5**(5), pp. 852–857 (1966).

[142] Xu Wang and Dong-Sheng Yang, “Spectroscopy and structures of copper complexes with ethylenediamine and methyl-substituted derivatives”, *J. Phys. Chem. A* **110**(24), pp. 7568–7576 (2006), PMID: 16774198.

[143] Paul M. Castro and Paul W. Jagodzinski, “Ftir and raman spectra and structure of cu(no3)+ in aqueous solution and acetone”, *Spectroc. Acta, Pt. A: Molec. Spectr.* **47**(12), pp. 1707–1720 (1991).

[144] José Pedro Donoso, Claudio J. Magon, José F. Lima, Otaciro R. Nascimento, Eglantina Benavente, Mabel Moreno, and Guillermo Gonzalez, “Electron paramagnetic resonance study of copperethylenediamine complex ion intercalated in bentonite”, *J. Phys. Chem. C* **117**(45), pp. 24042–24055 (2013).

[145] Firmin Velghe, Robert A. Schoonheydt, Jan B. Uytterhoeven, Paul Peigneur, and Jack H. Lunsford, “Spectroscopic characterization and thermal stability of copper(ii) ethylenediamine complexes on solid surfaces. 2. montmorillonite”, *J. Phys. Chem.* **81**(12), pp. 1187–1194 (1977).

[146] Angelo R. Rossi and Roald. Hoffmann, “Transition metal pentacoordination”, *Inorg. Chem.* **14**(2), pp. 365–374 (1975).

[147] A. A. G. Tomlinson and B. J. Hathaway, “The electronic properties and stereochemistry of the copper(ii) ion. part iii. some penta-ammine complexes”, *J. Chem. Soc. A* , pp. 1905–1909 (1968).

[148] I. M. Procter, B. J. Hathaway, and P. Nicholls, “The electronic properties and stereochemistry of the copper(ii) ion. part i. bis(ethylenediamine)copper(ii) complexes”, *J. Chem. Soc. A* , pp. 1678–1684 (1968).

[149] Daniel P. Shoemaker, Yung-Jin Hu, Duck Young Chung, Gregory J. Halder, Peter J. Chupas, L. Soderholm, J. F. Mitchell, and Mercouri G. Kanatzidis, “In situ studies of a platform for metastable inorganic crystal growth and materials discovery”, *PNAS* **111**(30), pp. 10922–10927 (2014).

[150] Daniel P. Shoemaker, Ram Seshadri, Andrew L. Hector, Anna Llobet, Thomas Proffen, and Craig J. Fennie, “Atomic displacements in the charge ice pyrochlore $Bi_2Ti_2O_6O$’ studied by neutron total scattering”, *Phys. Rev. B* **81**(14), pp. 144113 (2010).

[151] K. M. Kojima, R. Kadono, M. Miyazaki, M. Hiraishi, I. Yamauchi, A. Koda, Y. Tsuchiya, H. S. Suzuki, and H. Kitazawa, “Magnetic Frustration in Iridium Spinel Compound $CuIr_2S_4$”, *Phys. Rev. Lett.* **112**(8), pp. 087203 (2014).

[152] A. Biffin, R. D. Johnson, Sungkyun Choi, F. Freund, S. Manni, A. Bombardi, P. Manuel, P. Gegenwart, and R. Coldea, “Unconventional magnetic order on the

hyperhoneycomb Kitaev lattice in β-Li_2IrO_3: Full solution via magnetic resonant x-ray diffraction", *Phys. Rev. B* **90**(20), pp. 205116 (2014).

[153] Jeong-Wan Jo, Jaekyun Kim, Kyung-Tae Kim, Jin-Gu Kang, Myung-Gil Kim, Kwang-Ho Kim, Hyungduk Ko, Yong-Hoon Kim, and Sung Kyu Park, "Highly Stable and Imperceptible Electronics Utilizing Photoactivated Heterogeneous Sol-Gel Metal–Oxide Dielectrics and Semiconductors", *Adv. Mater.* **27**(7), pp. 1182–1188 (2015).

[154] Kannatassen Appavoo, Bin Wang, Nathaniel F. Brady, Minah Seo, Joyeeta Nag, Rohit P. Prasankumar, David J. Hilton, Sokrates T. Pantelides, and Richard F. Haglund, "Ultrafast Phase Transition via Catastrophic Phonon Collapse Driven by Plasmonic Hot-Electron Injection", *Nano Lett.* (2014).

[155] Jianping Lin, Xudong Li, Guanjun Qiao, Zhao Wang, Jesús Carrete, Yang Ren, Lingzhi Ma, Youjian Fei, Baifeng Yang, Lei Lei, and Ju Li, "Unexpected High-Temperature Stability of β-Zn_4Sb_3 Opens the Door to Enhanced Thermoelectric Performance", *J. Am. Chem. Soc.* **136**(4), pp. 1497–1504 (2013).

[156] Juliette Billaud, Raphaële J. Clément, A. Robert Armstrong, Jesús Canales-Vázquez, Patrick Rozier, Clare P. Grey, and Peter G. Bruce, "β-$NaMnO_2$: A High-Performance Cathode for Sodium-Ion Batteries", *J. Am. Chem. Soc.* **136**(49), pp. 17243–17248 (2014).

[157] Hai L. Feng, Masao Arai, Yoshitaka Matsushita, Yoshihiro Tsujimoto, Yanfeng Guo, Clastin I. Sathish, Xia Wang, Ya-Hua Yuan, Masahiko Tanaka, and Kazunari Yamaura, "High-Temperature Ferrimagnetism Driven by Lattice Distortion in Double Perovskite Ca_2FeOsO_6", *J. Am. Chem. Soc.* **136**(9), pp. 3326–3329 (2014).

[158] Shokouh S. Farvid, Tahereh Sabergharesou, Lisa N. Hutfluss, Manu Hegde, Eric Prouzet, and Pavle V. Radovanovic, "Evidence of Charge-Transfer Ferromagnetism in Transparent Diluted Magnetic Oxide Nanocrystals: Switching the Mechanism of Magnetic Interactions", *J. Am. Chem. Soc.* **136**(21), pp. 7669–7679 (2014).

[159] Haiyan Xia, Yunzhe Ye, Longgang Yan, Qingfang Liu, Jianbo Wang, and Desheng Xue, "Preparation and characterization of $Ba_2Co_2Fe_{12}O_{22}$ ferrite via glucose sol–gel method", *J. Sol-Gel Sci. Technol.* **61**(1), pp. 39–43 (2012).

[160] Wenping Geng, Yang Liu, Xiangjian Meng, Laurent Bellaiche, James F. Scott, Brahim Dkhil, and Anquan Jiang, "Giant Negative Electrocaloric Effect in Antiferroelectric La-Doped $Pb(ZrTi)O_3$ Thin Films Near Room Temperature", *Adv. Mater.* **27**(20), pp. 3165–3169 (2015).

[161] Zhelong Jiang, Shiliang Tian, Shuqi Lai, Rebecca D. McAuliffe, Steven P. Rogers, Moonsub Shim, and Daniel P. Shoemaker, "Capturing Phase Evolution during Solvothermal Synthesis of Metastable Cu_4O_3", *Chem. Mater.* **28**(9), pp. 3080–3089 (2016).

[162] Wonil Jung, Sujeong Lee, Dongwon Yoo, Sohee Jeong, Pere Miró, Agnieszka Kuc, Thomas Heine, and Jinwoo Cheon, "Colloidal Synthesis of Single-Layer MSe_2 (M = Mo, W) Nanosheets via Anisotropic Solution-Phase Growth Approach", *J. Am. Chem. Soc.* **137**(23), pp. 7266–7269 (2015).

[163] Shreyashi Ganguly, Nasrin Kazem, Danielle Carter, and Susan M. Kauzlarich, "Colloidal Synthesis of an Exotic Phase of Silicon: The BC8 Structure", *J. Am. Chem. Soc.* (2014).

[164] Daniel E. Bugaris and Hans-Conrad zurLoye, "Materials Discovery by Flux Crystal Growth: Quaternary and Higher Order Oxides", *Angew. Chem. Int. Ed.* **51**(16), pp. 3780–3811 (2012).

[165] Margret J. Geselbracht, Liam D. Noailles, Lien T. Ngo, Jessica H. Pikul, Richard I. Walton, E. Sarah Cowell, Franck Millange, and Dermot O'Hare, "Probing Molten Salt Flux Reactions Using Time-Resolved in Situ High-Temperature Powder X-ray Diffraction: A New Synthesis Route to the Mixed-Valence $NaTi_2O_4$", *Chem. Mater.* **16**(6), pp. 1153–1159 (2004).

[166] Martí Gich, Ignasi Fina, Alessio Morelli, Florencio Sánchez, Marin Alexe, Jaume Gázquez, Josep Fontcuberta, and Anna Roig, "Multiferroic Iron Oxide Thin Films at Room Temperature", *Adv. Mater.* **26**(27), pp. 4645–4652 (2014).

[167] Martin D. Burke and Stuart L. Schreiber, "A Planning Strategy for Diversity-Oriented Synthesis", *Angew. Chem. Int. Edit.* **43**(1), pp. 46–58 (2004).

[168] Miles Congreve, Stephen P. Andrews, Andrew S. Doré, Kaspar Hollenstein, Edward Hurrell, Christopher J. Langmead, Jonathan S. Mason, Irene W. Ng, Benjamin Tehan, Andrei Zhukov, Malcolm Weir, and Fiona H. Marshall, "Discovery of 1,2,4-Triazine Derivatives as Adenosine A_{2a} Antagonists using Structure Based Drug Design", *J. Med. Chem.* **55**(5), pp. 1898–1903 (2012).

[169] Matthew S. Baker and Scott T. Phillips, "A Two-Component Small Molecule System for Activity-Based Detection and Signal Amplification: Application to the Visual Detection of Threshold Levels of Pd(II)", *J. Am. Chem. Soc.* **133**(14), pp. 5170–5173 (2011).

[170] Sameh Helmy, Saemi Oh, Frank A. Leibfarth, Craig J. Hawker, and Javier Read de Alaniz, "Design and Synthesis of Donor–Acceptor Stenhouse Adducts: A Visible Light Photoswitch Derived from Furfural", *J. Org. Chem.* **79**(23), pp. 11316–11329 (2014).

[171] Andrew J. Martinolich and James R. Neilson, "Pyrite Formation via Kinetic Intermediates through Low-Temperature Solid-State Metathesis", *J. Am. Chem. Soc.* **136**(44), pp. 15654–15659 (2014).

[172] Andrew J. Martinolich, Joshua A. Kurzman, and James R. Neilson, "Polymorph Selectivity of Superconducting $CuSe_2$ Through Kinetic Control of Solid-State Metathesis", *J. Am. Chem. Soc.* **137**(11), pp. 3827–3833 (2015).

[173] Caroline Mellot-Draznieks, Stéphanie Girard, Gérard Férey, J. Christian Schön, Zeljko Cancarevic, and Martin Jansen, "Computational Design and Prediction of Interesting Not-Yet-Synthesized Structures of Inorganic Materials by Using Building Unit Concepts", *Chem. Eur. J.* **8**(18), pp. 4102–4113 (2002).

[174] Scott M. Woodley and Richard Catlow, "Crystal structure prediction from first principles", *Nat. Mater.* **7**(12), pp. 937–946 (2008).

[175] K. Büker, N. AlonsoVante, and H. Tributsch, "Photovoltaic output limitation of n-FeS_2 (pyrite) Schottky barriers: A temperature-dependent characterization", *J. Appl. Phys.* **72**(12), pp. 5721–5728 (1992).

[176] A. Ennaoui, S. Fiechter, Ch. Pettenkofer, N. Alonso-Vante, K. Büker, M. Bronold, Ch. Höpfner, and H. Tributsch, "Iron disulfide for solar energy conversion", *Sol. Energy Mater. Sol. Cells* **29**(4), pp. 289–370 (1993).

[177] Liping Yu, Stephan Lany, Robert Kykyneshi, Vorranutch Jieratum, Ram Ravichandran, Brian Pelatt, Emmeline Altschul, Heather A. S. Platt, John F. Wager, Douglas A. Keszler, and Alex Zunger, "Iron Chalcogenide Photovoltaic Absorbers", *Adv. Energy Mater.* **1**(5), pp. 748–753 (2011).

[178] H. Vincent, E. F. Bertaut, W. H. Baur, and R. D. Shannon, "Polyhedral Deformations in Olivine-Type Compounds and the Crystal Structure of Fe_2SiS_4 and Fe_2GeS_4", *Acta Cryst. B* **32**(6), pp. 1749–1755 (1976).

[179] V. Baron, Ö. Amcoff, and T. Ericsson, "Neutron powder diffraction study of the crystal and magnetic structures of Fe_2SiS_4", *J. Magn. Magn. Mater.* **195**(1), pp. 81–92 (1999).

[180] Tore Ericsson, Katalin Holényi, and Örjan Amcoff, "A Mössbauer study of Fe_2SiS_4, having the olivine structure: comparison with fayalite and related minerals", *J. Phys.: Condens. Matter* **9**(19), pp. 3943 (1997).

[181] P. Walder and A. D. Pelton, "Thermodynamic Modeling of the Fe-S System", *J. Phase Equilib. Diffus.* **26**(1), pp. 23–38 (2005).

[182] Jing-Feng Li, Fumiaki Sato, and Ryuzo Watanabe, "Synthesis of Ti_3SiC_2 polycrystals by hot-isostatic pressing of the elemental powders", *J. Mater. Sci. Lett.* **18**(19), pp. 1595–1597 (1999).

[183] Fumiaki Sato, Jing-Feng Li, and Ryuzo Watanabe, "Reaction Synthesis of Ti_3SiC_2 from Mixture of Elemental Powders", *Mater. Trans. JIM* **41**(5), pp. 605–608 (2000).

[184] Daniel P. Shoemaker, Duck Young Chung, J. F. Mitchell, Travis H. Bray, L. Soderholm, Peter J. Chupas, and Mercouri G. Kanatzidis, "Understanding Fluxes as Media for Directed Synthesis: *In Situ* Local Structure of Molten Potassium Polysulfides", *J. Am. Chem. Soc.* **134**(22), pp. 9456–9463 (2012).

[185] I. R. Fisher, M. C. Shapiro, and J. G. Analytis, "Principles of crystal growth of intermetallic and oxide compounds from molten solutions", *Philos. Mag.* **92**(19-21), pp. 2401–2435 (2012).

[186] Samuel J. Mugavero III, William R. Gemmill, Irina P. Roof, and Hans-Conrad zur Loye, "Materials discovery by crystal growth: Lanthanide metal containing oxides of the platinum group metals (Ru, Os, Ir, Rh, Pd, Pt) from molten alkali metal hydroxides", *J. Solid State Chem.* **182**(7), pp. 1950–1963 (2009).

[187] Stanisłw Mrowec, "On the defect structure and diffusion kinetics in transition metal sulphides and oxides", *React. Solids* **5**(4), pp. 241–268 (1988).

[188] Brian Gleeson, "Alloy Degradation Under Oxidizing-Sulfidizing Conditions at Elevated Temperatures", *Mater. Res.* **7**(1), pp. 61–69 (2004).

[189] D. J. Young and W. W. Smeltzer, "Sulfidation Kinetics of Iron and Ferritic Iron-Cobalt Alloys", *J. Electrochem. Soc.* **123**(2), pp. 229–234 (1976).

[190] M. Danielewski, S. Mrowec, and A. Stołosa, "Sulfidation of iron at high temperatures and diffusion kinetics in ferrous sulfide", *Oxid. Met.* **17**(1-2), pp. 77–97 (1982).

[191] S. Mrowec and M. Wedrychowska, "Kinetics and Mechanism of High-Temperature Sulfur Corrosion of Fe-Cr-Al Alloys", *Oxid. Met.* **13**(6), pp. 481–504 (1979).

[192] E. M. Fryt, W. W. Smeltzer, and J. S. Kirkaldy, "Chemical Diffusion and Point Defect Properties of Iron Sulfide ($Fe_{1-\delta}S$) at Temperatures 600°-1000°c", *J. Electrochem. Soc.* **126**(4), pp. 673–683 (1979).

[193] H. Mitsui, H. Habazaki, K. Hashimoto, and S. Mrowec, "The sulfidation and oxidation behavior of sputter-deposited amorphous Al-Nb-Si alloys at high temperatures", *Corrosion Sci.* **39**(1), pp. 9–26 (1997).

[194] J. Erlebacher, R. C. Newman, and K. Sieradzki, "Chapter 2:Fundamental Physics and Chemistry of Nanoporosity Evolution During Dealloying", In *Nanoporous Gold: From an Ancient Technology to a High-Tech Material* , pp. 11–29. (2012).

[195] J. Snyder, K. Livi, and J. Erlebacher, "Dealloying Silver/Gold Alloys in Neutral Silver Nitrate Solution: Porosity Evolution, Surface Composition, and Surface Oxides", *J. Electrochem. Soc.* **155**(8), pp. C464–C473 (2008).

[196] F. Kh. Urakaev and V. V. Boldyrev, "Mechanism and kinetics of mechanochemical processes in comminuting devices: 1. Theory", *Powder Technol.* **107**(1), pp. 93–107 (2000).

[197] P. C. Canfield and Z. Fisk, "Growth of single crystals from metallic fluxes", *Philos. Mag. B* **65**(6), pp. 1117–1123 (1992).

[198] H. Y. Hong and H. Steinfink, "The crystal chemistry of phases in the BaFeS and Se systems", *J. Solid State Chem.* **5**(1), pp. 93–104 (1972).

[199] J. S. Swinnea and H. Steinfink, "The crystal structure of -BaFe2s4: The first member in the infinitely adaptive series Bap(Fe2s4)q", *J. Solid State Chem.* **32**(3), pp. 329–334 (1980).

[200] S. Cohen, L. E. Rendon-Diazmiron, and H. Steinfink, "Phases in the Ba3fe1+xS5 series: The structure of -Ba9fe4s15 and its low-temperature polymorph", *J. Solid State Chem.* **25**(2), pp. 179–187 (1978).

[201] J. T. Hoggins and H. Steinfink, "Compounds in the infinitely adaptive series Bap(Fe2s4)q:Ba9(Fe2s4)8", *Acta Crystallogr. B* **33**(3), pp. 673–678 (1977).

[202] Okamoto H., "Ba-s (barium-sulfur)", In *Binary Alloy Phase Diagrams, Second Edition, Ed. T.B. Massalski, ASM International, Materials Park, Ohio* , pp. 610–611. (1990).

[203] S. Yamaoka, J. T. Lemley, J. M. Jenks, and H. Steinfink, "Structural chemistry of the polysulfides dibarium trisulfide and monobarium trisulfide", *Inorg. Chem.* **14**(1), pp. 129–131 (1975).

[204] Awadhesh Narayan, Ankita Bhutani, Samantha Rubeck, James N. Eckstein, Daniel P. Shoemaker, and Lucas K. Wagner, "Computational and experimental investigation for new transition metal selenides and sulfides: The importance of experimental verification for stability", *Phys. Rev. B* **94**(4), pp. 045105 (2016).

[205] Chi-Hung Leung and Lawrence H. Van Vlack, "Solubility Limits in Binary (Ca,Mn) Chalcogenides", *J. Am. Ceram. Soc.* **62**(11-12), pp. 613–616 (1979).

[206] Norihito Kijima, Shōzō Ikeda, Isao Shimono, Takehiko Matsumoto, Shigenori Tsuji, Ken-ichi Kumagai, and Shoichi Nagata, "A New Strontium Vanadium Sulfide, SrV2s5", *J. Solid State Chem.* **126**(2), pp. 189 – 194 (1996).